

EXTRACELLULAR VESICLES AS TARGETED VEHICLES FOR THERAPEUTIC  
DELIVERY

By

Victoria Avery Toomajian

A DISSERTATION

Submitted to  
Michigan State University  
in partial fulfillment of the requirements  
for the degree of

Biomedical Engineering – Doctor of Philosophy

2023

## ABSTRACT

Delivery tools such as viral vectors, lipids, liposomes, polymers, polymeric micelles, inorganic nanoparticles, and extracellular vesicles have been studied for targeted therapeutic delivery. A number of these have been approved by the Food and Drug Administration for treatment of disease and many are currently being investigated in clinical trials. Extracellular vesicles (EVs) are an emerging therapeutic delivery tool based on their ability to be naturally taken up by cells, low immunogenicity, and potential for inherent targeting ability. EVs are small membrane bound particles released by cells and are considered to be a naturally occurring method of cell-to-cell communication. The targeting ability of EVs has been demonstrated using tumor cell-derived EVs that show increased uptake in tumors and tumor cells. In addition, EVs from immune cells have been used to target areas of inflammation, and one potential benefit of using EVs is that tracking studies have shown that EVs cross tissue barriers *in vivo*.

EVs have been tracked by common imaging modalities, all of which rely on labeling the EV with a modality-specific tracer, such as inorganic nanoparticles, fluorescent dyes, bioluminescent or fluorescent proteins, or radioactive tags. One of the emerging imaging methods for tracking EVs *in vivo* is magnetic particle imaging (MPI), which uses superparamagnetic iron oxide nanoparticles (SPIOs) as the tracer. Once labeled with SPIOs, EVs can be tracked *in vivo* with MPI, which offers the significant advantages of being sensitive and directly quantitative. Development of EVs as a therapeutic delivery tool can be enhanced through imaging, and here I evaluate this for primary cancer and metastasis as well as cardiovascular disease.

I initially evaluated EV delivery to primary breast cancer in a mouse model because of disease prevalence and importance. Women in the United States have a 12.8% chance of developing breast cancer during their lifetime. This study labels breast cancer-derived EVs with

SPIOs (iron-labeled EVs referred to as FeEVs) to measure retention in primary breast cancer tumors with MPI. These FeEVs were retained for longer and in greater amounts compared to SPIOs *in vivo* when injected intratumorally. Further analysis of the tumors revealed that FeEVs were taken up by tumor cells and were found around tumor-associated macrophages (TAMs).

Breast cancer may metastasize to the brain which is often deadly, as it is very difficult to treat because of the blood brain barrier (BBB). Treatment options for brain metastasize include surgical resection, stereotactic radiosurgery, whole brain radiation therapy, and systemic chemo- or endocrine therapies, which are limited by the BBB. EVs have been shown to cross the BBB, offering the potential for use as a therapeutic delivery tool for metastatic tumors in the brain. For this reason, FeEVs from metastatic breast cancer cells with a predilection to going to the brain (brain-seeking) were injected into the left ventricle of the heart (intracardiac, i.c.) in mice with brain metastasis as well as healthy control mice. Unmodified SPIOs alone were also injected into mice with brain metastasis as a control to show EV targeting. Only mice with brain metastasis injected with FeEVs had detected iron signal in the head, indicating their possible use as a therapeutic delivery tool.

The third study involved EVs isolated from immune cells for targeting of myocardial infarction (MI). Human monocyte-like cells (THP-1) were transfected with firefly luciferase, and EVs from these cells were isolated and delivered to recipient cardiac organoids *in vitro*. Bioluminescence was detected in the recipient cells suggesting directed delivery. Assessing the difference in delivery to normal organoids and hypoxic organoids could be an indicator of effective targeting to diseased tissues. EVs isolated from specific donor cells demonstrated the ability to target damaged cardiac tissue.

Copyright by  
VICTORIA AVERY TOOMAJIAN  
2023

This thesis is dedicated to all the family and friends who have always asked about what I was working on, listened to me when I needed to think out loud, and understood when I needed to buckle down and work hard, or take a break. Your support is the reason I'm here.

## ACKNOWLEDGEMENTS

This dissertation is a labor of love. I have loved science from a young age, which was always encouraged by my parents. My earliest memories involve going to Women in Engineering and Women in Stem events and camps, or talking about the steps of problem solving over dinner. Being an engineer is about learning how to solve problems, and I was very blessed to have been encouraged to think of every issue as something to learn from and think about on my own.

I would first like to thank Dr. Christopher Contag, who has been an extremely helpful and supportive mentor, encouraging me to see the bright side of every failed experiment. The rest of the Contag group has been a huge support through this whole process, and I can't thank you all enough. I want to thank Dr. Ashley Makela, Evran Ural, and Dr. Emily Greeson for their help with gathering and analyzing all of the data. Thank you for being there and helping plan our eight "last experiments." Thank you to Dr. Cody Madsen and Dr. Chima Maduka for being supportive lab mates and friends, and always willing to listen, unless I had drank too much iced coffee immediately beforehand.

Thank you to my committee, Dr. Christopher Contag, Dr. Mark Worden, Dr. Aitor Aguirre, Dr. Masako Harada, and Dr. Masamitsu Kanada for all your wonderful insights and support. The mentorship each of you has offered me as been invaluable. Dr. Aguirre, thank you for letting me learn from your lab about stem cells and organoids. Dr. Kanada, thank you for teaching me about exosomes and reteaching me how to do lab work after a two year hiatus. Dr. Harada, thank you for your kind words and encouragement. Dr. Worden, thank you for an incredible class!

A big thank you to Dr. Emily Greeson again, for support, keeping snacks on hand for when my blood sugar got low, and remembering my allergies when I didn't. Thank you to Dr.

Kayla Connor-Halim and Evran Ural, for always knowing how to make me laugh, and giving me advice when I couldn't see a path forward. Thank you again to Dr. Ashley Makela for always being willing to answer my random texts about experiments or ideas and Dr. Cody Madsen for encouraging me to stick up for myself. Thank you to Erin, Justin, Lauren, Emily, Hunter, Jon, Kristin, Kylie, Adrianna, and Elyssa for all of the comradery and encouragement I've received. Science is a team effort, and even though we didn't do any experiments together, you're all a part of my team.

Thank you to Brenda Lippincott, Tiffany Owens, Saneeya Mir, and Heather Hazzard for your help and advice for navigating the degree process, as well as encouraging and supporting me. Tiffany and Saneeya, I still have the card you gave me at my comprehensive exam! It made me laugh when I couldn't be more stressed.

Thank you to all the mentors I've had in science over my life, officially and unofficially. Thank you to Dr. Christina Chan, who gave me my first opportunity to actually grow cells and learn how to study bioengineering. Thank you to Dr. Heather Powell for showing me how interesting biomaterials research could be, and for the jumpstart I got in learning about polymers for all my classes the next year. Thank you to all of my classmates in MSU's Materials Science and Engineering program, for all the late nights spent struggling over page long math problems and the comradery that occurs when your graduating class consists of less than 40 people. Thank to all of my professors in the program, especially Dr. Yue Qi, who always supported me and followed up with me even after I graduated and switched to biomedical engineering.

Funding for this dissertation came from the James and Kathleen Cornelius Endowment Fund, the MSU College of Engineering Dissertation Completion Fellowship, MetaVivor, and the John D. and Dortha Withrow Endowed Fellowship.

I want to thank everyone who played Fortnite, Minecraft, and Destiny 2 with me, every one of my TTRPG groups, and the cats of all my friends for all the emotional support. Thank you to Joe, Zak, Derek, Erin, Mel, Nicole, Des, and Nick for their support, and for providing laughs, fires, and great company. Thank you to Jake, Elissa, and Kylie for your long lasting friendships that survived living across the country in different time zones. We really all went through grad school and vet school together. Thank you to my second family, Riah, Robin, Edie, Erin, Scott, and Cam for growing with me. I have known you all for over half our lives at this point, and I'm so excited to see how we all continue to grow. Thanks to Michael Hood for hearing how stressed I was on discord and offering to proofread my first chapter for me! The notes you provided were invaluable.

Thank you to my family, and especially thanks to those of you that we lost on the journey to get here. Grandpa T, I'm always going to remember you asking me when I was going to build you a new heart. Grandpa S, I think of you every time I eat ice cream. Aunt Bridget, I wish we could talk about all the work I've done on breast cancer.

Thank you to all my aunts and uncles, for being almost second sets of parents and some of my favorite people to play games with. Thank you to my cousins, for being my second set of siblings, and some of my favorite people to gossip with and travel with. I'm very excited for our big cousins trip this year. Thank you to both my grandmas, for always being proud of me.

They aren't really words to describe how much my parents and my sisters have meant to me through this whole process. Thank you for being my cheerleaders. I know this took some time, but look! We made it! You are all my rock. Really, this is *our* thesis. I love you all more than I can possibly say without crying. I'm so proud of all of you, and I work hard to be someone that you are all proud of as well.

## TABLE OF CONTENTS

LIST OF ABBREVIATIONS.....	x
CHAPTER ONE: THERAPEUTIC DELIVERY TOOLS UNDER INVESTIGATION, EXTRACELLULAR VESICLES AS A TARGETED THERAPEUTIC DELIVERY TOOL, AND IMAGING TECHNIQUES OF EXTRACELLULAR VESICLES.....	1
REFERENCES.....	14
CHAPTER TWO: EXTRACELLULAR VESICLES FROM ISOLATED MAMMARY CARCINOMA CELLS ARE RETAINED FOR LONGER IN MAMMARY FAT PAD TUMORS COMPARED TO IRON ALONE.....	18
REFERENCES.....	39
CHAPTER THREE: EXTRACELLULAR VESICLES FROM BRAIN METASTASIS CELLS DERIVED FROM MAMMARY CARCINOMA CELLS TARGET METASTASES ACROSS THE BLOOD BRAIN BARRIER.....	41
REFERENCES.....	68
CHAPTER FOUR: EVS DERIVED FROM MACROPHAGES IN A SCAFFOLD CAN DELIVER REPORTER DNA TO INJURED CARDIAC CELLS .....	69
REFERENCES.....	93
CHAPTER FIVE: CONCLUSIONS AND FUTURE DIRECTIONS.....	95
REFERENCES.....	99

## LIST OF ABBREVIATIONS

AAV	Adeno-associated virus
FDA	Food and Drug Administration
PEG	Polythethylene glycol
MRI	Magnetic resonance imaging
siRNA	Small interfering ribonucleic acid
EV	Extracellular vesicle
BBB	Blood brain barrier
LPS	Lipopolysaccharide
GLuc	Gaussia luciferase
RLuc	Renilla luciferase
NanoLuc	Nano luciferase
NOTA	Bifunctional chelator 1,4,7-triazacyclononane-1,4,7-triacetic acid
ATP	Adenosine triphosphate
fLuc	Firefly luciferase
DNA	Deoxyribonucleic acid
SPECT	Single photon emission computed tomography
PET	Positron emission tomography
CT	Computed tomography
USPIO	Ultrasmall superparamagnetic iron oxide particles
TEM	Transmission electron microscopy
MSC	Mesenchymal stem cell
I.C.	Intracardiac

I.V.	Intravenous
I.N.	Intranasal
GNP	Gold nanoparticle
MPI	Magnetic particle imaging
PLGA	Poly(lactic-co-glycolic acid)
SPIO	Superparamagnetic iron oxide nanoparticle
PBS	Phosphate buffered saline
FeEV	Iron-labeled extracellular vesicle
mmEV	Macrophage/monocyte-derived extracellular vesicle
DiR	Lipophilic dye
DiD	Lipophilic dye

CHAPTER ONE:  
THERAPEUTIC DELIVERY TOOLS UNDER INVESTIGATION, EXTRACELLULAR  
VESICLES AS A TARGETED THERAPEUTIC DELIVERY TOOL, AND IMAGING  
TECHNIQUES OF EXTRACELLULAR VESICLES

## **INTRODUCTION**

### **Impact**

Therapeutic delivery strategies exist to improve the pharmacological properties of free drugs<sup>1</sup>, by enhancing the ability for a drug to go to its target site, as well as preventing it from accumulating in other areas where it may cause harm. All classes of nanotherapeutics, such as small molecules, proteins and peptides, antibodies, and nucleic acids, have challenges that can be mitigated using delivery technologies<sup>2</sup>.

### **Nanomedicine Delivery Strategies In Use and Under Development**

There are several viral and non-viral technologies in use for therapeutic nucleic acid or drug delivery. Viral options include viral vectors such as adeno associated viral vectors (AAV), retroviruses, adenoviruses, and herpes simplex viruses<sup>3</sup>. They often have a high transfection efficiency *in vitro*, but have failed in several clinical trials, which is speculated to be due to an immune response mounted in response, which is also a safety concern<sup>4,5</sup>. To avoid this, several non-viral approaches are used, though many of them may also produce an immune response. These include: lipids and liposomes, polymers and polymeric micelles, and inorganic nanoparticles. Several of these are actively used for drug delivery for cancer in patients, such as the popular Doxil, which is a liposome encapsulated doxorubicin, approved by the Food and Drug Administration (FDA) in 1995<sup>6</sup>. Several other liposome encapsulated drugs are approved for clinical use for treating cancer, including DepoCyt, Marqibo, and Onivyde<sup>7</sup>. Liposomes have been studied as a drug delivery system since the 1970's, and are small particles, typically 90-150 nm in diameter<sup>8</sup>. Therapeutics may either be stored in their empty cores or conjugated to their surface. They have been shown to increase blood circulation time, and passively

accumulate in tumors due to tumor vessel leakiness<sup>9</sup>. Liposomes can also be engineered for controlled release, and several more liposome-based therapies are currently in clinical trials.

Polymer nanoparticles include natural, synthetic, and pseudosynthetics, and can be 10 nm to 1  $\mu\text{m}$ <sup>7,10</sup>. They can also be entirely biodegradable, and release their contents over time.

Polymer nanoparticles are also currently in use for treating various diseases including hepatitis, multiple sclerosis, and hemophilia. This includes PEGylated small molecules and proteins such as interferons, which have increased circulation time and improved biocompatibility relative to free drug<sup>11</sup>. An example of this is PEGylated granulocyte colony stimulating factor (Neulasta®), approved by the FDA in 2002 for chemotherapy-induced neutropenia. As mentioned, polymer nanoparticles can enable controlled release of a therapeutic agent through slow-degradation, as seen in the case of Eligard®, which is a testosterone inhibiting drug packaged in a polylactide-co-glycolic acid (PLGA) nanoparticle approved by the FDA for symptoms of prostate cancer.

Polymer chains alone may also be used as a treatment for multiple sclerosis, as seen with glatiramer acetate, used as an immunomodulator to treat multiple sclerosis<sup>7,11</sup>. Another type of polymeric delivery platform are micelles, which are self-assembling polymeric amphiphiles<sup>7,11</sup>. These are used to carry hydrophobic drugs, allowing for slow and controlled release as the exterior surface dissolves in aqueous solutions while the internal core is hydrophobic. A micellar formulation of estradiol is approved by the FDA for treatment of menopause<sup>11</sup>.

Inorganic nanoparticles, including metals, metal oxides, silicas, and nanocrystals, are used for delivery and for their own therapeutic benefits. For examples, hydroxyapatite particles have been approved for FDA use from a few companies for use as a bone substitute.

Nanocrystals are made entirely out of a drug, to increase the surface area of the compound, which promotes quicker solubility. An example of this is Rapamune®, approved by the FDA in

2000, which increases the solubility of sirolimus, an immunosuppressant, by turning it into a nanocrystal. Iron nanoparticles, such as Feraheme®, Dexferrum®, and Venofer®, are all approved to treat iron deficiency<sup>7</sup>. Other metal and metal oxide reagents are used as both therapeutics and imaging agents. For example, iron nanoparticles can be used as contrast agents for magnetic resonance imaging (MRI). They can also be used for thermal ablation of tumors using magnetic hyperthermia<sup>12</sup>. Gold nanoparticles have also been used as a drug delivery vector to cancer, and gold can be used as a contrast agent for several different types of *in vivo* deep tissue imaging, including multi-photon imaging, optical coherence tomography, and photoacoustic imaging<sup>13</sup>. Gold is non-toxic and inert, and can be surface functionalized for targeting and retention<sup>14</sup>. CYT-6091, a gold nanoparticle bound to tumor necrosis factor alpha for cancer treatment, completed a phase I clinical trial, and is set to begin phase 2 as of 2020<sup>15</sup>. Silicon nanoparticles typically incorporate pores, which allows for greater drug encapsulation. These nanoparticles also have high stability, and may promote an immune response for immunotherapy<sup>14</sup>. Carbon nanotubes have been used as a delivery vehicle for drugs such as doxorubicin and small interfering ribonucleic acid (siRNA) for various types of cancer, and on their own can be used for thermal ablation as exposure to radiation allows them to produce heat<sup>12,13,16</sup>.

Extracellular vesicles, or EVs, are small membrane bound vesicles naturally released from cells as a method of cell-to-cell communication<sup>17</sup>. They are typically considered to fall into three major categories, defined by their method of biogenesis, size and molecular markers. Apoptotic bodies are released by dead and dying cells, and are the largest in size, up to 5  $\mu\text{m}$  in diameter<sup>17</sup>. Microvesicles are released from an outward budding of the cell membrane, and are considered to be 100-1,000 nm in diameter<sup>17</sup>. Exosomes are formed by an internal budding of a

multivesicular body inside a cell, which are then released into the extracellular space when the multivesicular body merges with the cell membrane, and are typically 30-150 nm in diameter<sup>17</sup>. The microvesicle and exosome populations are very difficult to separate from each other, due to the overlap in size. Many EV isolation methods, including the most common method of ultracentrifugation, concentrate vesicles based on size. For this reason, and a lack of consensus for specific markers of each EV subtype, ISEV 2018 standards suggest that vesicles be referred to as EVs, instead of using the terms “exosome” or “microvesicle”, which we will follow for this work<sup>18</sup>.

EVs are an emerging therapeutic delivery tool, due to the fact that they are naturally taken up by cells, have potential for an inherent targeting ability, and have low immunogenicity<sup>19</sup>. Drugs or other therapeutics are typically loaded directly (loading the EVs themselves) or indirectly (loading the parent cell, which produces EVs loaded with the same therapeutic)<sup>19</sup>, however loading is typically limited. There are several EV-related clinical trials undergoing development currently, with a few focused on using EVs as a delivery tool<sup>20</sup>. Two of these studies use EVs derived from human cells, with one using mesenchymal stromal cell-derived EVs to deliver siRNA to metastatic pancreatic cancer<sup>21</sup> (NCT03608631) and another using dendritic cell-derived EVs to deliver a tumor antigen to patients with small lung cancers<sup>22</sup> (NCT01159288). The first of these trials is currently in the recruitment stage, while the second has completed Phase I and is currently recruiting for Phase II. A third clinical trial is using plant-derived EVs to deliver curcumin to colon tumors, as curcumin has limited bioavailability on its own<sup>23</sup> (NCT01294072). This study is currently in recruitment for Phase I.

## Potential EV Targeting

EVs from tumor cells have been shown to be selectively taken up by tumors *in vivo* and *in vitro* in various types of cancer. For colorectal cancer, EVs from murine colorectal cancer cell (CT26), loaded with doxorubicin, targeted CT26 3D tumor spheroids *in vitro* and colorectal tumors formed from CT26 cells in mice<sup>24</sup>. Another example of this like-to-like tumor targeting was also seen in fibrosarcoma, where fibrosarcoma HT1080 EVs loaded with Doxil were preferentially retained in tumors formed from HT1080 in mice, and displayed tumor targeting<sup>25</sup>. Interestingly, tumor cell EVs could also target metastasis formed from the same tumor cells. This was shown in two different studies. One used breast cancer MDA-MB-231 cells to form tumors in mice, and found that treatment with EVs from MDA-MB-231 cells loaded with doxorubicin interfered with the formation of lung metastases<sup>26</sup>. More interestingly, a post-surgical treatment model of lung metastasis treatment was used to show that excised tumor cells EVs can target lung metastasis<sup>27</sup>. Breast cancer tumors and a resulting lung metastasis were established in mice. The breast cancer tumors were excised, and EVs were collected from these cells and loaded with cationic bovine serum albumin conjugated to siS100A4. These EVs had better anti-metastatic activity compared to liposomes containing CBSA-si100A4, supporting the better suitability of EVs as a therapeutic delivery tool compared to a synthetic, commonly used tool<sup>27</sup>. Tumor cells EVs can even target tumors made from other cells. EVs from hepatoma Bel7402 cells were loaded with porous silicon nanoparticles containing doxorubicin<sup>28</sup>. These EVs has enhanced uptake in cancer stem cell (H22) spheroids, as well as hepatocarcinoma tumors originating from H22 cells<sup>28</sup>.

EVs from immune cells can also target tumors and sites of metastases. EVs from macrophage cell line RAW264.7 or from primary bone-marrow derived macrophage cells

delivered paclitaxel to murine lung carcinoma cells (3LL-M27) *in vitro* and to mice with lung carcinomas derived from mCherry-3LL-M27 cells<sup>29</sup>. EVs from RAW264.7 loaded with doxorubicin or paclitaxel also inhibited growth of two different cancer models of triple negative breast cancer *in vivo*<sup>30</sup>. It is suggested that this is related to the fact that immune cells are recruited to tumors as part of the inflammatory immune response, and that components on the surface of the EVs, derived from the surface of the immune cells, allows them to be passively targeted to, and/or be retained in, areas of inflammation.

Immune cell EVs can also cross the blood brain barrier (BBB) and are being investigated for the treatment of neuroinflammatory diseases<sup>31-34</sup>. In an *in vivo* model of brain inflammation, EVs from mouse macrophage RAW264.7 cells were loaded with catalase and found to have greater therapeutic effects compared to catalase alone<sup>31</sup>. In a different *in vivo* model, RAW264.7 EVs accumulated in inflamed brains quicker and in greater amounts compared to the control<sup>32</sup>. It is important to note that EVs other than immune cell derived EVs can cross the BBB. In a study by Banks et al., EVs from several different types of non-cancerous cells, including mouse macrophages and fibroblasts as well as human T-cells and keratinocytes, were shown to cross the BBB when injected into the left jugular vein<sup>33</sup>. This was also done with human oral squamous cell-, melanoma cell-, breast cancer cell-, head and neck cancer cell-, and leukemia cell-derived EVs. Injecting lipopolysaccharide (LPS) to model neuroinflammation affected 7/10 of the exosome populations, with the human melanoma cell-, mouse macrophage cell-, and mouse fibroblast cell-derived EVs having no change in uptake, contrary to previous results with mouse macrophage-derived EVs<sup>33</sup>. It should be noted that this study used the J774A.1 cell line, not the RAW264.7 cell line that was used in the previous studies mentioned. Another study by Morad et al. studied the ability of human breast cancer-derived EVs to cross an intact BBB and

investigated the possible mechanism using an *in vitro* model<sup>34</sup>. It was found that these breast cancer-derived EVs crossed a model of human brain endothelial barriers on a transwell membrane in an active process that involved a clathrin-dependent endocytosis pathway as well as micropinocytosis<sup>34</sup>. Fluorescently labeled EVs derived from “brain-seeking” human breast cancer cells were taken up by astrocytes in healthy mice following retro-orbital injection as well.<sup>34</sup>

### **EV Tracking and Detection**

There are a few different ways to track EVs *in vivo* and *in vitro*. The first method is lipophilic fluorescence dyes, which specifically stain the lipid membrane of EVs. Commonly used dyes include DiR and DiD, both of which are also used for cellular imaging<sup>35</sup>. This method is typically used for *in vitro* studies, as fluorescence imaging suffers from signal loss based on depth *in vivo*. Additionally, dyes can actually outlast the EVs when the EVs degrade *in vivo*, due to their potential to have a long half-life. The lipid dyes can also form micelles that may interfere with analysis of EV distribution by producing a false signal. A way to avoid this is by using recombinant protein labeling. Fluorescent proteins are stably expressed in cells with tags that allow for them to be sorted to EVs, such as palmitoylation signals, which traffic to the inner membrane leaflet, or fusion with EV proteins, such as tetraspannin CD63, present in the cell-derived membrane of EVs and considered a standard EV marker<sup>35</sup>. This prevents the creation of false signals as the fluorescence is expressed by the producer cells and directed to the EVs, so micelles are not created. Fluorescence intensity is, in part, determined by the protein levels in EVs, and interestingly, expression of these fusion proteins by the producer cells may affect the cargo and uptake of EVs<sup>35</sup>.

Bioluminescence imaging can also be used to identify EVs, either directly or indirectly. For direct EV imaging, Gaussia luciferase (Gluc), Renilla luciferase (Rluc) or Nano luciferase (NanoLuc) have been used since the high energy substrates are sufficient for light production and co-factors such as ATP are not required. Use of the substrate as an energy source also means that these reporters can be used for extracellular imaging. Since these luciferases do not require ATP to produce light, makes them well-suited for many types of EV imaging experiments. The reporter genes can be expressed transiently or stably from EV producing cells by plasmid transfection or lentiviral transduction<sup>35</sup>. EVs can be indirectly imaged using firefly luciferase (fLuc), which requires ATP for light production, and as such can serve as a functional readout for EV-mediated delivery<sup>35</sup>. EVs can be used to delivery fLuc deoxyribonucleic acid (DNA), which the recipient cells then express, or alternatively the protein is delivered and the enzymatic activity used as a readout of delivery<sup>45</sup>. Since the signals come from the recipient cells and not the EVs themselves, this is considered indirect imaging. Luciferase requires a substrate in order to produce light and additionally while bioluminescence imaging is utilized for animal or cell studies, it is not used for clinical imaging.

Single photon emission computed tomography (SPECT) and positron emission tomography (PET) are widely used clinically to generate images from tracers labeled with different radioactive sources<sup>35</sup>. Several studies have also used these methods for EV imaging by labeling EVs with radioactive probes. One example of this is a study that labeled primary erythrocyte-derived EVs for *in vivo* SPECT imaging using <sup>99m</sup>Tc-tricarbonyl, which binds to several amino acids that can be found on the surface of EVs<sup>36</sup>. EVs were co-incubated with <sup>99m</sup>Tc-tricarbonyl complex solutions at room temperature for 30 minutes, before separating free <sup>99m</sup>Tc-tricarbonyl using a desalting compound. Combined SPECT/CT imaging of mice injected

with these radiolabeled EVs showed that the EV uptake was heavily concentrated in the liver<sup>36</sup>. A different study isolated EVs from 4T1 murine breast cancer cells before conjugating them with bifunctional chelator 1,4,7-triazacyclononane-1,4,7-triacetic acid (NOTA) and polyethylene glycol (PEG)<sup>37</sup>. The NOTA conjugation allowed for radiolabeling with  $^{64}\text{Cu}^{2+}$ , while the PEG conjugation was used for improving the *in vivo* properties. This radiolabeling allowed for both PEGylated and not PEGylated EVs to be traced in an *in vivo* 4T1 tumor model with PET scans over 24-h<sup>37</sup>. PEGylation did increase clearance time of the radiolabeled exosomes, as well as increased uptake in the tumor compared to the EVs that were not PEGylated<sup>37</sup>.

EVs can also be labeled with nanoparticles for different types of imaging including ultrasound, computed tomography (CT), and MRI<sup>35</sup>. Mesenchymal stem cells were labeled with ultrasmall superparamagnetic iron oxide particles (USPIO)<sup>38</sup>. EVs isolated from these labeled cells were believed to contain iron, based on transmission electron microscopy (TEM) imaging of the labeled cells showing USPIOs present in endocytic vesicles inside the cells. USPIOs appeared to be associated with the membranes of collected exosomes using TEM<sup>38</sup>. These USPIO-labeled EVs were injected intramuscular into the hind limbs of mice for *in vivo* MRI of the EVs, which were clearly detected in the muscle tissue. Injection of the same iron amount of plain USPIOs showed localized loss of signal compared to injection with the USPIO-labeled EVs<sup>38</sup>. A different study labeled mesenchymal stem cell (MSC)-derived EVs with glucose-coated gold nanoparticles for CT imaging of the brain<sup>39</sup>. MSC-derived EVs were co-incubated with the glucose-coated gold nanoparticles (GNP) for direct labeling instead of indirect labeling by labeling the EV-producing cells, confirmed by dark-field microscopy. GLUT-1 glucose transporter was found to be responsible for glucose-coated gold nanoparticle uptake into the EVs. These GNP-labeled EVs were injected intravenously (IV) or intranasally (IN) to determine

if the injection site had an impact on the biodistribution of the EVs, determined by CT imaging<sup>39</sup>. Injecting the GNP-labeled EVs IN resulted in significantly less accumulation in the liver and the EVs were retained in the brain for longer. The GNP-labeled EVs were then injected IN in an ischemic stroke mouse model, where *in vivo* CT scans showed accumulation of the labeled EVs in the stroke region<sup>39</sup>.

Magnetic particle imaging (MPI) is an imaging method that directly detects superparamagnetic iron oxide nanoparticles (SPIO) based on their magnetic properties<sup>40,41</sup>. Superparamagnetic nanoparticles switch their direction of magnetization in the direction of an applied magnetic field. Opposing magnetic fields are applied to the object being imaged, with a field free region, scanning over the area determined by the software. The particle is magnetized in the direction of the applied magnetic field, then relaxes in the field free region. It will then switch the direction of magnetization to the new applied magnetic field, generating signal. This signal is only generated when the flip in magnetization occurs, after the particle is exposed to the field free point. The imaging instrument knows where the field free point region is at all times, thus allowing the software to determine where the signal is and generate an image<sup>40</sup>. This type of imaging provides no anatomical information, so it typically needs to be paired with another imaging method such as CT<sup>40</sup>. There is no loss of signal based on depth enabling MPI to be quantitative. Cells and EVs can be labeled with these SPIOs to indirectly track them *in vivo*<sup>40-42</sup>. Human breast cancer cells MDA-MB-231 were labeled with SPIO nanoparticles, and SPIO-labeled EVs were isolated from those cells<sup>42</sup>. Association of SPIOs with the EVs was confirmed with TEM imaging. These SPIO-labeled EVs were further loaded with anti-cancer drug Olaparib and injected intratumor into mice bearing MDA-MB-231 xenografts. MPI of these mice confirmed that signal from the SPIOs was concentrated in the tumor<sup>42</sup>. Tumors injected every

two days with the EVs loaded with Olaparib had less tumor growth compared to tumors injected every two days with Olaparib or phosphate buffer saline (PBS) as controls<sup>42</sup>.

### **Summary and Dissertation Overview**

As described earlier, there are many therapeutic delivery strategies currently in use to improve the pharmacological properties of those therapeutics. These strategies include viral transfection tools such as AAV vectors, as well as non-viral solutions such as liposomes, polymers, and inorganic nanoparticles<sup>1,8,11</sup>. One emerging strategy is the use of EVs as a delivery tool, based on their natural ability to be taken up by cells as well as their potential for natural targeting. Some examples of the potential targeting were outlined, including cancer cell-derived EVs accumulating in tumor cells *in vitro* and tumors *in vivo*<sup>25,27,28,34</sup>, as well as immune-cell derived EVs accumulating in areas of inflammation. EVs from multiple sources were also shown to cross the BBB<sup>31,43</sup>. There are a few different modalities and strategies for imaging EVs. The first discussed is fluorescence-based imaging, utilizing lipid dyes or fluorescent proteins fused to tags associated with EVs<sup>35</sup>. The second is bioluminescent imaging, utilizing proteins such as GLuc and NanoLuc that produce light when a substrate is added. SPECT and PET imaging can also be used to image EVs, by adding a radioactive label to the EV membranes<sup>35</sup>. Labeling EVs with nanoparticles like gold allows for the EVs to be imaged using CT, while labeling EVs with SPIO nanoparticles allows for imaging with MRI or MPI, a novel imaging technique specific to SPIOs<sup>35,39,42,44</sup>. It is important to note that these imaging techniques do not image the EVs directly, but rather image a probe associated with the EVs intended to be imaged, therefore it is important to confirm that those probes are associated with the EVs.

This dissertation focuses on the potential targeting capabilities and use as a therapeutic delivery tool of EVs in three different cases: breast cancer tumor cell-derived EVs retention in

breast cancer tumors, brain-seeking breast cancer tumor cell-derived EVs accumulation in a model of breast cancer-derived brain metastasis, and accumulation of immune cell EVs in heart organoids experiencing myocardial infarction-like conditions. For the first two cases, EVs were labeled with SPIOs for *in vivo* MPI, and the association of the SPIOs with the EVs is confirmed using transmission electron microscopy. MPI was used to determine the distribution and accumulation of these EVs. The third case used EVs derived from human monocyte-like cells transfected with nucleic acid for firefly luciferase for bioluminescent imaging. Delivery of these EVs was determined by expression of bioluminescence in recipient human heart organoids. This work builds upon previous work in the field showing the potential for EVs as a therapeutic delivery tool in cancer and inflammation through imaging.

## REFERENCES

1. Allen, T. M. & Cullis, P. R. Drug Delivery Systems: Entering the Mainstream. *Science* vol. 303 1818–1822 (2004).
2. Vargason, A. M., Anselmo, A. C. & Mitragotri, S. The evolution of commercial drug delivery technologies. *Nat. Biomed. Eng.* 2021 59 5, 951–967 (2021).
3. Sung, Y. K. & Kim, S. W. Recent advances in the development of gene delivery systems. *Biomater. Res.* 2019 231 23, 1–7 (2019).
4. Ramamoorth, M. & Narvekar, A. Non viral vectors in gene therapy - An overview. *Journal of Clinical and Diagnostic Research* (2015) doi:10.7860/JCDR/2015/10443.5394.
5. Glover, D. J., Lipps, H. J. & Jans, D. A. Towards safe, non-viral therapeutic gene expression in humans. *Nature Reviews Genetics* (2005) doi:10.1038/nrg1577.
6. Barenholz, Y. Doxil® — The first FDA-approved nano-drug: Lessons learned. *J. Control. Release* 160, 117–134 (2012).
7. Lee Ventola, C. Progress in Nanomedicine: Approved and Investigational Nanodrugs. 42, (2017).
8. Sercombe, L. et al. Advances and challenges of liposome assisted drug delivery. *Frontiers in Pharmacology* (2015) doi:10.3389/fphar.2015.00286.
9. Sajja, H. K. et al. Development of Multifunctional Nanoparticles for Targeted Drug Delivery and Non-invasive Imaging of Therapeutic Effect NIH Public Access. *Curr Drug Discov Technol* 6, 43–51 (2009).
10. Ventola, C. L. The nanomedicine revolution: Part 1: Emerging Concepts. *P T* 37, 512–518 (2012).
11. Bobo, D., Robinson, K. J., Islam, J., Thurecht, K. J. & Corrie, S. R. Nanoparticle-Based Medicines: A Review of FDA-Approved Materials and Clinical Trials to Date. *Pharm. Res.* 33, 2373–2387 (2016).
12. Luo, E. et al. The Toxicity and Pharmacokinetics of Carbon Nanotubes as an Effective Drug Carrier. *Curr. Drug Metab.* 14, 879–890 (2013).
13. Wu, Y. et al. Gold Nanoparticles in Biological Optical Imaging. (2018).
14. Yao, Y. et al. Nanoparticle-Based Drug Delivery in Cancer Therapy and Its Role in Overcoming Drug Resistance. *Front. Mol. Biosci.* 7, 193 (2020).

15. NCI to Conduct Phase 2 Studies of Cytimmune's lead nanomedicine, CYT-6091 — CYTIMMUNE SCIENCES. <https://www.cytimmune.com/news/blog-post-title-two-e3k3g>.
16. Madani, S. Y., Naderi, N., Dissanayake, O., Tan, A. & Seifalian, A. M. A new era of cancer treatment: carbon nanotubes as drug delivery tools. *Int. J. Nanomedicine* 6, 2963–2979 (2011).
17. Doyle, L. M. & Wang, M. Z. Overview of Extracellular Vesicles, Their Origin, Composition, Purpose, and Methods for Exosome Isolation and Analysis. *Cells* 8, (2019).
18. Théry, C. et al. Minimal information for studies of extracellular vesicles 2018 (MISEV2018): a position statement of the International Society for Extracellular Vesicles and update of the MISEV2014 guidelines. <https://doi.org/10.1080/20013078.2018.1535750> 7, (2018).
19. Herrmann, I. K., Wood, M. J. A. & Fuhrmann, G. Extracellular vesicles as a next-generation drug delivery platform. *Nat. Nanotechnol.* 2021 167 16, 748–759 (2021).
20. Chen, Y. S., Lin, E. Y., Chiou, T. W. & Harn, H. J. Exosomes in clinical trial and their production in compliance with good manufacturing practice. *Tzu-Chi Med. J.* 32, 113 (2020).
21. iExosomes in Treating Participants With Metastatic Pancreas Cancer With KrasG12D Mutation - Full Text View - ClinicalTrials.gov. <https://clinicaltrials.gov/ct2/show/NCT03608631>.
22. Trial of a Vaccination With Tumor Antigen-loaded Dendritic Cell-derived Exosomes - Tabular View - ClinicalTrials.gov. <https://clinicaltrials.gov/ct2/show/record/NCT01159288>.
23. Study Investigating the Ability of Plant Exosomes to Deliver Curcumin to Normal and Colon Cancer Tissue - Tabular View - ClinicalTrials.gov. <https://clinicaltrials.gov/ct2/show/record/NCT01294072>.
24. Nguyen, V. Du, Kim, H. Y., Choi, H., Park, J.-O. & Choi, E. Tumor-derived extracellular vesicles for the active targeting and effective treatment of colorectal tumors *in vivo*. *Drug Deliv.* 2022, 2621–2631 (2022).
25. Qiao, L. et al. Tumor cell-derived exosomes home to their cells of origin and can be used as Trojan horses to deliver cancer drugs. *Theranostics* 10, 3474 (2020).
26. Xie, X. et al. Tumor-derived exosomes can specifically prevent cancer metastatic organotropism. *J. Control. Release* 331, 404–415 (2021).

27. Zhao, L. et al. Exosome-mediated siRNA delivery to suppress postoperative breast cancer metastasis. *J. Control. Release* 318, 1–15 (2020).
28. Yong, T. et al. Tumor exosome-based nanoparticles are efficient drug carriers for chemotherapy. doi:10.1038/s41467-019-11718-4.
29. Kim, M. S. et al. Engineering macrophage-derived exosomes for targeted paclitaxel delivery to pulmonary metastases: *in vitro* and *in vivo* evaluations. *Nanomedicine Nanotechnology, Biol. Med.* 14, 195–204 (2018).
30. Haney, M. J. et al. Macrophage-Derived Extracellular Vesicles as Drug Delivery Systems for Triple Negative Breast Cancer (TNBC) Therapy. *J. Neuroimmune Pharmacol.* 15, 487–500 (2020).
31. Haney, M. J. et al. Exosomes as Drug Delivery Vehicles for Parkinson’s Disease Therapy HHS Public Access. *J Control Release* 207, 18–30 (2015).
32. Yuan, D. et al. Macrophage exosomes as natural nanocarriers for protein delivery to inflamed brain. *Biomaterials* 142, 1–12 (2017).
33. Banks, W. A. et al. Transport of Extracellular Vesicles across the Blood-Brain Barrier: Brain Pharmacokinetics and Effects of Inflammation. *Int. J. Mol. Sci.* 21, 1–21 (2020).
34. Morad, G. et al. Tumor-Derived Extracellular Vesicles Breach the Intact Blood-Brain Barrier via Transcytosis. *ACS Nano* 13, 13853–13865 (2019).
35. Chuo, S. T. Y., Chien, J. C. Y. & Lai, C. P. K. Imaging extracellular vesicles: Current and emerging methods. *J. Biomed. Sci.* 25, 1–10 (2018).
36. Varga, Z. et al. Radiolabeling of Extracellular Vesicles with <sup>99m</sup>Tc for Quantitative *In Vivo* Imaging Studies. <https://home.liebertpub.com/cbr> 31, 168–173 (2016).
37. Shi, S. et al. Copper-64 Labeled PEGylated Exosomes for *In Vivo* Positron Emission Tomography and Enhanced Tumor Retention. *Bioconjug. Chem.* 2675–2683 (2019) doi:10.1021/ACS.BIOCONJCHEM.9B00587/SUPPL\_FILE/BC9B00587\_SI\_001.PDF.
38. Busato, A. et al. Magnetic resonance imaging of ultrasmall superparamagnetic iron oxide-labeled exosomes from stem cells: a new method to obtain labeled exosomes. *Int. J. Nanomedicine* 11, 2481–2490 (2016).
39. Betzer, O. et al. *In Vivo* Neuroimaging of Exosomes Using Gold Nanoparticles. *ACS Nano* 11, 10883–10893 (2017).
40. Panagiotopoulos, N. et al. Magnetic particle imaging: current developments and future directions. *Int. J. Nanomedicine* (2015) doi:10.2147/ijn.s70488.

41. Bulte, J. W. M. Superparamagnetic iron oxides as MPI tracers: A primer and review of early applications. *Advanced Drug Delivery Reviews* (2019) doi:10.1016/j.addr.2018.12.007.
42. Jung, K. O., Jo, H., Yu, J. H., Gambhir, S. S. & Pratz, G. Development and MPI tracking of novel hypoxia-targeted theranostic exosomes. *Biomaterials* 177, 139–148 (2018).
43. Yuan, D. et al. Macrophage Exosomes as Natural Nanocarriers for Protein Delivery to Inflamed Brain HHS Public Access. *Biomaterials* 142, 1–12 (2017).
44. Marzola, P. et al. Magnetic resonance imaging of ultrasmall superparamagnetic iron oxide-labeled exosomes from stem cells: a new method to obtain labeled exosomes. *Int. J. Nanomedicine* (2016) doi:10.2147/ijn.s104152.
45. Kanada, M, Bachmann, MH, Hardy, JW, Bronsart, L, Wang, A, Frimannson, DO, Sylvester, MD, Schmidt, TL, Kaspar, RL, Butte, MJ, Matin, AC, Contag, CH (2015) Differential fates of biomolecules delivered to target cells via extracellular vesicles. *Proc Nat Acad Sci, USA*. 112(12): E1433-42. doi:10.1073/pnas.1418401112.

CHAPTER TWO:  
EXTRACELLULAR VESICLES FROM ISOLATED MAMMARY CARCINOMA CELLS  
ARE RETAINED FOR LONGER IN MAMMARY FAT PAD TUMORS COMPARED TO  
IRON ALONE

## **ABSTRACT**

Breast cancer is one of the most common cancers for women in the United States. Treatment of breast cancer is often dependent on the type of breast cancer, and various therapies exist, but remains imperfect. Delivery of chemotherapeutic drugs and retention of those drugs are areas being explored to improve treatment of breast cancer. Extracellular vesicles, or EVs, are one possible option for improving delivery and retention of chemotherapeutic agents. Extracellular vesicles are small particles released from cells, separated into three classes based on their method of biogenesis. As it is currently impossible to purposefully separate all three classes using ultracentrifugation, our method of isolating EVs, we will not distinguish our EVs between the classes, instead determining that we isolated small EVs. EVs from tumor cells and other types of cells have been used to deliver therapeutic agents to cancer before, but our study focuses on measuring retention using a novel imaging method, magnetic particle imaging (MPI). Magnetic particle imaging tracks superparamagnetic iron oxide nanoparticles (SPIOs), and is specific, directly quantifiable, and has no depth limit. In order to use MPI to track EVs, we labeled our EVs with SPIOs, as EVs are not inherently superparamagnetic.

Breast cancer cells expressing firefly luciferase (4T1-fLuc2) or firefly luciferase and green fluorescent protein (4T1-BGL) were labeled with 70 nm dextran-coated synomag-D SPIOs using a combination of heparin and protamine sulfate. 4T1-fLuc2 and 4T1-BGL cells were washed with heparin and PBS 24-h post labeling, and EV-depleted media was added to the cells. 24-h later, iron-associated EVs were isolated from the media using differential ultracentrifugation. Transmission electron microscopy revealed that lipid membrane bound particles were associated with SPIOs, confirming the isolation of FeEVs. FeEVs or an equivalent iron amount of SPIOs were injected via the tail vein into healthy mice, and observed over 7-day.

Both the SPIOs and FeEVs were located in the liver of the healthy mice, and could be detected for at least 7-days. Tumors were established by injecting mouse breast cancer 4T1-BGL or 4T1-fLuc2 cells into the mammary fat pad and allowed to grow for three weeks. Injection of FeEVs into the tail vein of the mice (n=4) did not seem to result in any iron signal in the tumor. FeEVs (n=5) or equal iron amounts of FeEVs (n=3) were injected into directly into the tumor, and signal was measured immediately post-injection, 24-h, and 72-h post-injection. FeEVs were retained in the tumor for longer and in greater iron amounts compared to SPIOs. Slicing the tumor revealed that FeEVs were present in both CD47<sup>+</sup> tumor cells and CD11b<sup>+</sup> macrophages, while no SPIOs could be detected in the tumor across multiple sections. Tumor cells EVs allow for therapeutics to be contained in breast cancer tumors for longer, and in greater amounts in both tumor cells and tumor-associated macrophages, making them an interesting delivery tool for therapeutic delivery to breast cancer.

## INTRODUCTION

In 2020, female breast cancer represented 11.7% of all new cases of cancer worldwide, the highest among all types of cancer<sup>1,2</sup>. It was responsible for 685,000 deaths worldwide in that same year<sup>1,2</sup>. Women in the United States have a 12.9% lifetime risk of breast cancer, with 287,850 new cases predicted in the United States in 2022<sup>3</sup>. It was further predicted that 43,250 of these women will die of this disease in 2022.<sup>3</sup>

There are three major subtypes of breast cancer, which are based on presence of certain hormonal markers or human epidermal growth factor (HER2) molecular markers<sup>4</sup>. Tumors that are positive for hormonal markers but negative for HER2 are termed HR+HER2- and represent 60-70% of patients, tumors that are negative for hormonal markers but positive for HER2 are termed HR-HER2+ and represent 15-20% of patients, and tumors that are negative for both types of markers are termed triple negative (TN), representing 15-20% of all patients<sup>4,5</sup>. The type of breast cancer affects treatment, as well as the odds of recurrence, with TN breast cancer having the highest rate of recurrence.

Treatment is also dependent on whether or not the cancer is metastatic. For non-metastatic tumors, local therapies may be used, such as surgery or radiation therapy. Surgery typically consists of a total mastectomy or excision of the tumor area with radiation for any potentially missed tumor cells. The axillary lymph nodes may be removed as well. For radiation, it is typically used after a lumpectomy or a mastectomy. The benefits of radiation remained the same across all patients in proportion to their risk<sup>5</sup>. There are also systemic therapies for non-metastatic breast cancer<sup>5</sup>. For HR+HER2- subtypes, endocrine therapy is most common. This includes tamoxifen and aromatase inhibitors<sup>5</sup>. Chemotherapy is also be used in conjunction with endocrine therapy. For the other subtypes, chemotherapy is most common.

Nanotherapeutic delivery tools are also used for breast cancer, such as liposomes, dendrimers, micelles, carbon nanotubes, and polymer nanoparticles<sup>4</sup>. Liposome-based therapeutics approved for breast cancer include Doxil, LipoDox, and Myocet™, which all deliver doxorubicin<sup>4</sup>. Dendrimer-based therapeutics, micelle-based therapeutics, and polymer-based therapeutics are in clinical trials<sup>4</sup>. Carbon nanotube-based therapeutics and polymeric nanoparticle-based therapeutics are not yet in clinical trial, but have shown promising results in *in vitro* studies<sup>4</sup>.

As discussed, EVs are a potential therapeutic delivery tool, with clinical trials investigating their use as a delivery tool<sup>6-9</sup>. EVs from tumor cells specifically have also been used to target cancer<sup>10-13</sup>. In this study, iron labeled EVs<sup>14,15</sup> (FeEVs) from breast cancer cells were injected into tumors of mice bearing mammary carcinomas<sup>16</sup>. The MPI signal from FeEVs or SPIOs as a control was quantified<sup>17</sup> over 72h, and the distribution of the FeEVs and SPIOs was examined in the tumor.

## **RESULTS**

Briefly, 4T1-fLuc or 4T1-BGL were seeded at approximately  $3 \times 10^6$  cells per dish. 24h after seeding, a mix of protamine sulfate, heparin, and SPIOs were added to the cells with no serum, with serum being added 3-6-h later. EV-depleted media was added to the iron-labeled cells, which were allowed to release EVs associated with iron (FeEVs) for 24 hours. EVs were then isolated through a series of differential centrifugation steps, before being resuspended in phosphate buffered saline (PBS).

FeEVs were then analyzed using nanoparticle tracking analysis (NTA) to give an estimation of the size distribution and the particle count. The size distribution for 4T1-fLuc and

4T1-BGL FeEVs are seen in Figure 2.1. The average particle count for each type was on the scale of  $10^8$  particles/ml.

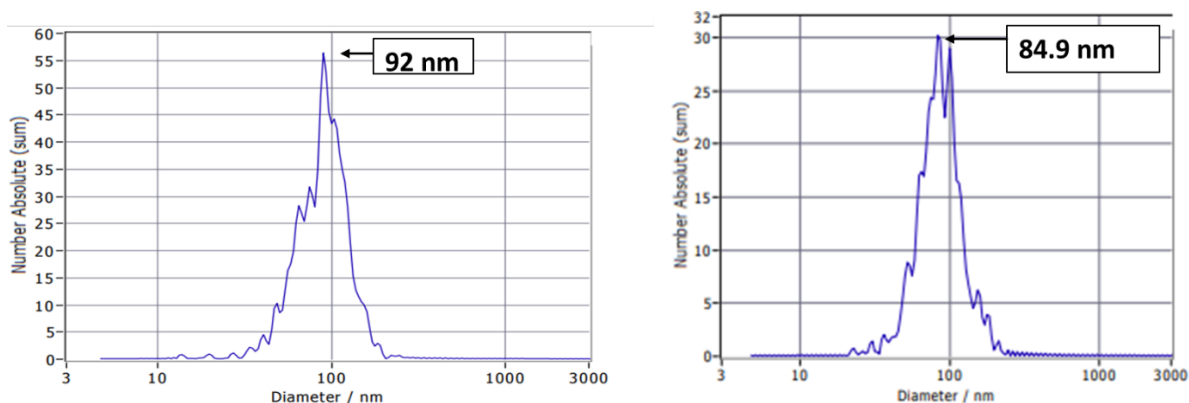


**Figure 2.1.** Nanoparticle tracking analysis of 4T1-fLuc FeEVs (left) and 4T1-BGL FeEVs (right) shows the size distribution of the FeEVs, measured across 11 fields of view twice.

FeEVs and plain SPIOs (Figure 2.2) were visualized using transmission electron microscopy. The FeEVs were stained with uranyl acetate for negative contrast. Briefly, iron nanoparticles in a flower-like shape can be seen associated with dark circular particles, believed to be uranyl acetate stained EVs. These dark particles are much larger than the SPIOs, which also points to them being something other than iron. Proteomic analysis of these EVs shows that FeEVs contain many common EV-associated proteins (Figure 2.3)

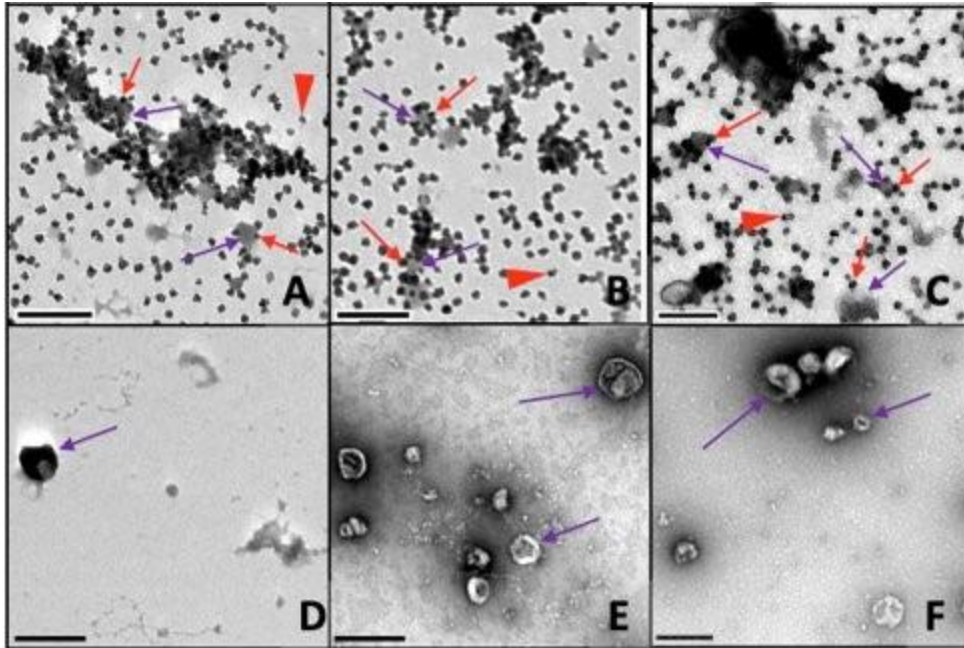


**Figure 2.2.** Visualization of 4T1-fluc EVs. Images of EVs from 4T1-fluc cells were captured via transmission electron microscopy (TEM) in biological triplicates with iron (Fe-EVs;A-C) and unlabelled (D-F). Red arrows indicate iron associated with EV membranes (A-C) while purple arrows show EVs  $\pm$  iron (A-F). Red triangles indicate free iron (A-C). Scale bars = 250 nm; magnification = 15,000X (A-F).

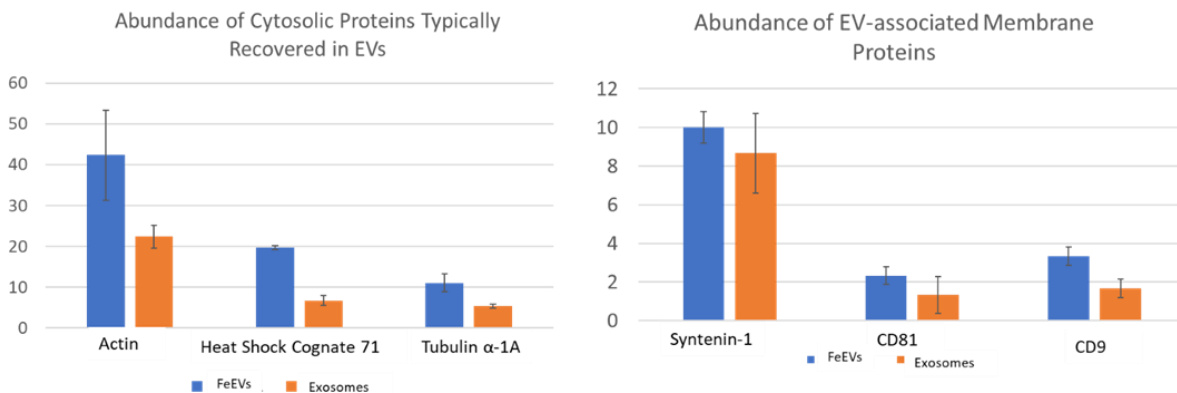


**Figure 2.3.** Abundance of cytosolic (left) and membrane-associated (right) proteins in the FeEVs and EVs as determined by proteomic analysis.

FeEVs from  $3 \times 10^6$  cells per mouse ( $n=2$ ) were injected into the tail veins of healthy mice. The distribution was then observed using MPI and  $\mu$ -CT 24h-, 48h-, and 72h-post-injection. All signal appears to be concentrated in the liver, based on the location and shape of the signal. 8.2  $\mu$ g of 70 nm dextran-coated Synomag-D was injected into the tail vein of another healthy Balb/C mouse. All signal was again seen in the lower abdomen, approximately in the area and shape of the liver. Visually, the FeEVs and SPIOs seemed to clear at the same rate as each other and accumulated in similar amounts (Figure 2.4).

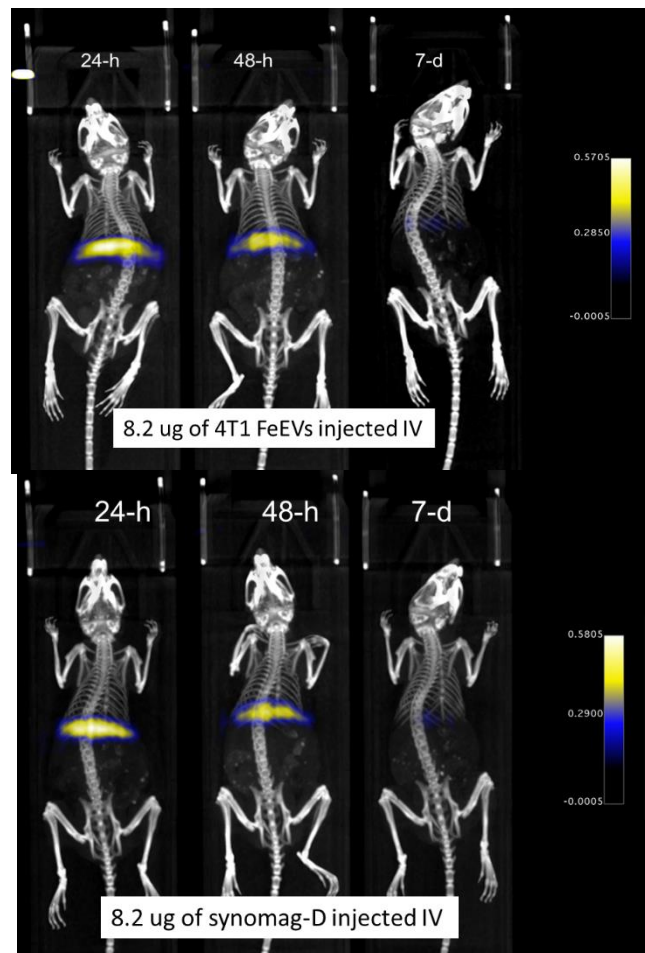


**Figure 2.4.** Distribution of (A) SPIOs (8.2  $\mu$ g Synomag-D) or (B) FeEVs from 4T1-BGL cells (8.2  $\mu$ g Fe) when injected IV over 7 days, determined by an overlay of MPI and micro-CT scans for the iron signal and anatomical information, respectively.

$3 \times 10^5$  4T1-BGL cells/mouse were injected into the mammary fat pad of six mice and allowed to grow into tumors for three weeks. Tumors only developed in two mice, which were both injected in the tail vein with 4T1-BGL FeEVs, equivalent to  $1.25 \mu\text{g}$  of iron, 6.5 fold less than injected previously. No iron was seen in the tumors when injected with FeEVs in the tail vein, 24h and 48h post-injection, despite bioluminescence from the tumor being seen when using BLI (Figure 2.5). The tumors were removed and scanned in the MPI ex vivo, and once again expressed no iron signal with MPI.

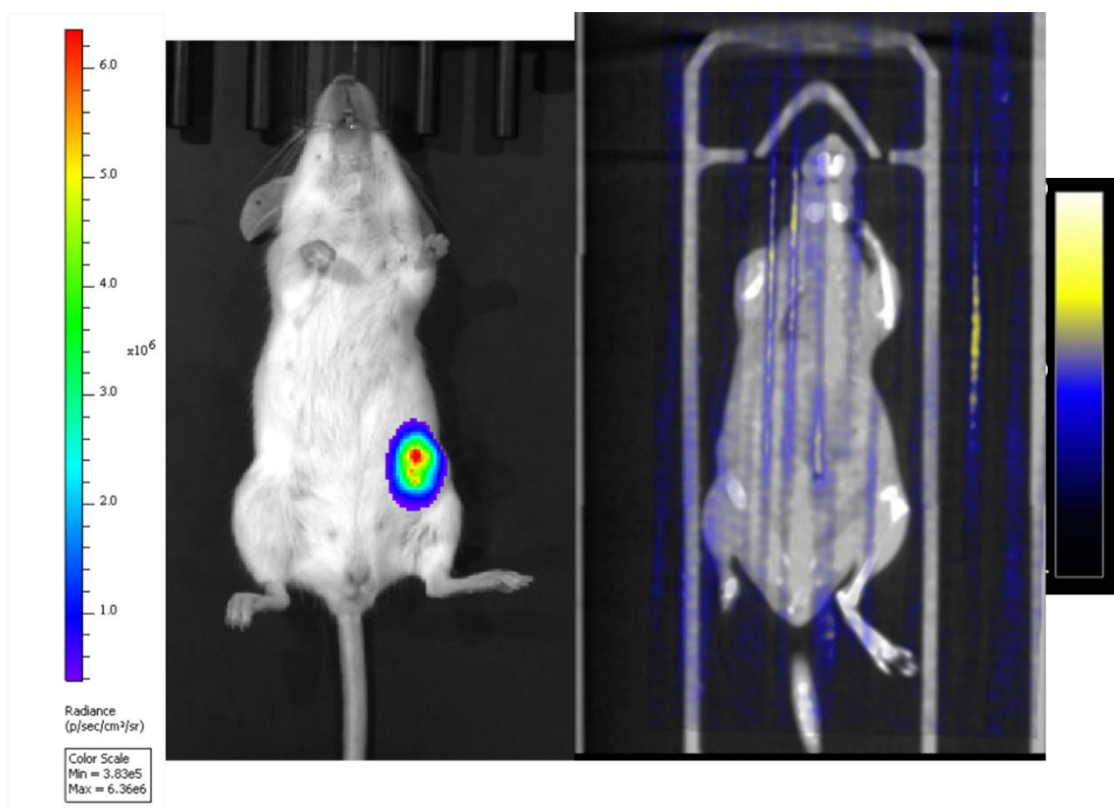


**Figure 2.5.** Overlay of MPI and micro-CT (left) of BalB/C tumor-bearing mouse injected IV with 4T1-BGL FeEVs shows no iron signal visible in the body. Bioluminescence imaging (right) confirms presence of tumor due to the cells stably expressing firefly luciferase.

$3 \times 10^5$  4T1-fLuc cells were injected into the mammary fat pad of 10 mice and tumors were again allowed to grow for 3 weeks in the Balb/C mice.  $3 \times 10^6$  4T1-fLuc2 cells/mouse

were labeled with 70 nm dextran-coated Synomag-D that was far-red fluorescently tagged. Two mice were injected with FeEVs i.v. into the tail vein, while five mice were injected with FeEVs intratumor (i.t.). The final three mice were injected with equal amounts of iron of SPIOs i.t. Iron signal in the mouse was observed immediately after injection, 24h-, and 72h- post-injection via MPI. A representative overlay of iron signal from the MPI and anatomical information from the  $\mu$ -CT is seen in Figure 2.6. Amount of iron in the tumor was calculated by calculating the average background signal, multiplying that by five, and then using that amount to determine a base signal for the Osiris imaging software to automatically detect above, which draws its own ROI. The total signal is calculated by multiplying the average signal by the area. This was done for each mouse, with the background being calculated for every day that was imaged. The amount of signal and iron were calculated for each mouse, then compared to the amount of signal detected upon injection, as the amounts of signal in each tumor differed from each other. One mouse from the FeEV group was cut from analysis because it had signal in the gut that appeared to be from iron contamination that resulted in an extended ROI being detected, including signal outside the tumor, so the results could not be trusted from that mouse.

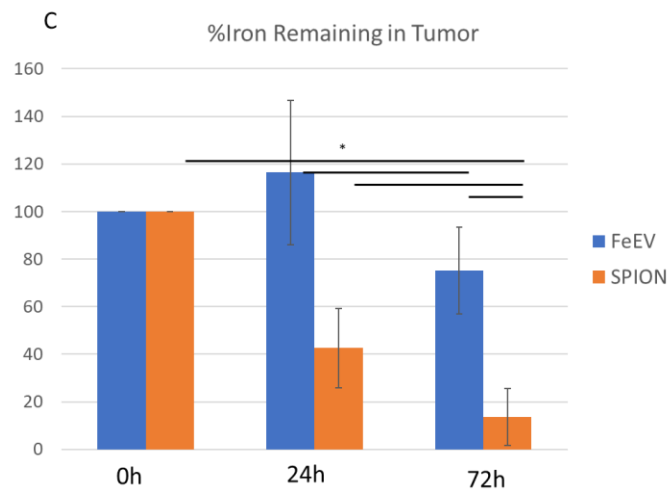
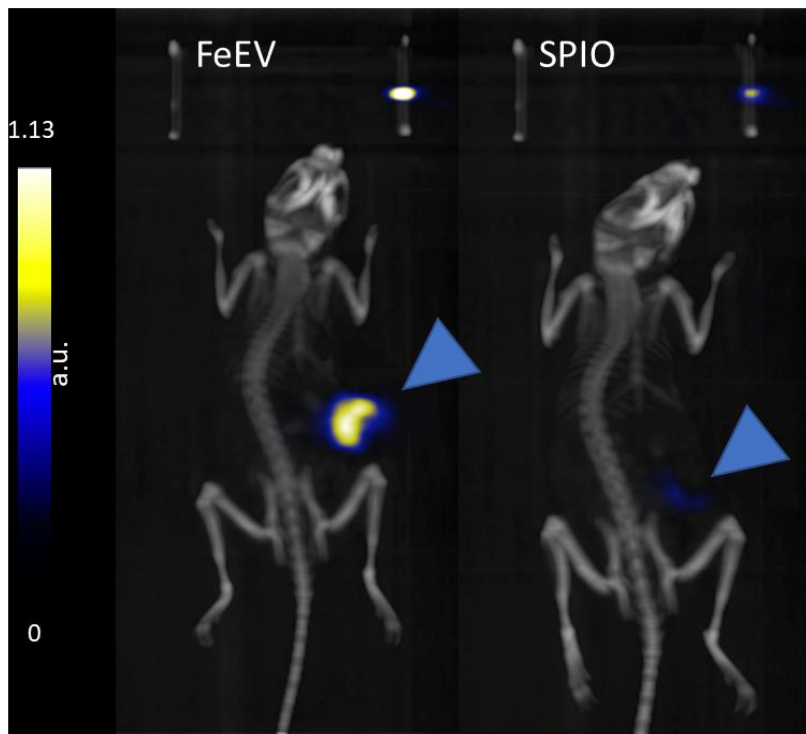


**Figure 2.6.** Identification and quantification of iron from FeEVs or SPIOs in primary mammary fat pad (MFP) tumors. Overlay images of micro-CT and MPI scans of mice bearing 4T1 MFP tumors with FeEVs (n=4) (A) or SPIOs (n=3) (B), 24h post injection (arrowhead indicates location of MFP tumor). More signal is retained in the tumor over 72h when FeEVs are injected vs SPIO only (C). \*p<0.05.

Tumors from each mouse were excised post-mortem, which occurred immediately after the 72-h time point imaging. They underwent sucrose treatment, before being flash frozen for tissue slicing. After sectioning, tissues were transferred to glass slide and the slides were scanned for far-red fluorescence as an indicator of the presence of FeEVs or SPIOs. No far-red fluorescence could be observed after direct injection of SPIOs into the tumors, which was expected based on the lack of iron signal seen from the MPI. Spots of far-red fluorescence, from the iron nanoparticles, is seen in sections of tumors in which the FeEVs were directly injected. One tissue section was stained with CD11b to look for macrophages, typically seen in tumors, and another slice was stained with CD47 to identify tumor cells. Fluorescent nanoparticles could be seen inside both CD11b+ macrophages and CD47+ tumor cells when the tumors were injected with FeEVs (Figure 2.7).

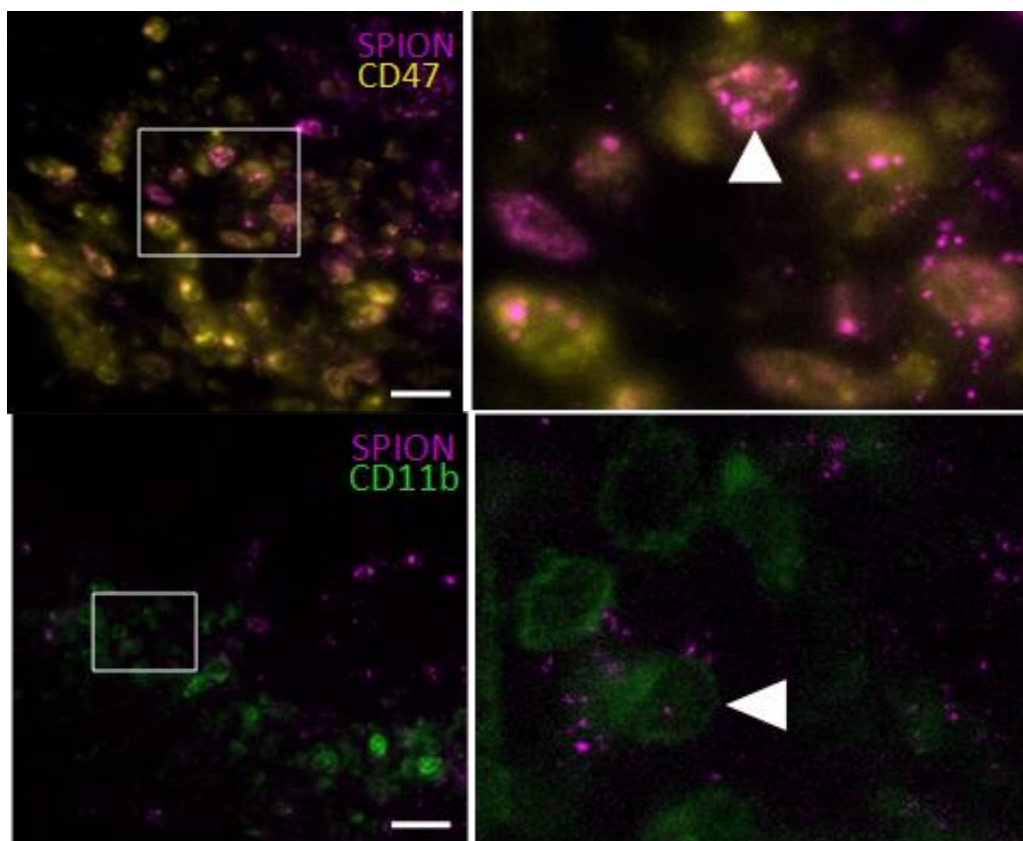


**Figure 2.7.** Immunofluorescence staining of tumor sections showed little to no iron when SPIONs only were injected (not shown). Fluorescent SPION associated with FeEVs (magenta) are identified in few CD11b+ macrophages (green) (D) and to a larger extent in CD47+ tumor cells (yellow) (E). Zoomed insets identify iron-labeled cells (arrowheads). Scale bars: 50  $\mu$ m.

## DISCUSSION

FeEVs were characterized by their physical size and their protein composition. Nanoparticle tracking analysis shows the average size of the FeEVs isolated from 4T1-fLuc2 and 4T1-BGL cells are larger than the nanoparticle alone, and have a size peak of 92 nm and 84.9 nm, respectively, which is within the typical small EV size range of 50-150 nm. This indicates that another small particle, that is not the iron nanoparticle, was isolated by differential centrifugation.

TEM was performed on 4T1-fLuc2 FeEVs to identify iron associated with EVs. Uranyl acetate was used to stain the lipid membranes of the EVs so they could be visualized, while iron is a heavy element so it can appear under TEM on its own. Iron particles can clearly be seen associated with the EVs, although TEM does not allow us to determine if the iron particles are inside the EVs or outside attached to the surface. The EVs are too small to slice through, which would normally be used to determine the location of iron particles. Because it is not certain that the SPIOS are contained within the EVs, we only claim our FeEVs associated with iron. Nonetheless, almost every EV seen is heavily associated with iron. The process of isolating the EVs, fixing the EVs, or attaching them to the EM-grids and the following wash steps resulted in mostly clumps of FeEVs being visualized. It is likely that the FeEVs were not clumped in suspension due to the NTA results showing individual EV sizes, not the size of the clumps seen.

To test the base biodistribution in healthy mice, FeEVs were isolated from 4T1-BGL cells and injected via the tail vein into mice (n=2). The FeEVs were determined by MPI to contain 8.2  $\mu\text{g}$  of iron per dose, and so 8.2  $\mu\text{g}$  of the 70 nm dextran coated synomag-D were injected into the tail vein of one mouse (n=1). The iron signal in all mice was measured by MPI 24-h, 48-h, and 7-d post injection, and overlaid with micro-CT scans to determine the source of the signal. For both the FeEVs and SPIOs, signal could be observed for at least 7 days and was only seen in the liver. This is expected as the liver acts to filter blood, absorbing the foreign FeEVs since there is no tumor for them to localize to. EVs from cancer cells have previously been reported to help establish pre-metastatic niches or tumor niches, but this was not observed in this initial study. It is possible that a larger group of animals would have resulted in this observation, or it is possible that there is other iron signal in the mouse that is being masked by

the high iron signal of the liver. Nonetheless, iron signal from FeEVs and SPIOs could be observed over 7 days and appeared to only be located in the liver.

Tumors were established by injecting 2E4 4T1-BGL cells into the mammary fat pad. The tumors were allowed to grow for three weeks prior to FeEV injection, and growth was monitored every few days. The bioluminescence of the tumor was also measured by IVIS 15 minutes post-injection of D-luciferase (30 mg/kg). Only two out of six mice developed tumors, so both were injected with FeEVs from  $6 \times 10^6$  4T1-BGL cells per mouse in the tail vein i.v. Initial MPI scans of the mice showed signal in the liver area, which unfortunately was very close to the location of the tumors. Because the liver absorbs so much of the FeEV and the SPIOs, it was impossible to distinguish the possible tumor signal from the liver signal. High amounts of signal in one location can mask signal in other locations by adjusting the scale bar to reflect the highest points of signal, and then adjusting to display lower amounts of signal results in the areas with high signal extending outwards, making any points near the large signal masked by that effect. In order to determine if the tumor did take up any FeEVs, the tumors were removed post-sacrifice and imaged with MPI *ex vivo*. Unfortunately, no iron signal was detected in the tumors. Other studies have shown SPIO uptake by tumors that could be detected in MPI, but we injected significantly less iron than they did due to constraints when creating the FeEVs, and so the amount of signal in the tumor is much lower and could not be detected.

For this reason, FeEVs and fluorescently labeled dextran-coated synomag-D SPIOs were injected intra-tumor three weeks post tumor initiation of Balb/C mice with 4T1-fLuc cells. Injecting intra-tumor does not address any targeting effect, but allows for evaluation of retention in the tumor and the ability to determine which cells take up the FeEVs, which are both very important for evaluation as a drug delivery tool. Tumors were established by injecting 2E4 4T1-

fLuc cells into the mammary fat pad, and allowed to grow for three weeks, before being injected intratumor with FeEVs isolated from 4T1-fLuc 3E6 cells per mouse or an equivalent amount of iron, as determined by MPI. Each mouse was imaged immediately post-injection of FeEVs or SPIOs, and then 24-h and 72-h post injection of FeEVs or SPIOs.

As seen, the FeEVs were retained in the tumor for both longer and in greater amounts compared to the SPIOs. This indicates that something about the association with EV membranes allows the FeEVs to stay in the tumor for longer. Slicing the tumor and immunocytochemistry of the resultant slices revealed that the FeEVs were present in both CD11b+ tumor associated macrophages and CD47+ tumor cells, which could be the reason for the enhanced uptake and retention. Unfortunately, we could not find iron in the macrophages or tumor cells of mice injected with SPIOs. This is not unexpected, as MPI scanning of these mice showed very little, if any, iron signal coming from the tumor. While there is likely SPIOs present, they could not be found in any of the tumor that we sectioned. Sectioning the whole tumor and scanning each slice would possibly locate any remaining iron, but other studies have shown that the SPIOs are typically only present in the TAMs and not the tumor cells themselves.

## **CONCLUSIONS AND FUTURE WORK**

FeEVs were retained for longer in a primary breast tumor compared to SPIOs alone, possibly due to the fact that FeEVs are taken up by the tumor cells themselves. Further work in this area would involve using the FeEVs to deliver a therapeutic, or attempting to treat the tumor with thermal ablation. FeEV could be shown to be a successful therapeutic delivery vehicle in this case.

## **MATERIALS AND METHODS**

### **Cell Culture**

4T1-fLuc2 cells were gifted by Dr. Brian Smith and 4T1-BGL cells were gifted by Dr. Michael Bachmann at Michigan State University. The cells were maintained in incubators set at 37°C with 5% CO<sub>2</sub>. They were cultured in RPMI140+Glutamax with 10% fetal bovine serum. For passaging, cells were washed with PBS and incubated with 5% Trypsin-EDTA for 5 minutes, before isolating via centrifugation. Cell counting was performed with a Trypan Blue Live/Dead stain and the number of live cells was utilized when plating specific numbers of cells.

### **Iron Labeling**

Cells were seeded at 3E6 cells/dish 24 hours before labeling. Protamine sulfate was added to 2.5 ml of FBS-free media per dish, and heparin and 70 nm dextran-coated Synomag-D (1 mg/ml Fe) or 70 nm dextran-coated far-red fluorescently labeled Synomag-D (1 mg/ml Fe) were added to 2.5 ml of FBS-free media per dish. Both tubes were well mixed, before the protamine sulfate mixture was added to the heparin and synomag-D mixture. 5 ml of this mixture was added to each plate. 5 ml of complete media was added 3-6 hours later.

### **FeEV Isolation**

24 hours post-addition of iron to cells, the cells were washed 3 times with 10 U/ml heparin to collect free iron and once with PBS. 10% EV-depleted FBS and RPMI-Glutamax were added to the cells and allowed to sit for 24 hours. The EV-containing media underwent differential centrifugation to isolate the Fe-EVs. The media was removed and spun at 600g for 10 minutes to remove any cells. It was then spun at 2,000g for 20 minutes to remove any remaining cells and apoptotic bodies. The remaining media was spun at 20,000g for 1 hr to pellet the

FeEVs, which were then resuspended and mixed together and spun again at 20,000g for 1 hour further concentrate the FeEVs, before resuspending in PBS.

### **EV Isolation**

3E6 4T1-fLuc cells were seeded in a 10 cm dish. 48 hours after seeding, the cells were washed twice with PBS to remove traces of media, and replaced with RMPI640 with 10% EV-depleted FBS. The cells were allowed to secrete EVs for 24 hours before the media was removed for EV isolation. The media was spun at 600g for 10 min to remove cells and at 2,000g for 20 min to remove apoptotic bodies. The supernatant was then spun at 20,000g for 1h to isolate the EVs. EVs were then combined and spun again at 20,000g for 1h to concentrate the EVs. Supernatant was removed and spun at 100,000g for 90 min to isolate a fraction of EVs that we termed exosomes. These exosomes were then washed with PBS and isolated at 100,000g for 90 minutes to pellet them before resuspension in PBS.

### **Transmission Electron Microscopy**

FeEVs were prepared in biological replicates using three dishes of  $3 \times 10^6$  4T1-fLuc2 cells each according to the protocol above. EVs from unlabeled cells were also prepared according to the previous protocol in biological replicates using three dishes of  $3 \times 10^6$  4T1-fLuc2 cells. These EVs were then concentrated at 20,000g for 30 min, before resuspension in EM-grade 16% paraformaldehyde. The EVs and FeEVs were incubated on EM grids for 10 min before being washed in EM-grade PBS, and then added to 1% glutaraldehyde for 5 min. After this second fixation, the grids were washed with distilled water eight times for 1 min each. The grids were then stained with uranyl acetate for 1 min for negative contrast of the EV membranes.

## ***In Vivo* Studies**

6-week old female Balb/C mice were purchased from Charles River Laboratories, and kept in the MSU animal facilities with approval from the MSU Institutional Animal Care and Use Committee.

For the initial *in vivo* study, FeEVs from 3E6 4T1-BGL cells (n=2) or equal iron amounts of Synomag-D (n=1, 8.2  $\mu$ g) were injected IV into the tail vein while the mice were under 2% isoflurane anesthesia. The mice were imaged via MPI using the standard 3D and 2D imaging mode and  $\mu$ -CT 24h, 48h, and 7-d post initial injection to observe the biodistribution under 2% isoflurane. Standards of known iron amount were placed in the MPI bed in order to coregister the  $\mu$ -CT and MPI 3D scans.

Tumors were established in six Balb/C mice by injecting  $2 \times 10^4$  4T1-BGL cells into the mammary fat pad, and allowed to grow for three weeks. Tumors only grew in two mice, which were then injected into the tail vein with FeEVs from  $6 \times 10^6$  cells each (n=2), before imaging with the standard 2D and 3D imaging mode in MPI. The mice were sacrificed using 5% carbon monoxide, and underwent post-mortem dissection to remove the livers and tumors. The tumors were later scanned on the MPI using the standard 2D imaging mode.

Tumors were then established in ten Balb/C mice by injecting  $2 \times 10^4$  4T1-fLuc cells into the mammary fat pad. Three weeks post-tumor initiation, FeEVs were injected into the tail vein (n=2), directly injected in the tumor (n=5), or SPIOs were injected directly into the tumor (n=3). These mice were imaged with MPI and  $\mu$ -CT immediately-, 24h-, and 72h-post-injection. After the 72h imaging, the mice were sacrificed using 5% CO and dissected post-mortem to remove the liver and the tumors, which were then placed in 4% paraformaldehyde (PFA) for tissue fixation. The 4% PFA was removed one week later and replaced with PBS.

## **Determination of Iron Signal**

Known amounts of iron were pelleted and imaged with MPI on various imaging methods to establish a curve for each scan type utilized: standard 2D, standard 3D, high signal 2D, and high signal 3D. The signal from each pellet was determined using the free and open source Horos software. Background signal was calculated by taking the average signal of an area of the scan with no iron present and multiplied by 5 to determine the base amount of signal that should be detected. This was used with the autocalculate tool in Horos to quantify the amount of signal detected instead of drawing an ROI, which is more accurate. The signal detected was plotted against the known amount of iron to create an equation for determining iron amount for each type of scan.

## **Tumor Sectioning and Staining**

Isolated tumors from mice injected intratumor with FeEVs or SPIOs were placed in 10%, 20%, and 30% sucrose for 24 hours each. Tumors were then placed in a bed of OCT, before being flash frozen in a mixture of dry ice and ethanol. The frozen tumors were stored at -20°C in preparation for tissue sectioning using the Leica CM3050 S. The slices were added to positively charged slides, and screened using the Leica Thunder for far-red expression from the iron nanoparticles.

Tissue sections with far-red expression from the iron nanoparticles were washed with PBS for 5 min, before being added to 0.3% triton X-100 in PBS and incubated for 45 min. Blocking buffer consisting of 5% goat serum and 0.3% triton X-100 in PBS was then added to the slides for 60 min. Diluted anti-CD47 or anti-CD11b were then added to the slides overnight at 4°C. The slides were then washed with PBS three times for five minutes each, and fluorescent goat anti-rat IgG secondary antibody (1:500) was added. The slides were then incubated for 2hr

in the dark, before three additional PBS washes. The slides were then mounted with a coverslip using Fluoromount, which was allowed to dry overnight before imaging.

### **Image Analysis**

Analysis of tumor sections and staining were performed using Fiji. This software allowed for the different fluorescence channels to be overlaid, as well as zooming in on cells of interest.

### **Proteomics Analysis**

Proteomics analysis was performed by the MSU Proteomics Core using biological triplicate samples. Resulting proteins had a literature search performed to determine the function of each protein and its relevance to the study.

## REFERENCES

1. Sung, H. et al. Global Cancer Statistics 2020: GLOBOCAN Estimates of Incidence and Mortality Worldwide for 36 Cancers in 185 Countries. *CA Cancer J Clin* 71, 209–249 (2021).
2. Wilkinson, L. & Gathani, T. Understanding breast cancer as a global health concern. *British Journal of Radiology* 95, 20211033 (2022).
3. Giaquinto, A. N. et al. Breast Cancer Statistics, 2022. *CA Cancer J Clin* 72, 524–541 (2022).
4. Tagde, P. et al. Nanomedicine-Based Delivery Strategies for Breast Cancer Treatment and Management. *International Journal of Molecular Sciences* 2022, Vol. 23, Page 2856 23, 2856 (2022).
5. Waks, A. G. & Winer, E. P. Breast Cancer Treatment: A Review. *JAMA* 321, 288–300 (2019).
6. Chen, Y. S., Lin, E. Y., Chiou, T. W. & Harn, H. J. Exosomes in clinical trial and their production in compliance with good manufacturing practice. *Tzu-Chi Medical Journal* 32, 113 (2020).
7. iExosomes in Treating Participants With Metastatic Pancreas Cancer With KrasG12D Mutation - Full Text View - ClinicalTrials.gov. <https://clinicaltrials.gov/ct2/show/NCT03608631>.
8. Trial of a Vaccination With Tumor Antigen-loaded Dendritic Cell-derived Exosomes - Tabular View - ClinicalTrials.gov. <https://clinicaltrials.gov/ct2/show/record/NCT01159288>.
9. Study Investigating the Ability of Plant Exosomes to Deliver Curcumin to Normal and Colon Cancer Tissue - Tabular View - ClinicalTrials.gov. <https://clinicaltrials.gov/ct2/show/record/NCT01294072>.
10. Yong, T. et al. Tumor exosome-based nanoparticles are efficient drug carriers for chemotherapy. doi:10.1038/s41467-019-11718-4.
11. Qiao, L. et al. Tumor cell-derived exosomes home to their cells of origin and can be used as Trojan horses to deliver cancer drugs. *Theranostics* 10, 3474 (2020).
12. Zhao, L. et al. Exosome-mediated siRNA delivery to suppress postoperative breast cancer metastasis. *Journal of Controlled Release* 318, 1–15 (2020).
13. Xie, X. et al. Tumor-derived exosomes can specifically prevent cancer metastatic organotropism. *Journal of Controlled Release* 331, 404–415 (2021).

14. Gutova, M. et al. Magnetic Resonance Imaging Tracking of Ferumoxytol-Labeled Human Neural Stem Cells: Studies Leading to Clinical Use. *Stem Cells Transl Med* 2, 766 (2013).
15. Jung, K. O., Jo, H., Yu, J. H., Gambhir, S. S. & Pratz, G. Development and MPI tracking of novel hypoxia-targeted theranostic exosomes. *Biomaterials* 177, 139–148 (2018).
16. Tao, K., Fang, M., Alroy, J. & Gary, G. G. Imagable 4T1 model for the study of late stage breast cancer. *BMC Cancer* 8, (2008).
17. Sehl, O. C. et al. MPI region of interest (ROI) analysis and quantification of iron in different volumes. doi:10.1101/2022.04.10.487778.

CHAPTER THREE:  
EXTRACELLULAR VESICLES FROM BRAIN METASTASIS CELLS DERIVED FROM  
MAMMARY CARCINOMA CELLS TARGET METASTASES ACROSS THE BLOOD  
BRAIN BARRIER

## **ABSTRACT**

Breast cancer remains one of the most common cancers for women worldwide. Death from breast cancer normally results from metastasis, of which brain metastasis is one of the most common causes of death. The average patient survival rate with brain metastasis from breast cancer remains low, with a median overall survival ranging from 4.9 to 18 months, depending on the subtype of breast cancer, even with treatment options such as surgery and radiation therapy available. This is in part due to the blood brain barrier (BBB) or blood-tumor-barrier (BTB), which may exclude targeted therapeutic agents, promoting a need for delivery tools that can help these therapeutics cross the BTB and allow them to enter the tumor. Extracellular vesicles, or EVs, are small particles naturally released from cells that have been investigated as therapeutic delivery vehicles, and have been shown to cross the BBB, which means they could be an excellent choice for a delivery vehicle to brain metastasis. In order to investigate this, EVs need to be tracked and quantified when a brain metastasis is present. Magnetic particle imaging (MPI) is a new sensitive and quantitative imaging method that specifically tracks superparamagnetic iron oxide nanoparticles (SPIOs). MPI can then be used to track and quantify EVs after they have been labeled with SPIOs, creating FeEVs.

Mouse breast cancer cells that metastasized to the brain and express firefly luciferase and green fluorescent protein (4T1BR5-fLuc/GFP) were labeled with fluorescent SPIOs using a combination of heparin and protamine sulfate. The cells were labeled for 24h before washing and replacing the iron containing media with EV-depleted media. The media was then collected 24h later and underwent differential centrifugation in order to collect the FeEVs. These FeEVs were then characterized by size, appearance, and protein composition. Under transmission electron microscopy (TEM), membrane-bound particles were seen associated with iron. Proteomic

analysis of those same particles had canonical EV markers as well as higher amounts of proteins associated with EV uptake into cells. Balb/C mice were injected intracardiac (IC) using ultrasound guidance with 4T1BR5-fLuc/GFP cells to establish brain metastasis *in vivo*. The resulting metastases were observed every 48h using bioluminescent imaging (BLI) to monitor tumor growth and spread. FeEVs were injected 7-9 days post-metastases initiation with FeEVs or an equal iron amount of SPIOs IC. In addition, healthy mice were injected IC with FeEVs to observe the distribution. Only mice with brain metastasis injected with FeEVs displayed iron signal in the brain 1-2h following injection. In conclusion, multimodal imaging revealed that association with EV membranes was required for iron to cross the BBB into a metastasis in our study, and improves delivery to other metastases.

## INTRODUCTION

The majority of deaths from breast cancer are caused by metastasis<sup>1</sup>, with 15-30% of these patients developing specifically metastases to the brain<sup>2</sup>. Brain metastasis is typically deadly, with the subtype of breast cancer contributing to the overall survival and the odds of developing a brain metastasis. The two most common groups to develop brain metastasis are HER2+/ER- and HER2-/ER- (triple negative, TN)<sup>3</sup>, with very different overall survival (OS) rates. For HER2+/ER- groups, the OS was 22 months, while for the TN group it was 6 months in a study performed by Leone et al.<sup>4</sup>. Interestingly, this group reported that HER2-/ER+ group accounted for the majority of brain metastasis patients (46.6% of 740 patients)<sup>4</sup>. Due to the low OS of TN patients who develop brain metastasis in combination with the high risk of developing brain metastasis, TN breast cancer will be focused on here.

Treatment of brain metastasis is very limited, and is divided into local and systemic treatments<sup>5</sup>. Current local options include surgical resection, stereotactic radiosurgery (SRS), and whole brain radiation therapy (WBRT)<sup>6</sup>, which are all difficult and have outcomes dependent on the number of lesions and location of those lesions. There is also the option of systemic treatments with cytotoxic chemotherapy, but the outcome of this therapy is highly dependent on the tumor subtype<sup>4</sup> and has difficulty reaching the brain due to the blood-brain barrier (BBB) or blood-tumor barrier (BTB)<sup>7</sup>. In the presence of a tumor, it is noted that the BBB is disrupted, forming what is then called the BTB<sup>7</sup>. The BTB experiences a loss in the tight junctions of the BBB, causing the BTB to be heterogeneously permeable, affecting accumulation of chemotherapies inside lesions. There may also be brain-specific drug resistance.<sup>7</sup>

As mentioned, EVs from tumor cells can target to metastases, as seen in cases with lung metastasis from breast cancer<sup>8,9</sup>. Brain-seeking breast cancer cells (4T1-BR5) were labeled with

iron to create FeEVs for imaging with magnetic particle imaging<sup>10-12</sup>. Protein analysis revealed an increase in proteins associated with These FeEVs were injected into mice bearing brain metastasis, and the amount of iron in the brain was determined<sup>13</sup>. Successful delivery of iron to the brain indicated that FeEVs may be used to target brain metastasis and successfully deliver the loaded material. FeEVs were not present in the brain when injected into healthy mice. SPIOs were also injected into mice with brain metastases which did not result in iron detected in the brain via MPI.

## **RESULTS**

FeEVs were created from 4T1BR5-fLuc/GFP cells, a type of breast cancer cell that had metastasized to the brain and express firefly luciferase and green fluorescent protein.  $3 \times 10^6$  cells were seeded per 10 cm dish, and a mix of far-red fluorescent 70 nm dextran-coated Synomag-D, heparin, and protamine sulfate was added 24h later in serum-depleted media. The iron-labeled cells were washed with 10 mg/ml heparin and PBS, before media made with EV-depleted FBS was added to the cells. The iron-labeled cells were allowed to secrete EVs for 24h before the media was collected and underwent differential ultracentrifugation to isolate the FeEVs.

The FeEVs were first characterized by size and amount using the nanoparticle tracking analysis, which uses Brownian motion to estimate particle size and counts multiple particles in different fields of view in order to determine the particle amount. NTA revealed peak sizes at 83 nm and 110 nm, indicating that the largest number of particles had sizes similar to that. There also appears to be a small peak around 70 nm, the hydrodynamic size of the SPIOs, but the majority of particles appear to be larger (Figure 3.1).

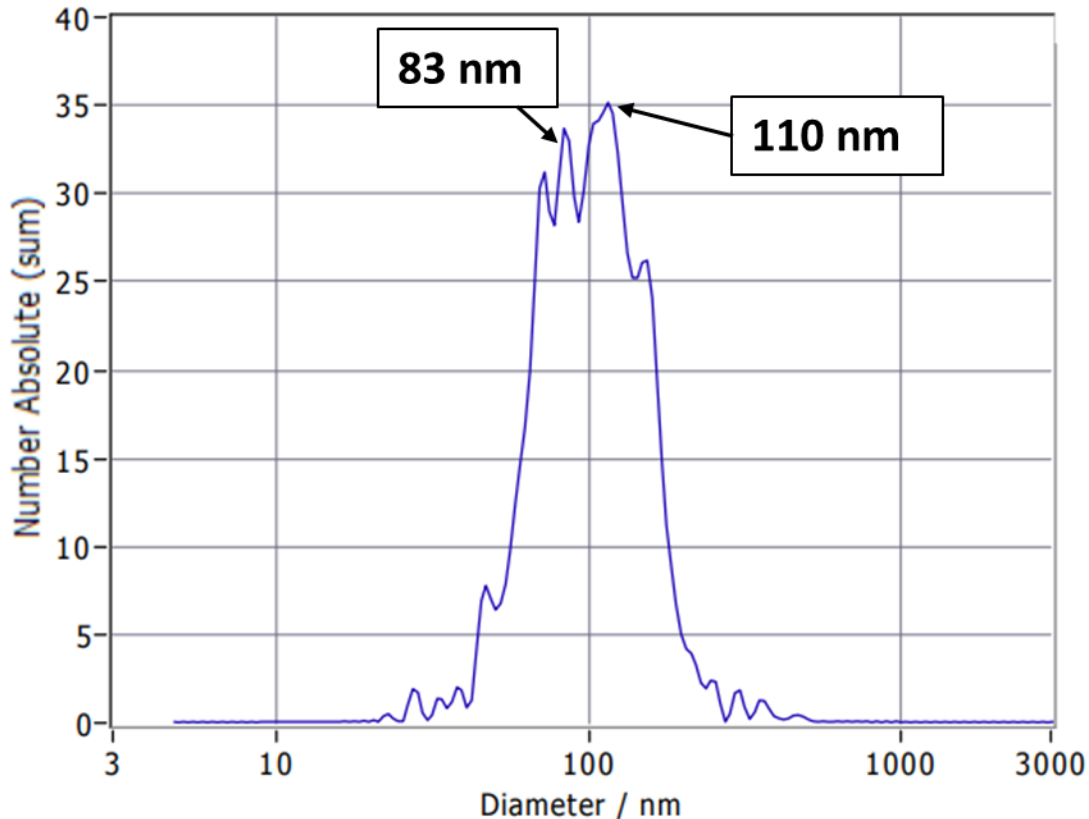


**Figure 3.1.** Size distribution of FeEVs. Nanoparticle tracking analysis of FeEVs injected IC into mice burdened with metastasis or healthy mice. FeEVs had size peaks between 80-110 nm, which is similar to the size of small EVs (50-200 nm) but larger than SPIOs alone (70 nm).

Transmission electron microscopy of FeEVs and unlabeled EVs isolated using the same centrifugation force reveal similar membrane-bound structures. The unlabeled EVs do have more of the typical cup shape seen in literature, but also possess some particles that do not appear to have that shape, instead appearing as circular particles like those seen with FeEVs, indicating a similarity. Some of the FeEVs also exhibit that cup-like shape more typically seen as well. Iron is heavily associated with EVs, but there is also a lot of free iron, unassociated with any structures, indicating that the labeling is not perfect and not all iron signal is from iron associated with EVs (Figure 3.2).

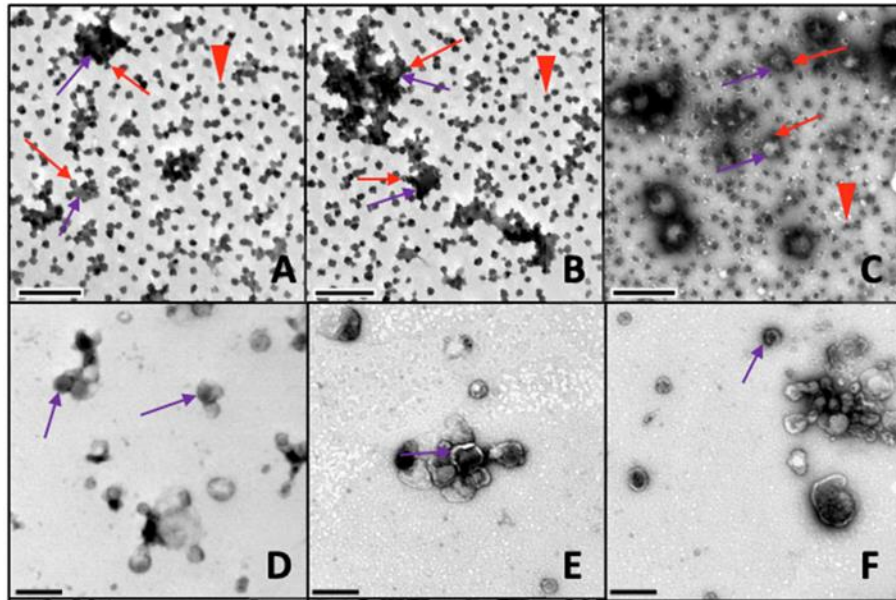


**Figure 3.2.** Visualization of 4T1-BR5 EVs. Images of EVs from 4T1-BR5 cells were captured via transmission electron microscopy (TEM) in biological triplicates with iron (Fe-EVs;A-C) and unlabelled (D-F). Red arrows indicate iron associated with EV membranes (A-C) while purple arrows show EVs  $\pm$  iron (A-F). Red triangles indicate free iron (A-C). Scale bars = 250 nm; magnification = 15,000X (A-C); magnification = 10,000X (D-F).

Western blots of FeEVs showed protein expression from Alix and TSG101, both common cytosolic EV protein markers due to their roles in the ESCRT pathway, which is involved in the process for creating multivesicular bodies, and the resulting exosomes (Figure 3.3). Expression of surface EV protein markers was more challenging to determine. Immunogold labeling of FeEVs and SPIOs as a negative control for common EV marker tetraspannin CD63 was performed and analyzed using transmission electron microscopy (Figure 3.4). There was no direct association of gold particles, which would indicate presence of CD63, with the FeEVs, the gold appears to be randomly spread throughout the images, as seen in Figure 3.4. Western blots for CD63 also showed no signal for FeEVs (Figure 3.3). Further investigation to see if the FeEVs express other membrane proteins such as CD9 or CD81, tetraspannins like CD63, typically

expressed by EVs was performed using proteomic analysis (Figure 3.6) as well as super-resolution imaging of EVs labeled with fluorescent antibodies to the three previously mentioned tetraspannins (Figure 3.5).

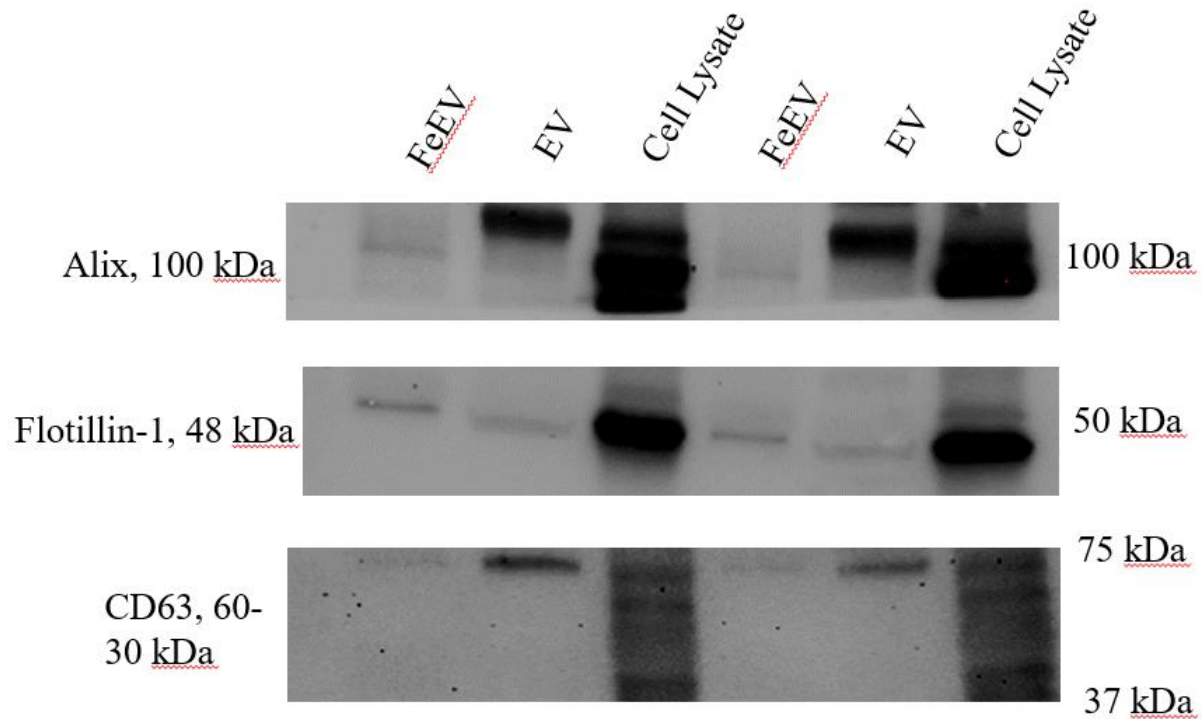


**Figure 3.3.** Protein expression of FeEVs. Western blots of FeEVs, unlabeled exosomes, and cell lysates from 4T1BR5 cells for EV cytosolic proteins Alix and Flotillin-1, and membrane protein CD63.

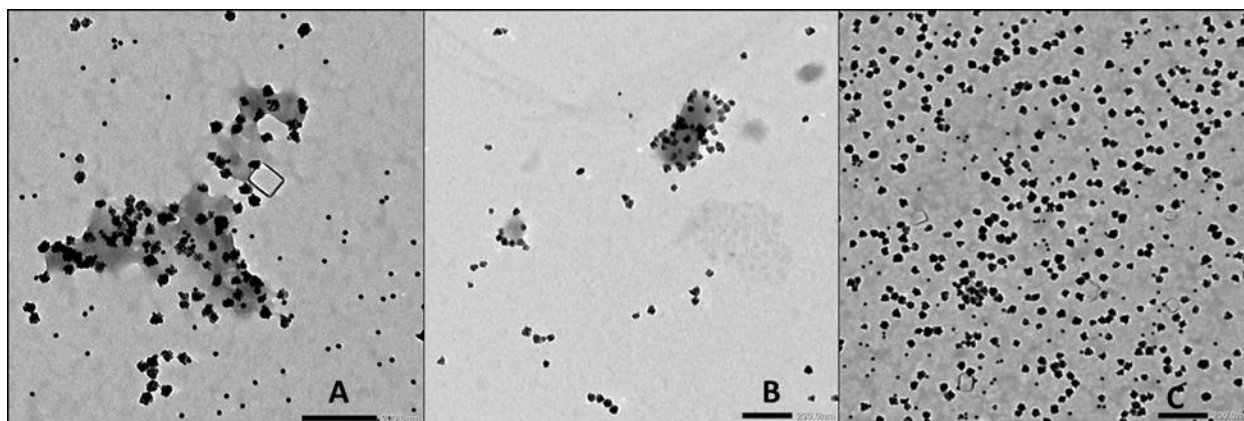


**Figure 3.4.** Immunogold labeling of FeEVs. Representative images of immunogold labeling of FeEVs using the primary and secondary antibodies (A), immunogold labeling of FeEVs using only the 2<sup>nd</sup> antibody to look for non-specific binding of the secondary antibody (B), and immunogold labeling of SPIOs using the 1<sup>st</sup> and 2<sup>nd</sup> antibodies to look for non-specific binding of the primary antibody.

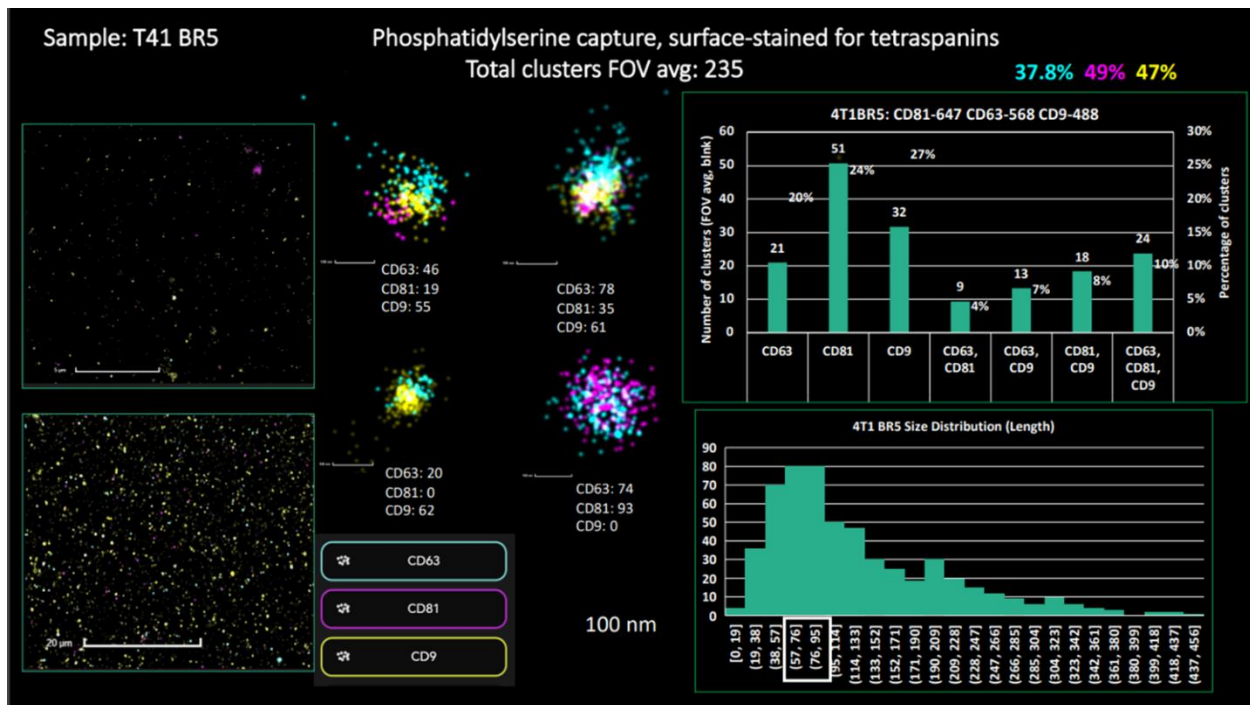


**Figure 3.5.** Super resolution microscopy of FeEVs, performed by representatives of ONI Nanoimager. 4T1BR5 FeEVs were captured by beads displaying antibodies to typical tetraspanins CD9, CD81, and CD63. Close up images of the EVs displaying those EVs can be seen, alongside population percentages for each tetraspanin marker and approximate size distributions.

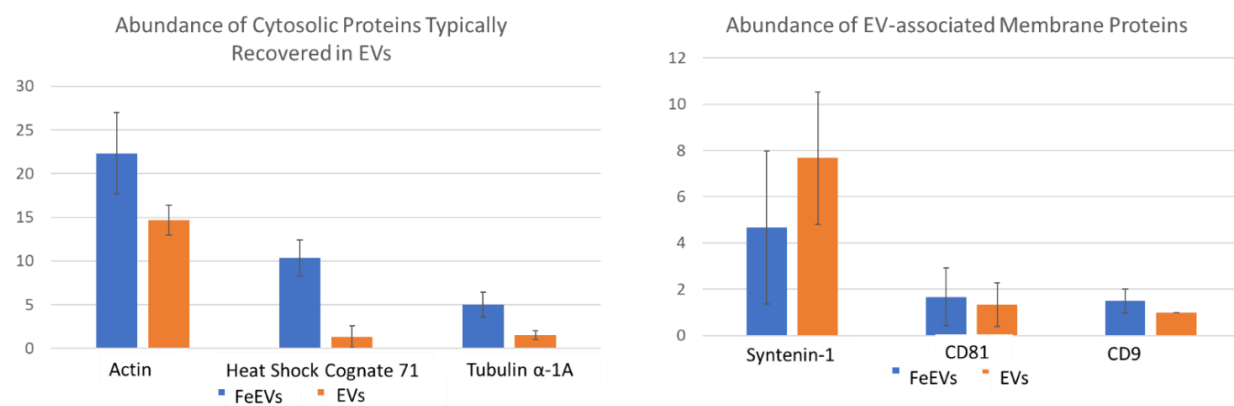


**Figure 3.6.** Abundance of cytosolic and membrane-associated EV proteins, as determined by proteomic analysis. n=3.

4T1BR5-fLuc/GFP cells were seeded on glass slides and treated with FeEVs or SPIOs (20  $\mu$ g iron) overnight before fixation. The FeEVs were stained with PKH26, a lipid membrane stain, for the EV membranes. Points of far-red fluorescence, corresponding to the fluorescent signal from the Synomag-D particles, are associated with clouds and dots of lipid stain. The fluorescent stains from the membranes and the fluorescence Synomag-D are seen in and around GFP+ 4T1BR5 cells (Figure 3.7). Fluorescence from Synomag-D is also associated with fluorescence from 4T1BR5-fLuc/GFP when SPIOs alone were added to the cells (Figure 3.7).

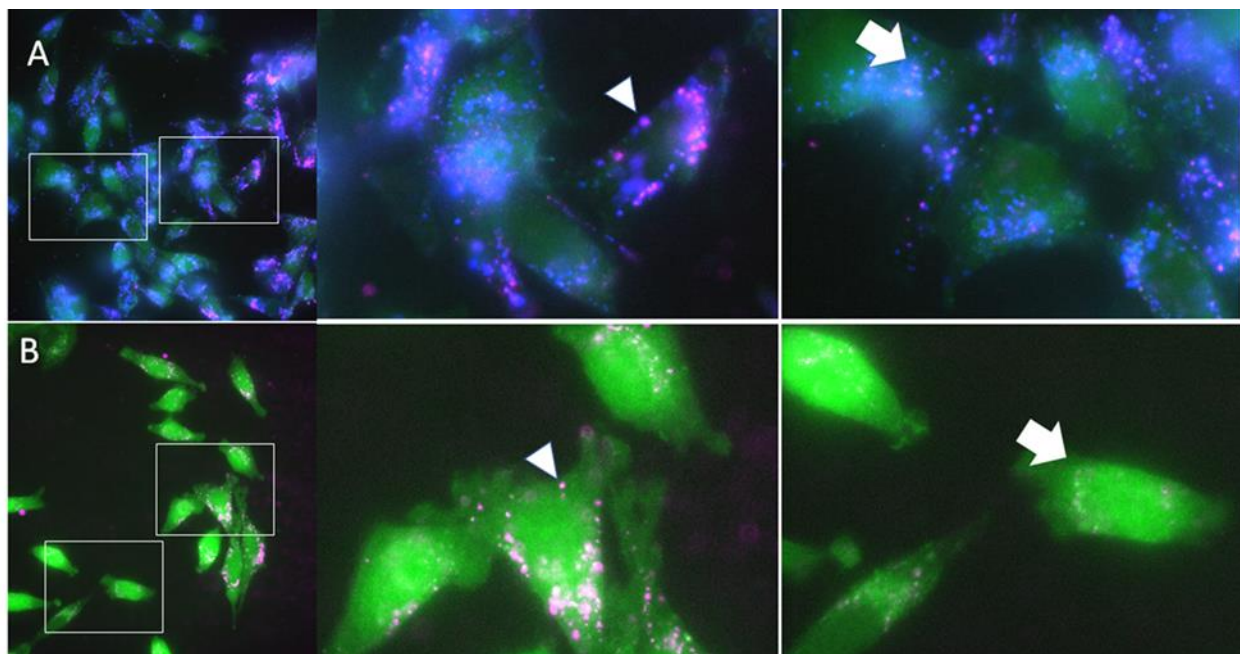


**Figure 3.7.** FeEVs and SPIOs are taken up by 4T1BR5 cells *in vitro*. 4T1BR5-fLuc/GFP cells (green) were treated with 4T1BR5-derived FeEVs (A) or SPIOs only (20 $\mu$ g, B) for 24h. FeEVs were stained with PKH26 (blue) and this membrane stain corresponds with SPIOs indicating that SPIOs are associated with a plasma membrane. Iron and EV fluorescence were always associated with cells treated with FeEVs, to varying extents (A-arrowhead, high iron and arrow, low iron). Cells treated with SPIOs only did not appear to have as many cells with iron (B-arrowhead, high iron and arrow, little to no iron).

4T1BR5-fLuc/GFP cells were injected intracardiac (i.c.) into the left ventricle of Balb/C mice using ultrasound guidance. Tumor formation was monitored by BLI using interperitoneal injections of D-luciferase every 48 hours after injection (Figure 3.8). There was high luciferase signal in the heads of each mouse, indicating successful formation of brain metastasis. BLI of the whole mouse showed signal in multiple locations throughout the body, indicating formation of multiple metastases.  $6 \times 10^6$  4T1BR5-fLuc/GFP cells/mouse were labeled with far-red fluorescent 70 nm dextran-coated Synomag-D to produce FeEVs. FeEVs (n=11), or an equivalent iron amount of SPIOs (30  $\mu$ g, n=5) was injected i.c. via ultrasound into the left ventricle of mice with brain metastases. FeEVs were also injected i.c. into healthy mice (n=5). Each mouse was scanned 1-4h post-injection in the MPI using the 2D high resolution imaging mode. The majority of the iron signal was seen in the liver, but zooming in on the heads of each mouse revealed iron signal in the heads of mice with brain metastasis injected with FeEVs. No signal was detected in the heads of healthy mice injected with FeEVs or mice with brain metastasis injected with SPIOs (Figure 3.9). The amount of iron in the head was calculated first by determining the amount of signal in the head. The average signal of the noise was calculated using the Osiris software. The Osiris software then detected all signal three standard deviations above the noise, which is assumed to be true signal. The average signal detected was multiplied by the total area of the projection and fit to a curve that compared known amounts of iron to signal detected using a high resolution imaging mode, allowing for the amount of iron to be calculated (Figure 3.10).

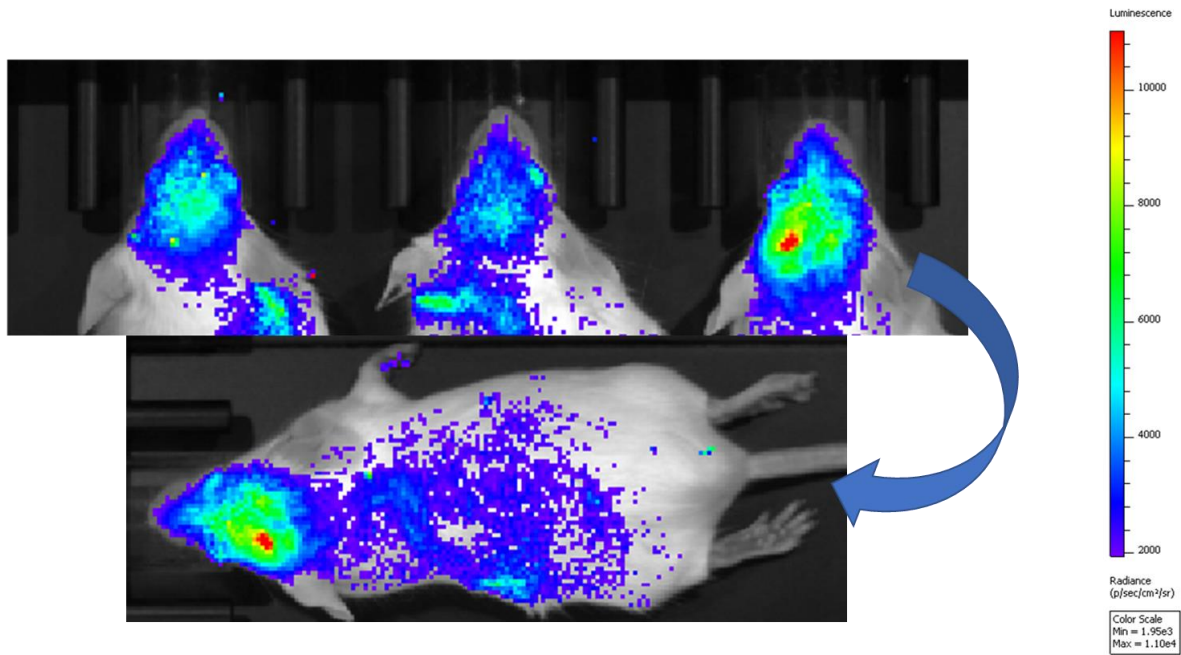


**Figure 3.8.** Bioluminescence imaging of Balb/C mice injected intracardiac via ultrasound guidance confirms successful formation of metastasis in the brains of these mice, as well as the formation of additional metastases.

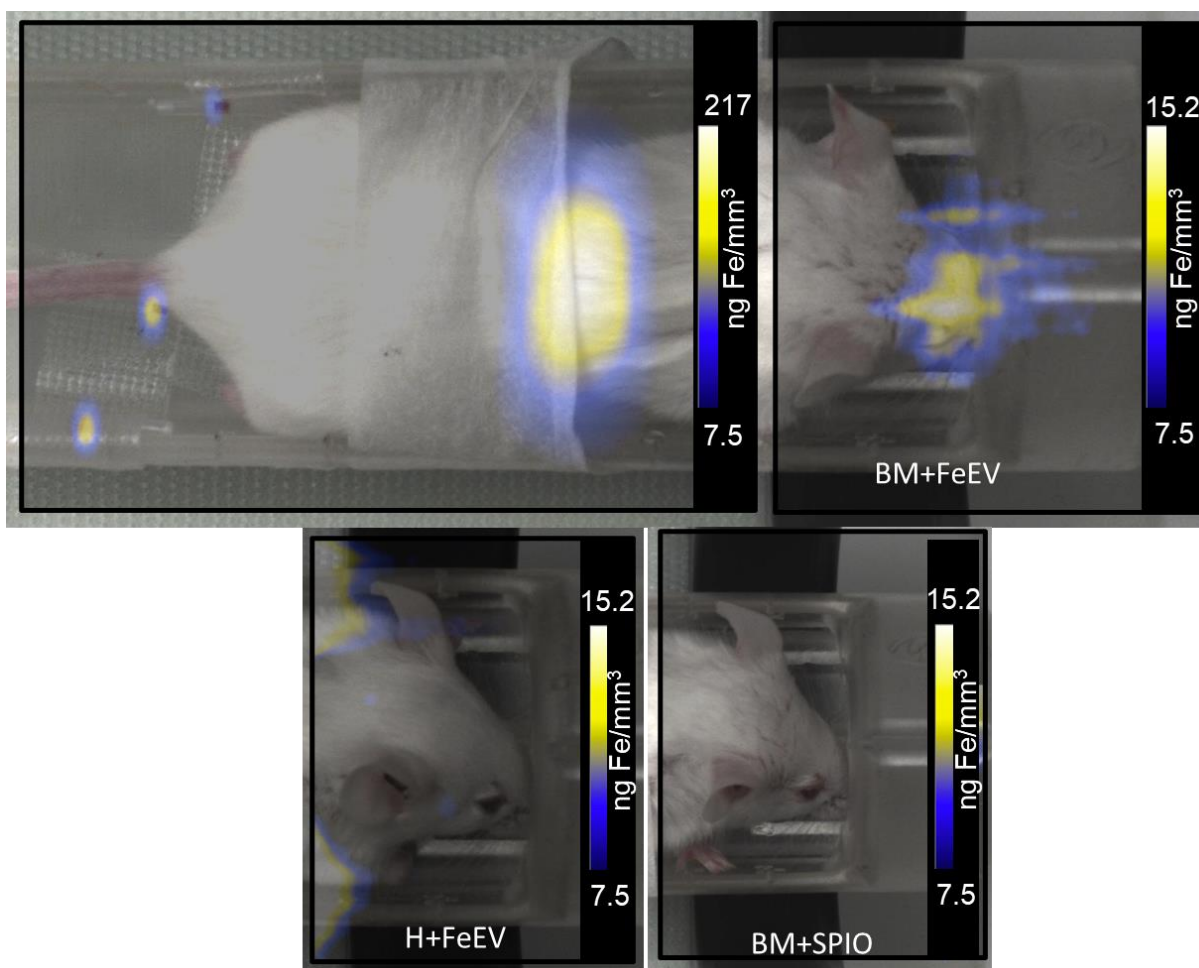


**Figure 3.9.** IC injection of SPIONs (n=5) or FeEVs (n=11), or injection of FeEVs in healthy mice (n=5) 7-8 days PI showed signal primarily in the liver whether SPIONs or FeEVs were injected 1 h post injection. Mice were sacrificed 1-4h post injection, and ex vivo scanning of their brains showed no signal (data not shown).

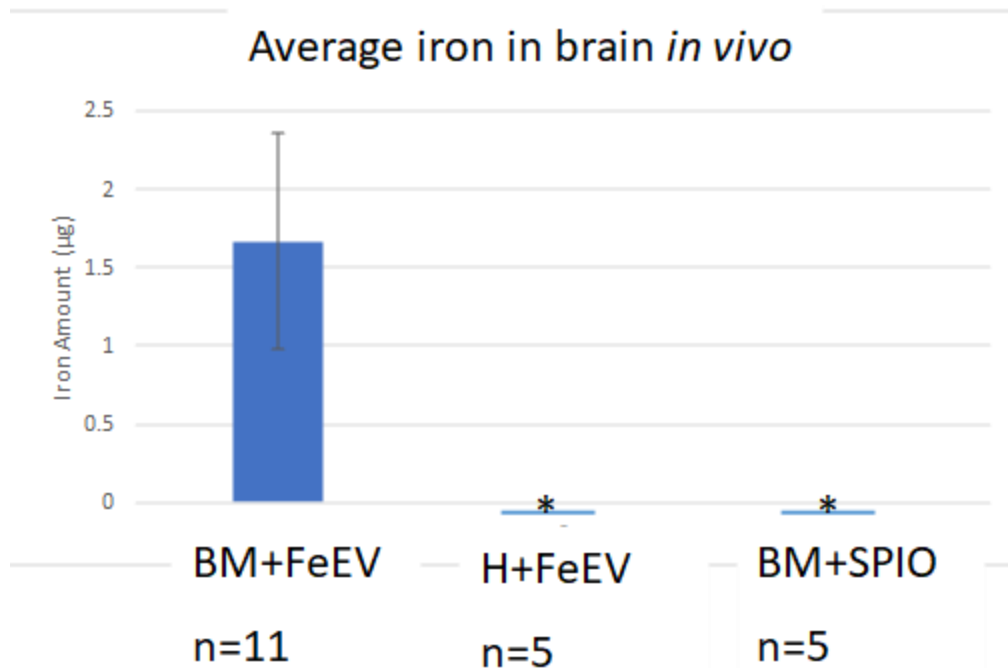


**Figure 3.10.** Iron amount (ug) in the brain of Balb/C mice when scanned after IC injection of FeEVs or SPIOs. \*signal not detected and unable to be quantified.

Immediately after imaging, each mouse was perfused with 10 U/ml heparin, followed by 4% PFA. The heads and bodies of each mouse were then soaked in 4% PFA for fixation. In order to make sure that timing of imaging did not play a significant role in uptake, this experiment was repeated using a total of eight mice, six of which had established brain metastasis using the previously described protocol. Four of these mice were injected i.c. with FeEVs, and two were injected using an equivalent amount of SPIOs (30 ug), 7-8d post-injection of cells. Two healthy mice were injected with FeEVs i.c. as well, and each mouse was imaged in the MPI using the 2D standard imaging mode 60-90 min post-injection. Iron amounts in the head were determined using the previous method described, with a curve established using known amounts of iron and 2D standard imaging being used to determine the amount of iron instead. These sets of mice were combined and reported by the percentage of injected dose to reach the brain.

One healthy mouse and one mouse with brain metastasis were injected with FeEVs that were stained with PKH26, the lipid membrane stain used in the *in vitro* uptake study. A similar iron amount of SPIOs was also injected a mouse with brain metastasis. These mice were then frozen whole in cryomount, before slicing in the Emit Xerra. GFP signal from small metastases outside the brain was identified in both mice with brain metastasis, but only the mouse injected with FeEVs had fluorescent signal from the Synomag-D particles, although the signal is very faint. There was also signal from the PKH26 lipid membrane stain present in the metastasis. No signal from the Synomag-D was seen in mice injected with SPIOs in green fluorescent tumors. No signal from the FeEVs could be identified outside of the liver in the healthy mouse (data not shown). Unfortunately the brains were destroyed by machine failure.

## **DISCUSSION**

FeEVs from 4T1BR5-fLuc/GFP cells exhibited two different median sizes, as evidenced by NTA. These sizes are 83 nm and 110 nm, both of which are within the average size range for small EVs, previously given as 30-150 nm<sup>14</sup>. There may also be a small peak around 70 nm, which the hydrodynamic size of our SPIO, but the majority of the particles are larger than that standard size, indicating once again that something other than the SPIOs were isolated by differential centrifugation. Immunogold labeling of these particles revealed that CD63, a classical EV protein, was not associated with our FeEVs. However, these TEM images showed that we have iron associated with some sort of membrane. Each of these membrane particles were associated heavily with iron, and no membrane bound particles could be identified without iron also present. However, there is quite a bit of iron not associated with any of these larger membrane bound particles, indicating that our purification method is not perfect. TEM also could not determine if the iron was bound to the exterior of the membrane or if it is present

inside the particle, so we conclude that our FeEVs are not necessarily EVs that contain iron, but EVs that are associated with iron.

As the iron nanoparticles may interfere with immunogold labeling due to iron potentially blocking the CD63 antibody on the surface or interior, we decided to confirm our lack of CD63 expression with western blotting. Western blots of the FeEVs confirmed that there is no CD63 expression, while other EV markers for cytosolic proteins, specifically Flotillin-1 and Alix, were expressed in our FeEVs. However, the super resolution microscopy showed that the FeEVs were 37.8% positive for CD63, 49% positive for CD81, and 47% positive for CD9, other tetraspannin EV markers, indicating that the previous results could be due to very low CD63 expression. Proteomic analysis confirmed expression of CD9 and CD81, while no CD63 was detected, which could again be due to the lower expression of CD63 in comparison for the other mentioned tetraspannins (Figure 3.6). Additional EV-associated proteins, both membrane-associated and cytosolic proteins, as defined by the ISEV 2018, were identified in the FeEVs as well. Additionally, several proteins implicated in EV uptake were identified, including fibronectin, histones, lactadherin, and annexins. These had a significant increase in expression by FeEVs in comparison to the unlabeled EVs, which may indicate that they may be better suited for uptake in recipient cells.

These FeEVs were taken up by 4T1BR5-fLuc/GFP cells *in vitro*. SPIOs with similar amounts of iron were also taken up by these cells *in vitro*, indicating that the brain metastatic cells are capable of taking up both FeEVs and plain SPIOs, so there are no inherent issues with using either for drug delivery to brain metastases resulting from 4T1 breast cancer cells. For testing *in vivo* delivery, 4T1BR5-fLuc/GFP cells were injected into the left ventricle of the heart of six week old BalB/C mice, confirmed by ultrasound imaging of the injection. Tumor growth

was observed by IVIS every 48 hours, showing firefly luciferase signal from the 4T1BR5-fLuc/GFP cells in the head of the mouse. Luciferase signal was also present in other locations, indicating the formation of multiple metastases.

Due to our previous results, where injecting FeEVs IV into the tail vein resulted in most of the iron being absorbed by the liver, we decided to inject the FeEVs and SPIOs intracardiac into the left ventricle of the mice 7-9 days post establishment of the metastasis as well, since blood from the left ventricle goes directly to the brain. Since any iron present in the brain could be due to the injection method, instead of any direct delivery to the brain metastasis, we also injected FeEVs intracardiac into healthy mice with no tumors or metastases. The mice were imaged with MPI one hour post injection of the FeEVs or SPIOs, before being perfused with 4% PFA to preserve the brain and other tissues. These one hour time point scans showed signal in three out of four brains of mice with brain metastasis injected with FeEVs. Interestingly, there was no signal seen in brains of mice with brain metastasis injected with SPIOs or healthy mice injected with FeEVs, suggesting that that the association of iron with EV membranes and the presence of a tumor are required for FeEVs to cross the blood brain barrier. The lack of iron detected when SPIOs are injected suggests that the blood brain barrier is at least mostly intact, preventing random small particles from passing through, though there still could be iron crossing the blood brain barrier in amounts too low for the MPI to detect any signal. There was still quite a bit of signal in the livers of the mice, which is to be expected as the FeEVs and SPIOs are technically foreign particles being cleared from the blood stream. Injecting higher amounts of FeEVs would likely result in easier to detect signal in the brain, as the amount of iron being injected is still much lower than seen in other MPI studies. Association of iron with EV

membranes and the presence of a tumor was necessary for iron to cross the blood brain barrier, and FeEVs can enter brain metastases.

Whole body sectioning of one mouse from each group was also performed in order to identify iron nanoparticles in the brain metastases or any other metastasis that formed. Unfortunately, there was an error during the whole body sectioning that resulted in the brains of the mice being destroyed instead of cleanly sliced, so there is no information from the brains of these mice. Other metastases could be identified in both of the mice injected with 4T1BR5-fLuc/GFP cells, as these cells express GFP so they could be identified with fluorescent imaging. The SPIOs were also tagged with a fluorescent marker, and the EV membranes were dyed with another fluorescent dye in order to identify any areas where all three overlap. There were two spots identified in one mouse that expressed GFP from the 4T1BR5-fLuc GFP cells, red fluorescence from the membrane dye of the FeEVs, and far-Red expression from the nanoparticles, indicating that FeEVs were present in metastatic tumors outside the brain. In the mouse with brain metastasis injected with SPIOs, other metastases could be identified by the GFP signal from the cells, but there was no accompanying far-Red signal from the SPIOs. SPIOs have been shown to be taken up by metastases in other studies, so this is likely once again due to the comparatively low amount of iron being injected compared to these other studies. However, the fact that FeEVs could still be identified in the metastases with the same amount of iron injected indicates that FeEVs are more effective at traveling to and being taken up by the metastases compared to SPIOs alone. FeEVs could not be identified in slices from healthy mice injected with FeEVs.

## **CONCLUSIONS AND FURTHER DIRECTIONS**

FeEVs are similar in size to normal EVs and express several EV related proteins, while also having an increase in proteins associated with EV uptake. The FeEVs were taken up by brain metastasis cells *in vitro*, and exhibited accumulation in the head of mice with brain metastasis. No signal was seen in the heads of mice with brain metastasis when injected with SPIOs or healthy mice injected with FeEVs. This suggests that FeEVs could be used for delivery to brain metastases from breast cancer. Further work in this area would be to load the FeEVs with a therapeutic to observe if the accumulation of these EVs is enough to make an effect on the size of the tumor. The use of tumor cell-derived EVs is a potential drawback, as these same types of EVs have been linked to promoting metastasis in other studies. Further work should observe mice for longer periods of time to see if the use of these EVs impacts the metastasis. EVs also have some larger drawbacks as a drug delivery system, including highly specialized equipment requiring training to use and a time-consuming isolation process. In order to see clinical use, assuming that the therapeutic treatment is a success, these challenges would need to be addressed.

## **MATERIALS AND METHODS**

### **Cell Culture**

4T1BR5-fLuc/GFP cells were gifted by Dr. Paula Foster at Western University. The cells were maintained in 10% FBS and RMPI+Glutamax (GIBCO, catalog# 61870036) at 37°C with 5% CO<sub>2</sub>. They were passaged using 5% Trypsin-EDTA. Cell concentration for seeding was determined using a Trypan-Blue Live/Dead stain.

## **Iron Labeling**

Cells were treated with a combination of Synomag-D, heparin, and protamine sulfate to label them with iron. Protamine sulfate mixed with 2.5 ml of FBS-free media per dish was added to heparin and fluorescently-labeled Synomag-D (1 mg/ml) in 2.5 ml of FBS free media per dish. 5 ml of this mixture was added to each dish and allowed to incubate for 3-6 hours before 5 ml of complete media was added. The cells were then incubated for 24 hours post-addition of iron.

## **FeEV Isolation**

Iron-labeled cells were washed three times with 10 U/ml heparin in PBS, and once with PBS. 10% EV-depleted FBS was added to RPMI+Glutamax, which was then added to the cells. The cells were then allowed to produce EVs for 24 hours, before the media was removed to perform differential centrifugation. Cells were spun out at 600g for 10 minutes, and apoptotic bodies were spun out at 2,000g for 20 minutes. FeEVs were concentrated at 20,000g for 1 hr, and were either further concentrated at 20,000g for 1 hr before resuspension in PBS, or resuspended in PBS immediately.

## **EV Isolation**

Cells were seeded at 3E6 cells/10 cm<sup>2</sup> dish. 48 hr post seeding, cells were washed twice with PBS before 10% EV-depleted FBS in RPMI+Glutamax was added. The cells were incubated with the EV-depleted media for 24 hours, before the media was removed for EV isolation. The media was spun at 600g for 10 minutes to remove cells and 2,000g for 20 minutes to remove apoptotic bodies. The remaining media was then pelleted at 20,000g for 1 hr or added to ExoQuick and incubated overnight before pelleting the EVs at 1,500g for 30 minutes, following manufacturer's instructions. Pelleted media had the supernatant removed, and that

supernatant was further concentrated at 100,000g for 1.5h before resuspension in PBS for proteomic analysis.

### **Cell Lysate**

Iron-labeled cells were incubated with 2.5 mM EDTA in PBS for 5-10 minutes, and then centrifuged at 2,000g for 5 minutes. They were washed with PBS and centrifuged again at 2,000g for 5 minutes, before resuspension in lysis buffer. The lysis buffer consists of protease inhibitor (ThermoFisher, A32955) and phosphatase inhibitor (ThermoFisher, A32957) in modified mRIPA buffer (0-0.1% SDS). The cell pellet and lysis buffer was shook at 4°C for 30 minutes, before being frozen at -80°C. After thawing, the mixture was centrifuged at 16,000g for 20 minutes to remove cell debris, and the supernatant was collected.

### **Western Blotting**

Protein concentration of 4T1BR5-fLuc/GFP cell lysate, FeEVs, and EVs isolated using ExoQuick was determined using the Pierce BSA Protein Assay kit (ThermoFisher, 23225). The protein quantification curve was completed in replicate 3 times, and the unknowns were all replicated twice.

15 ug of protein was added per well, mixed with DI H<sub>2</sub>O and RunBlue LDS sample buffer (4X) (Expedeon, NXB31010). The cell lysate mixtures were heated at 70°C for 10 minutes, while the FeEVs and EVs were not heated to avoid aggregation. The proteins were separated using Mini-PROTEAN TGX Stain-Free Pre-cast gels (BioRad, 4568093) at 100 V for 80-90 minutes in the BioRad Mini-Protean Tetra system. The ladder used was the Precision Plus Protein All Blue Standard (BioRad, 1610373). The protein was transferred to a nitrocellulose membrane using the BioRad Trans-Blot Turbo Transfer System, running at 25V for 30 minutes.

The membrane was then blocked using 5% w/v non-fat dry milk in TBST for one hour at room temperature or overnight at 4°C. The primary antibody was added to the membrane and shook at 4°C overnight. The membrane was then washed three times using TBST, and the secondary antibody was added to the membrane, which was then shook at room temperature for one hour. The membrane was washed again three times with TBST, before the Pierce ECL Western Blotting Substrate kit (ThermoFisher, 32209) was added. The proteins and ladder were then imaged using the ChemiDoc MP imaging system (Bio-Rad Laboratories, Inc.) using the autoexposure and chemiluminescence to observe the bands and 635 nm of light with autoexposure for visualization of the ladder.

### **Immunogold Labeling**

FeEVs or equal amounts of iron in 16% PFA were incubated with carbon-coated TEM grids for a minimum of one minute. They were then blocked in 5% BSA and 1% (insert) serum for one hour at room temperature. The grids were then transferred to a 25 ul droplet of CD63 antibody in 1% BSA in PBS and allowed to sit overnight at 4°C. The grids were washed three times in 1% BSA in PBS, before being added to a 25 ul droplet of 12 nm gold-conjugated insert anti-rabbit in 1% BSA in PBS for 2 hours. The grids were washed again in 1% BSA in PBS three times, before being incubated in 2.5% glutaraldehyde in 0.1M phosphate buffer for 15 minutes at room temperature. The grids were then rinsed with PBS and EM-grade DI H<sub>2</sub>O, and dried.

### **EV Physical Characterization**

FeEVs in PBS or equal amounts of iron in PBS were added to the Nanoparticle Tracking Analysis machine. An average of 50-150 particles was read per frame as quality control. The analysis parameters used were: Max Area:1000, Min Area: 10, Min Brightness 22, with 11frames read twice per sample.

FeEVs were fixed in 16% PFA. They were allowed to adsorb on carbon-coated formvar copper grids for 20 min, before incubating in 2.5% glutaraldehyde in 0.1M phosphate buffer for 15 minutes at room temperature. The grids were washed with PBS and EM-grad DI H<sub>2</sub>O before imaging with transmission electron microscopy (TEM; JEM-1400Flash, JEOL, MA USA), using the JEOL 1400-Flash Transmission Electron Microscope (Japan Electron Optics Laboratory, Japan).

### ***In Vitro* Uptake**

FeEVs were isolated from 4T1BR5-fLuc/GFP cells and stained with PKH26. FeEVs or equal amounts of iron of fluorescent Synomag-D was added to (number) of 4T1BR5-fLuc/GFP cells seeded on a (well number) glass slide. The FeEVs or SPIOs were incubated with the cells for 24 hours, before being washed with PBS and fixed using 4% PFA. Fluoromount mounting media was added with a coverslip and allowed to dry overnight before imaging. Fluorescence imaging was performed using the Leica Thunder. Overlays of fluorescence images were made using Image J.

### **Metastasis Establishment**

6 week old Balb/C mice (Charles River Laboratory), obtained and cared for using the guideline set by the Michigan State University Institutional Animal Care and Use Committee, were injected with  $2 \times 10^5$  in 85  $\mu$ l PBS mixed with 15  $\mu$ l microbubbles. The mice underwent anesthesia with 2% isoflurane in oxygen before removing their stomach hair with Nair and injection with ketoprofen into the scruff as an analgesic. The mice were then strapped down on their backs and the left ventricle of the heart was located using ultrasound. The needle entering the left ventricle of the heart and subsequent injection of the cells and microbubbles were imaged

via ultrasound for confirmation of successful injections. The mice were monitored until they woke up for signs of pain or distress.

### **FeEV and SPIOs Injections**

7-8 days post-establishment of metastasis, 85-150  $\mu$ l of FeEVs or equal amounts of iron of SPIOs were injected intracardiac. The mice went under 5% CO<sub>2</sub> as anaesthesia and injected with ketoprofen into the scruff for any pain. Ultrasound was using to located the left ventricle of the heart from the anterior of the mouse. Ultrasound was used again to image the needle entering the heart and the subsequent injection of the FeEVs or SPIOs. The mice were taken for additional imaging post-injection and monitored until they woke up.

### ***In Vivo* Bioluminescence Imaging**

100  $\mu$ l of d-Luciferase (30 mg/ml) was injected IP into awake mice. The mice were anesthetized 12 minutes later, and the unconscious mice were imaged via the IVIS Spectrum at 15 minutes post-injection. The mice were feed a continuous feed of 2% isoflurane in oxygen via the nose for anesthesia. Mice were imaged for bioluminescence signal every 48 hours, and again before magnetic particle imaging.

### **Magnetic Particle Imaging**

For the *in vivo* studies, mice were kept unconscious from IVIS imaging and added directly to the MPI animal imaging bed. The mice were imaged with the standard and the high signal 3D and 2D imaging modalities with the MPI software one hour post injection of FeEVs or SPIOs. The mice were then taken for perfusion and fixation.

### **Perfusion and Fixation**

Mice were kept under high levels of anesthesia until no signs of life were detected. A gravity-based perfusion system was inserted into the heart via a needle, washing the veins with

10 U/ml heparin before the addition of 4% PFA. The heads and livers of the mice were then removed and placed in 4% PFA for three days at 4°C, before removing the PFA and adding PBS for long term storage at 4°C.

### **Micro-CT**

Mice were transferred to the micro-CT bed when unconscious and taped down. Briefly, the whole body scan was applied, taking three separate 3D scans before being stitched together. Immediately after the scan, the mice were removed and either sacrificed or placed back in their cage and monitored until waking.

### **Image Analysis**

MPI quantification was performed using the free and open-source Horos imaging software. Calibration curves were created for both the 2D high resolution and standard imaging modes, using a fixed amount of iron. Signal for each iron amount was determined by taking 3 times the mean of the background signal for each image and using Horos to automatically detect all signal in an area above that threshold to create the ROI. The known amounts of iron were plotted against the average signal\*area of each ROI, and the formula for iron content was created by plotting a trendline ( $y=mx+b$ ). For iron detection of pellets or *in vivo*, the mean of the background signal was determined and multiplied by three to set the threshold. The Horos software was then used to create an ROI using all signal above that threshold in an area. For the scans of the mice, the MPI images were lined up with photos taken by the system to determine if signal was in the head.

## **Proteomics Analysis**

Proteomics analysis was performed by the MSU Proteomics Core using biological triplicate samples. Resulting proteins had a literature search performed to determine the function of each protein and its relevance to the study.

## REFERENCES

1. OJ Scully, B. B. G. Y. Y. Y. Breast cancer metastasis. *Cancer Genomics Proteomics*. **9**, 311–320 (2012).
2. Mills, M. N. *et al.* Management of brain metastases in breast cancer: a review of current practices and emerging treatments. **180**, 279–300 (2020).
3. Nam, B.-H. *et al.* Open Access Breast cancer subtypes and survival in patients with brain metastases. (2008) doi:10.1186/bcr1870.
4. Leone, J. P. *et al.* Prognostic factors and survival according to tumour subtype in women presenting with breast cancer brain metastases at initial diagnosis. *Eur J Cancer* **74**, 17–25 (2017).
5. Bailleux, C., Eberst, L. & Bachelot, T. Treatment strategies for breast cancer brain metastases. *British Journal of Cancer* 2020 124:1 **124**, 142–155 (2020).
6. Leone, J. P. & Leone, B. A. Breast cancer brain metastases: the last frontier. *Exp Hematol Oncol* **4**, 33 (2015).
7. Steeg, P. S. The blood–tumour barrier in cancer biology and therapy. *Nature Reviews Clinical Oncology* 2021 18:11 **18**, 696–714 (2021).
8. Xie, X. *et al.* Tumor-derived exosomes can specifically prevent cancer metastatic organotropism. *Journal of Controlled Release* **331**, 404–415 (2021).
9. Zhao, L. *et al.* Exosome-mediated siRNA delivery to suppress postoperative breast cancer metastasis. *Journal of Controlled Release* **318**, 1–15 (2020).
10. Gutova, M. *et al.* Magnetic Resonance Imaging Tracking of Ferumoxytol-Labeled Human Neural Stem Cells: Studies Leading to Clinical Use. *Stem Cells Transl Med* **2**, 766 (2013).
11. Jung, K. O., Jo, H., Yu, J. H., Gambhir, S. S. & Pratz, G. Development and MPI tracking of novel hypoxia-targeted theranostic exosomes. *Biomaterials* **177**, 139–148 (2018).
12. Bulte, J. W. M. Superparamagnetic iron oxides as MPI tracers: A primer and review of early applications. *Advanced Drug Delivery Reviews* Preprint at <https://doi.org/10.1016/j.addr.2018.12.007> (2019).
13. Sehl, O. C. *et al.* MPI region of interest (ROI) analysis and quantification of iron in different volumes. doi:10.1101/2022.04.10.487778.
14. Doyle, L. M. & Wang, M. Z. Overview of Extracellular Vesicles, Their Origin, Composition, Purpose, and Methods for Exosome Isolation and Analysis. *Cells* **8**, (2019).

CHAPTER FOUR:  
EVS DERIVED FROM MACROPHAGES IN A SCAFFOLD CAN DELIVER REPORTER  
DNA TO INJURED CARDIAC CELLS

## **ABSTRACT**

One of the leading causes of death in adults in the United States is myocardial infarction (MI), as it can lead to heart failure as cells die when no longer receiving oxygen. Macrophages have been shown to have a biphasic recruitment to the heart in the aftermath of MI, both for clearing damaged tissue (M1 phenotype macrophages) and recruitment of factors for scar formation (M2 phenotype macrophages). Treatments for MI include replacing the damaged pieces of heart with donor heart tissue, which is invasive and limited, and gene therapy using viral delivery systems such as adeno-associated vectors, which have a low transfection efficiency in clinical trials. For this reason, as well as natural biocompatibility and possible natural targeting abilities, EVs are being explored as a gene delivery system in MI. Specifically, this work investigates macrophage/monocyte-derived EVs (mmEV) as a gene delivery tool to the damaged heart tissue in MI, as mmEVs have been shown to target areas of inflammation.

Human monocyte-like (THP-1) cells were transfected with firefly luciferase, and mmEVs were collected from these donor cells. The EVs were then concentrated and used to treat human epithelial kidney cells (HEK293) and human cardiac organoids, in suspension or in Matrigel. All the recipient cells, HEK293 and cardiac organoids, expressed firefly luciferase, as determined by bioluminescence. The cardiac organoids seeded on Matrigel had higher overall light production compared to the organoids in suspension. Transfection efficiency studies were performed on the THP-1 cells in an attempt to maximize efficiency. Interestingly, treating the HEK293 cells with EVs isolated from THP-1 cells with lower transfection efficiency resulted in the recipient cells having higher transfection efficiency.

Further studies in this area would include determining if there is a difference in delivery efficiency by M2 macrophage-derived EVs, as M2 macrophages are anti-inflammatory, when the

recipient cardiac organoids are under low oxygen conditions, mimicking MI. Ideally, the reporter DNA would be switched to a therapeutic DNA as well, to measure a difference in outcome of the organoids post-injury.

## INTRODUCTION

Myocardial infarction (MI), resulting in heart failure, is one of the leading causes of death in the United States for adults<sup>1</sup>. MI results in damage to the heart due to lack of oxygen to cells, causing these cells to die. Normally, in an injury such as this, the organ would end up healing due to organ regeneration, but unfortunately the adult heart is not capable of regeneration<sup>1,2</sup>. Instead, post-MI there is a bi-phasic recruitment of M1 inflammatory macrophages and M2 anti-inflammatory macrophages for clearance of the dead and damaged tissue, followed by recruitment of factors for scar formation<sup>3</sup>. Heart failure and death can still result after this scar formation, as the scar may be too large for proper heart function<sup>1,2</sup>.

There are some treatments available for MI, such as transplanting the damaged pieces with donor heart tissue<sup>1,2</sup>. There is a limited number of donor hearts available, and there is always the possibility of immune rejection, coupled with the need for invasive surgery<sup>1,2</sup>. Unfortunately, this solution is costly, restrictive, and complicated, highlighting the need for treatments that are not based on surgery or on a need for donor tissue<sup>1</sup>. One of the areas being investigated for treatment of MI is gene therapy to improve cardiac healing, using adeno-associated viral vectors (AAV). AAV vectors have been utilized in clinical trials, but many of these trials have been unsuccessful, possibly due to immune response and non-optimized tissue targeting, causing a low transfection efficiency compared to the promise seen *in vitro*<sup>4,5</sup>. Non-viral delivery systems are now being investigated due to their low immunogenicity, despite seeing lower transfection efficiency.<sup>4-6</sup>

As discussed, EVs are a non-viral delivery system believed to have little to no immunogenicity, the ability to deliver drugs and genes *in vivo*, natural biocompatibility, and the potential to naturally target different diseases based on the cell of origin<sup>7-9</sup>. As discussed,

macrophages and monocytes are specifically recruited to the heart post-MI, and other areas of inflammation. Macrophage/monocyte EVs have also been shown to deliver therapeutics to areas of inflammation<sup>10-14</sup>, but have not been investigated for use as a therapeutic delivery vehicle for the heart post-MI. This is a potential missed opportunity, as macrophage/monocytes also contribute to healing post-MI, and macrophage/monocyte EVs (mmEVs) also contribute to this process.

Other EVs, specifically those from stem cells such as embryonic stem cells and mesenchymal stem cells, as well as EVs derived from cardiosphere-derived cells and cardiac progenitor cells, have been used to treat the heart in cases of myocardial infarction as they have an immunomodulatory effect. These effects are summarized into two categories: reduced macrophage infiltration and modulation of macrophage polarization<sup>15</sup>. Proteins and miRNA inherent to these cells' EVs are believed to be responsible for the reduced macrophage infiltration through a few different mechanisms, including downregulating expression of C-C chemokine receptor 2 in macrophages, decreasing pro-inflammatory cytokine and chemokine secretion, and decreasing the amount of macrophages that become pro-inflammatory<sup>15</sup>. Stem cell EVs push macrophages towards M2, the anti-inflammatory phenotype, while the EVs derived from cardiosphere-derived cells and cardiac progenitor cells did not push towards the M2 phenotype. They also did not push towards the pro-inflammatory phenotype, but promote phagocytosis and efferocytosis. Meta-analysis of studies treating MI using stem cell-derived EVs found that there was a reduction of infarct size<sup>16</sup>.

Several roles have been discovered for mmEVs during cardiac disease and injury<sup>17</sup>. For myocardial infarction, pro-inflammatory macrophage EVs were found to contain and deliver microRNA miR-155, which reduced the proliferation and induced inflammation in recipient

cardiac fibroblasts<sup>18</sup>. This indicates a pro-inflammatory role for inflammatory macrophage-derived EVs during cardiac injury. This is confirmed by another study by Zhang et al., M1 macrophage-derived EVs worsened oxidative stress in H<sub>2</sub>O<sub>2</sub>-treated cardiac cells H9c2<sup>19</sup>. Interestingly, this study also looked at the effects of M2 macrophage-derived EVs, and these EVs reduced the oxidative stress injury in the H<sub>2</sub>O<sub>2</sub>-treated H9c2 cells<sup>19</sup>. This would indicate that EVs-derived from M2 macrophages might also provide a therapeutic benefit, alongside an exogenous drug or nucleic acid.

This study focused on mmEVs as a gene delivery tool to cardiac organoids. Recipient test cells or cardiac organoids are treated with EVs from transfected monocyte-like cells. Delivery is determined by the recipient cell's expression of the transferred cargo, in this case firefly luciferase. Successful transfer would indicate that mmEVs can be used as a therapeutic delivery tool to cardiac organoids.

## **RESULTS**

Human monocyte-like THP-1 cells were seeded at 8E5 cells/well in a six well dish immediately prior to transfection with CAG/Luc2-TdT using Transit Jurkat. 24 hours post transfection, the cells were imaged to confirm BLI expression (Figure 4.1) before being washed with PBS twice before being seeded with EV-depleted media.

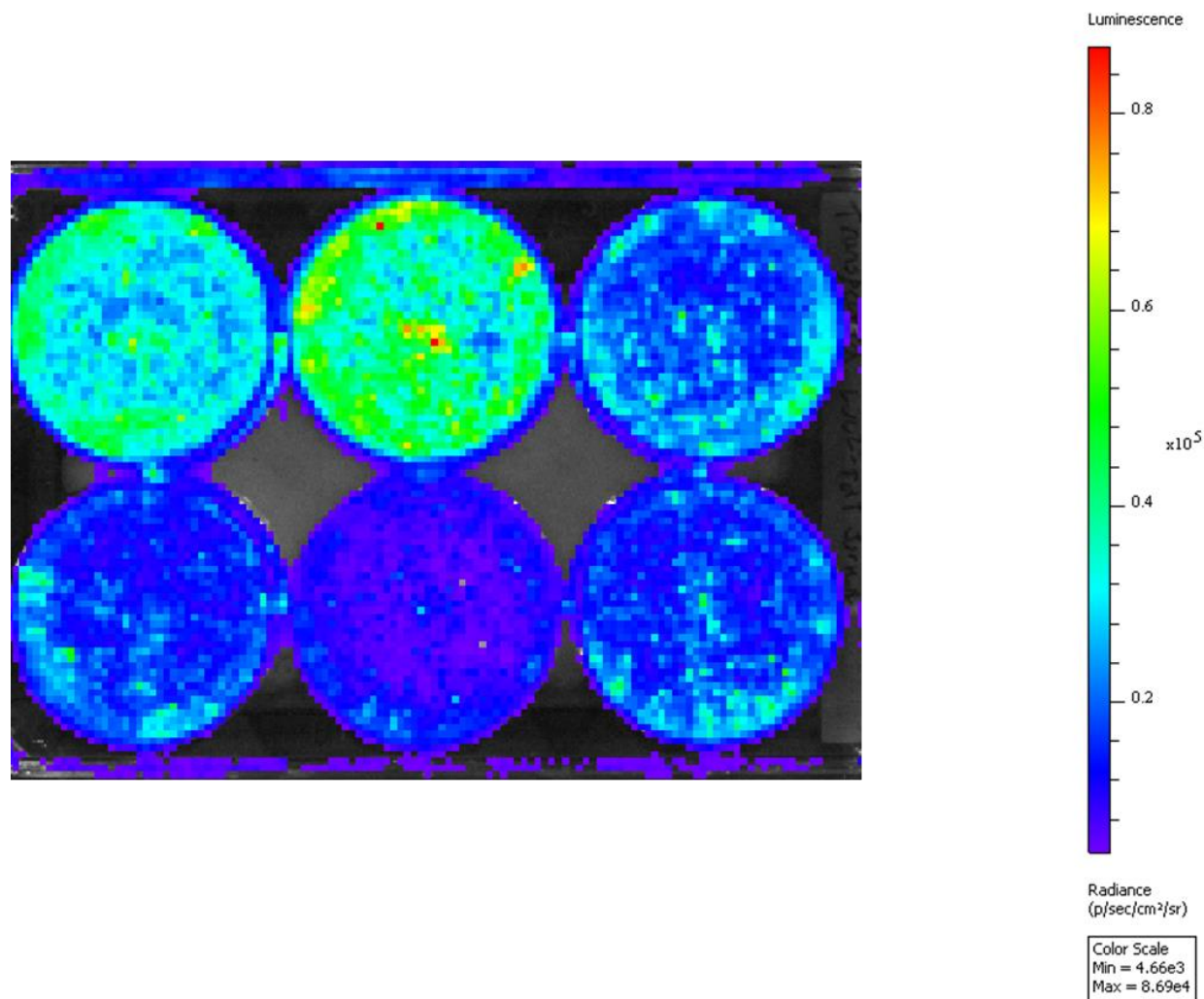


**Figure 4.1.** THP-1 cells, seeded at  $8E5$  immediately before transfected with Cag/Luc2-Tdt using TransIT Jurkat at a ratio of 1:3 DNA ( $\mu\text{g}$ ) to transfection reagent ( $\mu\text{l}$ ) in OptiMEM. BLI measured 22 hours post-transfection using the IVIS.

The media now containing EVs underwent differential ultracentrifugation, resulting in the EVs being pelleted at 20,000 g for one hour. As a positive control, EVs from one well of THP-1 cells were added to one well of  $2E4$  HEK293 cells in a 96 well dish. BLI of the HEK293 cells was measured 48 hours after EV addition using the IVIS (Figure 4.2).

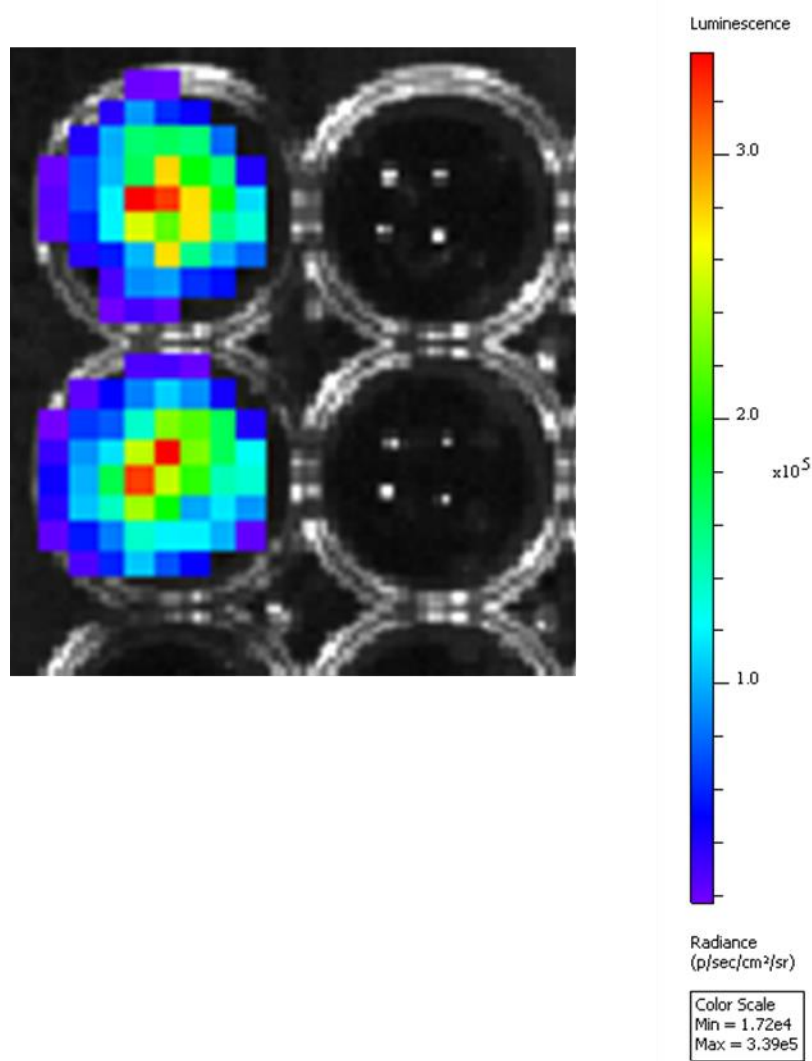


**Figure 4.2.** HEK293 cells, seeded at  $2 \times 10^4$  cells/well. The two wells on the left each had EVs from the transfected THP-1 cells added, while the ones on the right has no EVs added. BLI was measured 48h post-EV treatment.

Next, cardiac organoids were procured from Dr. Aitor Aguirre’s group, with two organoids seeded on Matrigel and two cardiac organoids suspended in media. The organoids were confirmed to beat under microscopy. EVs from one well of THP-1 cells were added per organoid, and BLI was measured 48 hours later (Figure 4.3).

### Cardiac EBs seeded on Matrigel

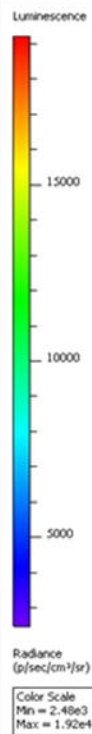
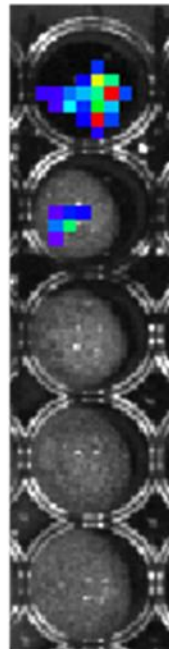
THP-EVs added

THP-EVs added

NC

NC,  
No

NC



### Cardiac EBs in suspension

THP-EVs added

THP-EVs added

NC

NC

NC,  
No

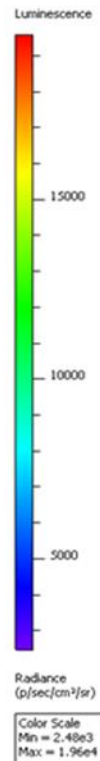
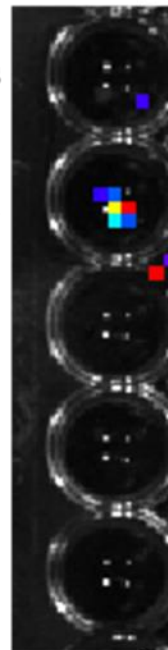


**Figure 4.3.** Cardiac organoids (EBs) seeded on Matrigel (Left) or in suspension (Right). The top two wells in each had THP-1 EVs added. Negative controls (NC) are wells with cardiac organoids with no THP-1 EVs added, and the other negative control is wells with only media (NC, No EB). BLI was measured 48h post addition of EVs.

Transfection using TransIT Jurkat was studied using different ratios of DNA to transfection reagent; 1:2, 1:3, 1:4, and 1:5  $\mu\text{g}$  of DNA per  $\mu\text{l}$  of transfection reagent. THP-1 cells were seeded either 24 hours before transfection at  $4 \times 10^5$  cells per well or immediately before transfection at  $4.5 \times 10^5$  cells per well, and bioluminescence was measured 24 hours later. Using a 1:3 ratio of DNA to transfection reagent resulted in the best transfection efficiency for the THP-1 cells in both conditions, though there was no statistical significance between 1:3 and 1:4 ratios of DNA to transfection reagent when seeded 24h before transfection (Figure 4.4). Transfection of

cells immediately after seeding was better than transfection of cells that had been allowed to sit over 24h.

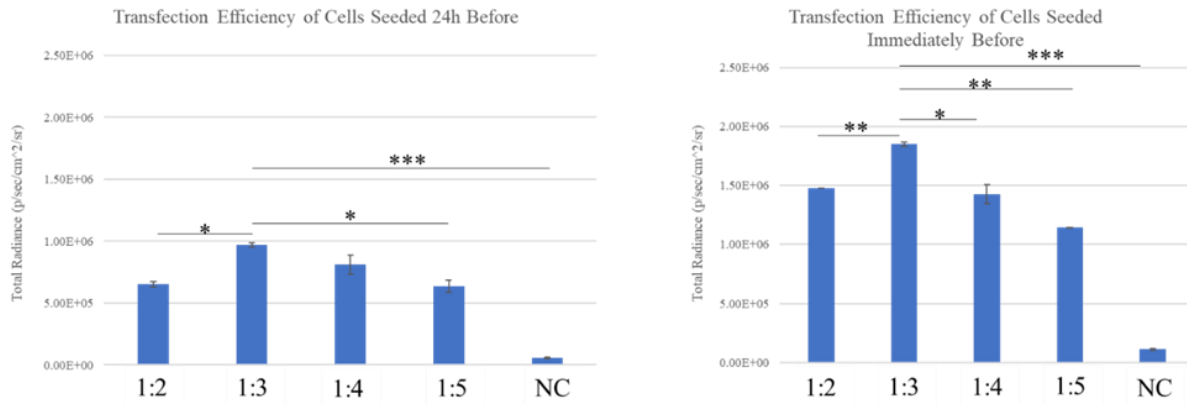


**Figure 4.4.** Total radiance of THP-1 cells seeded 24h before transfection (left) and THP-1 cells seeded immediately before transfection (right). Cells were transfected using Cag/Luc2-Tdt and Transit Jurkat, in amounts ranging from 1:2-1:5  $\mu\text{g}/\mu\text{l}$ . NC denotes negative control, wells of THP-1s that were not transfected. \* $p < 0.05$ , \*\* $p < 0.005$ , \*\*\* $p < 0.0005$ ,  $n = 2$  for each condition.

Next, transfection of THP-1 cells was explored to optimize DNA transfer. Transit Jurkat, Transit 2020, and Transit X2 were each used to transfect two wells of THP-1 cells at  $6E5$  cells/well, using 2.5:7.5 DNA to reagent ratios (Figure 4.5). 24 hours post transfection, all cells had similar amounts of bioluminescence, as measured by the Living Image software. All cells were kept separately and washed twice with PBS before EV depleted media was added. EVs were isolated from that media 24 hours later, and 20  $\mu\text{l}$  of EVs were added to each well of HEK293 cells seeded at  $2E4$  cells/well in a 96 well dish. BLI was measured 48 hours later. Only HEK293 cells treated with EVs isolated from THP-1 cells transfected with Transit X2 displayed bioluminescence (Figure 4.6).

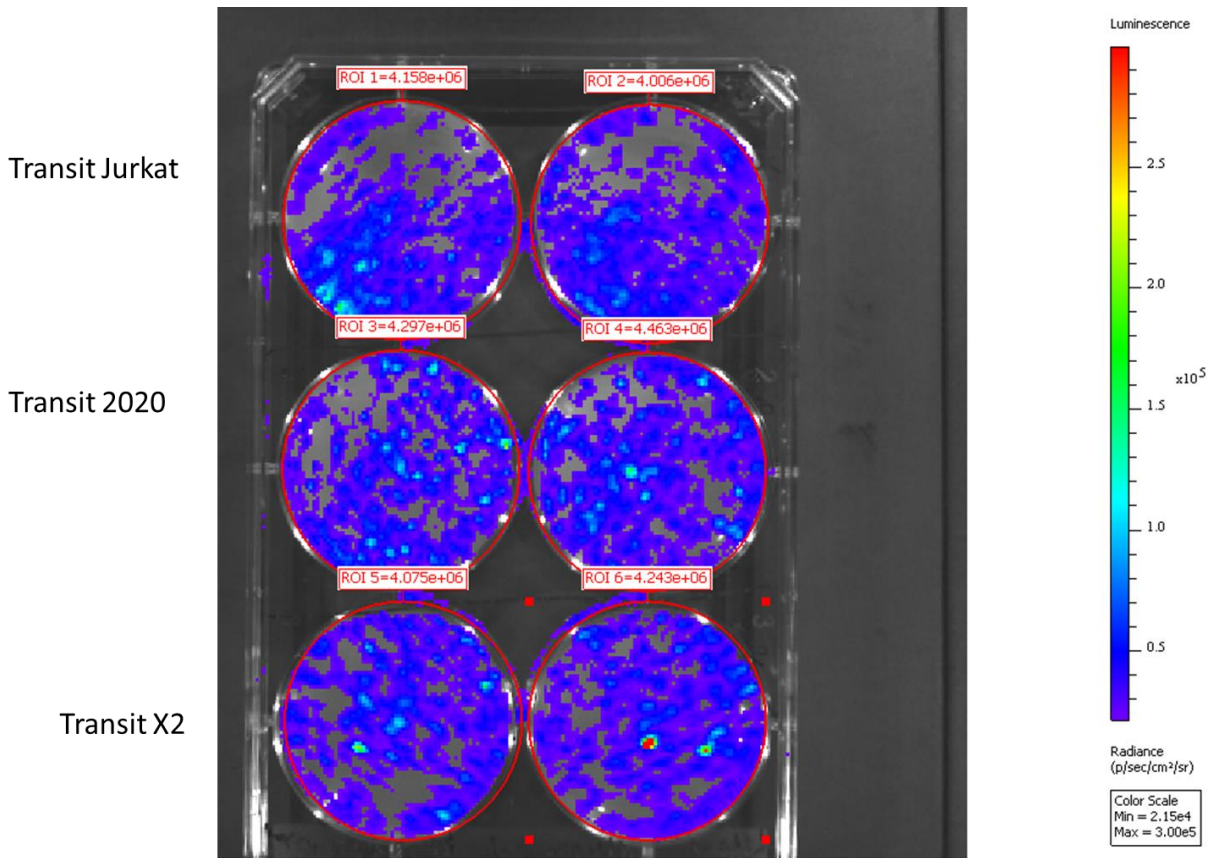


**Figure 4.5.** THP-1 cells seeded at  $6E5$  cells/well immediately before transfection. All wells transfected using  $2.5 \mu\text{g}$  of Cag/Luc2-Tdt and  $7.5 \mu\text{l}$  of reagent. Photo taken 24 hours post transfection.

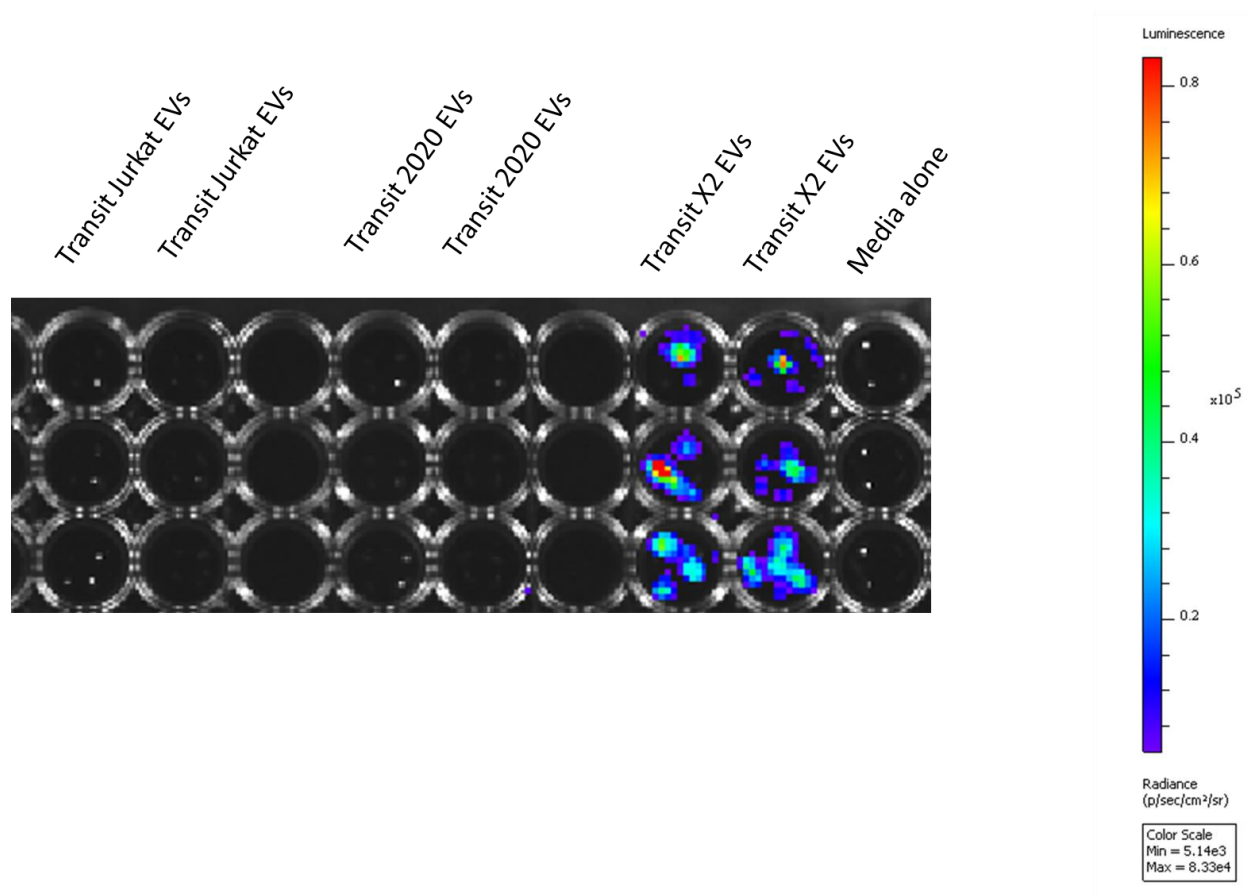
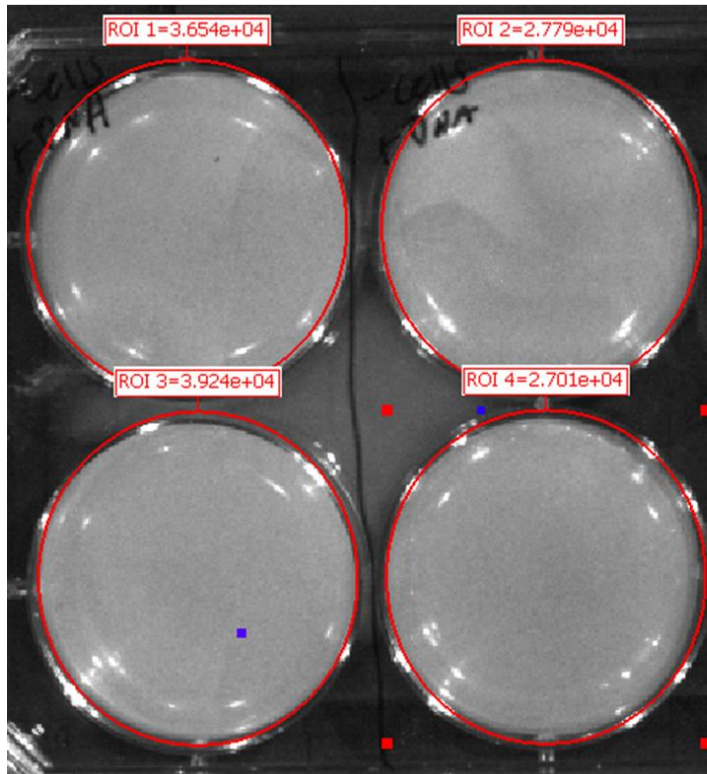


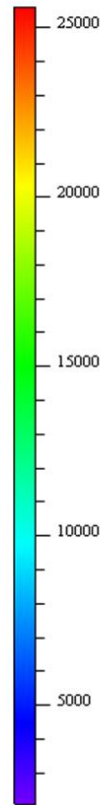
**Figure 4.6.** HEK293 cells seeded at 2E4 cells/well. 20 ul of EVs were added per well from isolated from cells in Figure 4.5. Photo taken 48 hours post EV addition.

To determine if this effect was due to remaining transfection reagent, two wells of THP-1 cells were transfected with Cag/Luc2-Tdt using Transit Jurkat, and two wells were given Transit Jurkat with Cag/Luc2-Tdt added to media. The THP-1 cells expressed no bioluminescent signal, but were washed with PBS twice and resuspended in EV-depleted media (Figure 4.7). The same was done to the media containing both the transfection reagent and DNA, with similar volume amounts being retained. EVs and THP-1 media containing transfection reagents were added to three wells of HEK293 cells, and 48h post-addition, only HEK293 cells treated with EVs expressed bioluminescence (Figure 4.8).

THP-1 cells transfected with Cag/Luc2-Tdt using Jurkat



Luminescence



Radiance  
(p/sec/cm<sup>2</sup>/sr)

Color Scale  
Min = 2.09e3  
Max = 2.56e4

**Figure 4.7.** THP-1 cells transfecting using TransIT Jurkat or Jurkat-DNA complexes suspended in media. No bioluminescence is seen 48h post-transfection.

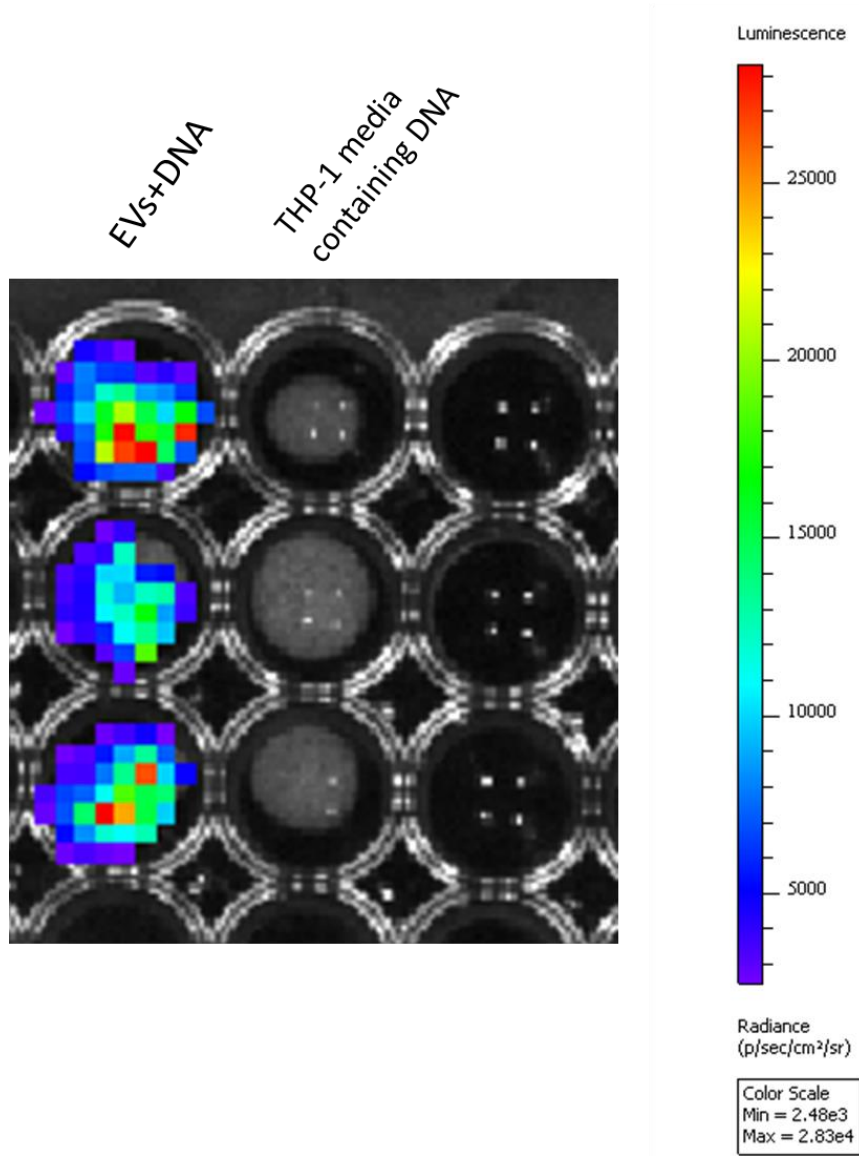


**Figure 4.8.** HEK293 cells seeded at 2E4 cells/well 24 hours before addition of EVs or THP-1 media. Photo taken 48 hours post addition. EVs and Media were isolated from two wells of cells.

It was suspected that EVs may be capable of functional delivery without the aid of transfection reagents, so Cag/Luc2-Tdt was added to two wells of THP-1 cells. Four wells were transfected using TransIT Jurkat with equal amounts of DNA ( $\mu\text{g}$ ). DNA expression was measured using bioluminescence and it was noted that one well of the THP-1 cells had about 4.6

times the amount of expression as the average of the other three wells. To determine if the expression of the EV-producer cells had an effect on delivery efficiency to recipient cells, EVs from each well were isolated separately and added to three wells of HEK293 cells. Recipient cell uptake was measured using bioluminescence. THP-1 EVs from cells with no transfection reagent did not have any functional delivery. THP-1 EVs from cells that had 4.6 times worse bioluminescence had better functional delivery to recipient cells than THP-1 EVs from cells that had more bioluminescence (Figure 4.9).

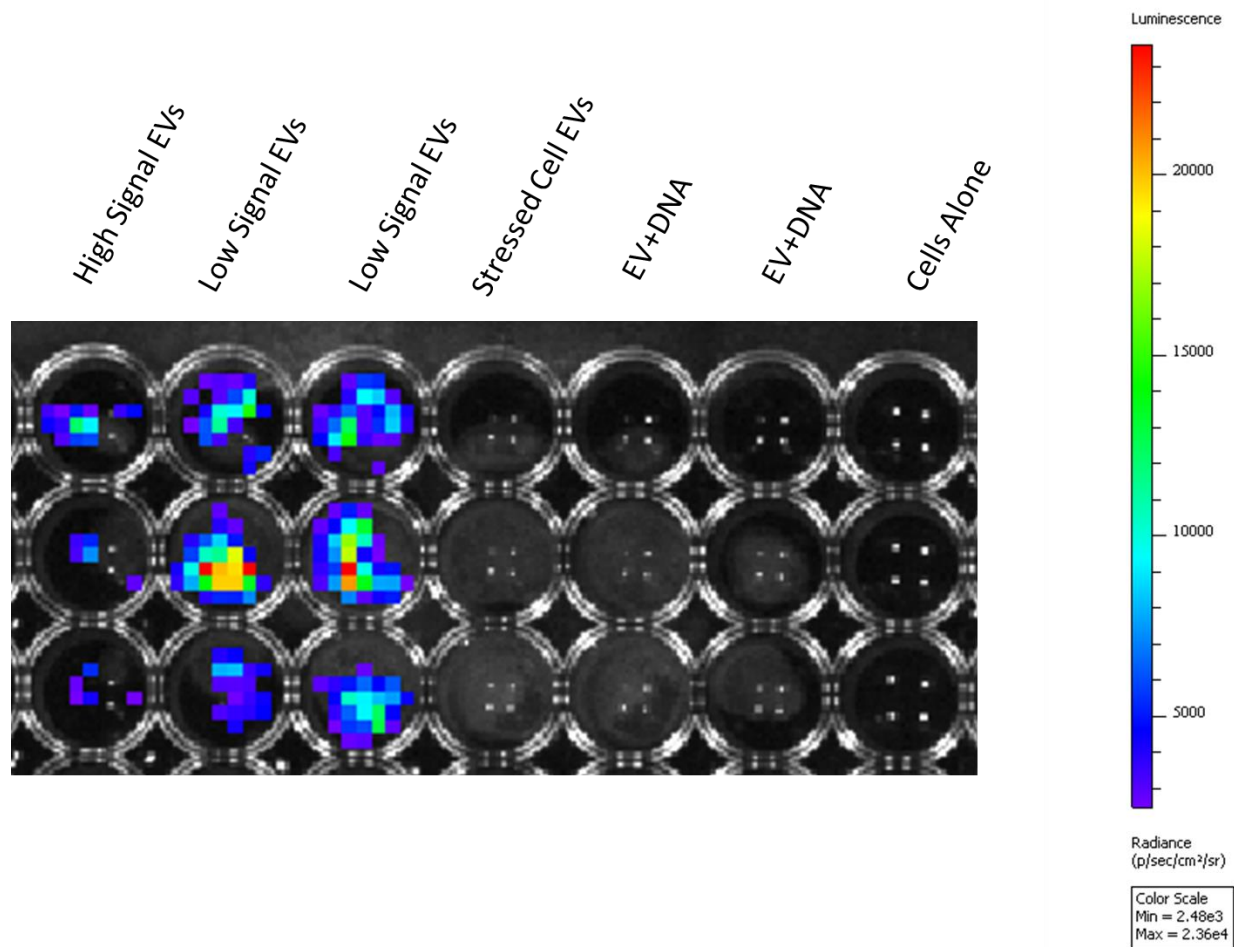


**Figure 4.9.** HEK293 cells seeded at 2E4 cells/well 24 hours before addition of EVs. Photo taken 48 hours post addition. EVs were isolated from one well of cells each.

Due to interest in macrophage delivery, THP-1 cells were differentiated to macrophages and transfected using TransIT Jurkat. Undifferentiated THP-1 cells were transfected using TransIT-Jurkat as a positive control. Only the undifferentiated THP-1 cells expressed bioluminescence (Figure 4.10).

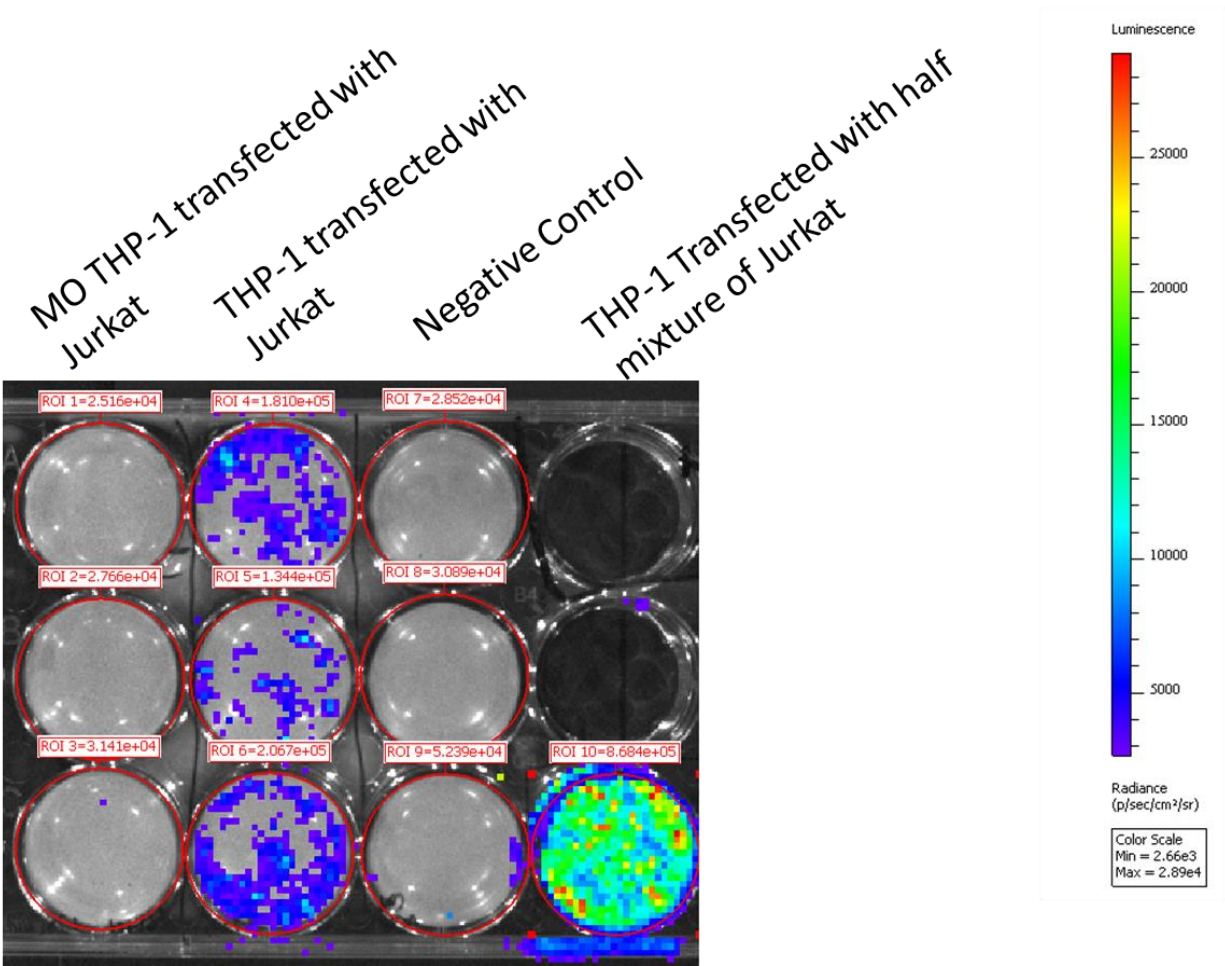


**Figure 4.10.** THP-1s were seeded at 3E5 cells/well day0. Day 1, 100 ng/ml PMA were added to three wells. Day 3, the 3 adherent wells and 3 nonadherent wells with transfected with Transit Jurkat. One nonadherent well was transfected with half the amount of DNA and Jurkat as the other nonadherent wells. Day 4, photo was taken.

## DICUSSION

Monocyte-like THP-1 cells were transfected with Cag/Luc2-Tdt using Transit-Jurkat. The cells were incubated with the DNA/Transit complexes for 24 hours, and checked for bioluminescence using the IVIS. The transfected cells were washed twice with PBS and added to EV-depleted media. The cells produced EVs for 24 hours, before the media was collected and underwent differential centrifugation. EVs isolated at 20,000g were added to HEK-293 cells or cardiac organoids. Half the cardiac organoids were seeded on Matrigel, a staple extracellular matrix mimetic. The uptake cells were exposed to the EVs for 48 hours before D-luciferin was added and the cells were checked for bioluminescence. The resulting bioluminescence was measured using the Living Image software. The recipient HEK293 cells expressed the Luc2 gene, which acted as a positive control. The cardiac organoids also expressed the Luc2 gene, and the cardiac organoids seeded on Matrigel had higher amounts of bioluminescence than the cardiac organoids in suspension in media. The reason for this is unknown, but it is suspected that the EVs may travel through the Matrigel to infiltrate the organoids, or the presence of the extracellular matrix adds in delivery. It has been shown that EVs can travel through extracellular matrices *in vivo* and *in vitro*, and artificial extracellular matrices are also used to deliver drugs with increased efficiency, so the presence of an artificial extracellular matrix may contribute towards increased efficiency of EV delivery as seen in the preliminary cardiac organoid studies.

Transfection efficiency studies indicated that transfection of THP-1 cells was best performed using a ratio of 1:3 DNA ( $\mu\text{g}$ ) to transfection reagent ( $\mu\text{l}$ ), on cells seeded immediately before transfection. These experiments were performed using a different number of cells, with a higher amount of cells being used when seeding immediately prior to transfection. This was done due to the possibility of cells splitting in the 24h prior to transfection and the

different amounts of cells possibly effecting light production. Bioluminescence is measured by the whole well, so the amount of signal per cell cannot be innately determined, and the cells were not counted immediately after imaging so this could be an effect of having more cells in the wells. However, dividing the average luminescence by the seeding amount of cells, assuming that there is no cell division, results in higher luminescence per cell. This could still be an effect of different cell densities, as cell density effects transfection efficiency.

Further transfection efficiency studies were performed using different transfection reagents; TransIT Jurkat, TransIT X2, and TransIT 2020. All reagents had very similar transfection efficiencies *in vitro*, so EVs were collected from each of the cells to determine if the delivery efficiency was effected by the type of transfection reagent. EVs from THP-1 cells transfected with TransIT X2 had the best functional transfer of nucleic acids or proteins. EVs from the THP-1 cells transfected with TransIT 2020 or TransIT Jurkat did not appear to have any functional transfer to HEK293 recipient cells, despite earlier success being seen with transfer using EVs from cells transfected with TransIT Jurkat. The lack of functional transfer seen here may be due to the delivery of EVs from THP-1 cells transfected with TransIT X2 being incredibly efficient. A draw back to bioluminescence imaging is that higher signals can sometimes mask lower signals due to automatic imaging being used, which searches for the point where the most signal can be seen. It's possible that imaging for longer would have revealed signal in the other wells.

In order to determine if the transfer effect is due solely to remaining transfection reagent and DNA in the media, THP-1 cells were transfected using TransIT Jurkat and Cag/Luc2-Tdt. Additional wells with only cell medium had TransIT Jurkat and DNA complexes added, and later underwent the same process as extracellular vesicle isolation side by side with the THP-1

EV isolation, at the same volumes. The remaining media was added to HEK293 recipient cells, same as the THP-1 EVs, and recipient cell's BLI expression was measured. There was no expression of BLI when media containing TransIT Jurkat and DNA complexes underwent differential high-speed centrifugation and was given to recipient cells, making it unlikely that the expression of bioluminescence is due to leftover transfection reagent and DNA complexes. Interestingly, treatment with EVs from the THP-1 cells that expressed no detectable radiance resulted in HEK293 expressing bioluminescence. This could be due to the amount of EVs being added having enough protein or nucleic acids to result in expression in less cells, or HEK293 cells maybe being better at expressing luminescence compared to THP-1 monocyte cells.

Because EVs have been shown to be able to transfer DNA without the use of a lipid or polymer based transfection reagent, a test was done where DNA was added directly to monocyte cells, which may act as scavengers and get rid of DNA via EVs. DNA was added to two wells of a six well dish, while the other four were transfected using TransIT Jurkat. Measuring the radiance of the THP-1 cells after transfection or DNA treatment revealed that one of the transfected wells had higher radiance than the average of the other three wells. To determine if radiance of the EV donating cells affected the expression of the recipient cells, the EVs of those wells were isolated separately from each other and added to different rows of HEK293 cells, with EVs from the DNA-treated cells added to other rows of HEK293 cells. Treatment with EVs from cells with DNA and no transfection reagent resulted in no expression in recipient cells, indicating that adding DNA to scavenger cells is not enough for detectable signal in recipient cells, which is not unexpected. HEK293 cells treated with EVs from wells with lower radiance had higher bioluminescence signal compared to HEK293 cells treated with EVs from the well

with higher radiance. Combined with the previous results, this suggests that there may be an inverse relationships between the expression of the EV donor cells and the EV recipient cells.

Because there is more interest in macrophage EVs as a delivery tool compared to monocyte EVs, THP-1 cells were also differentiated to macrophages and transfected using TransIT Jurkat along side undifferentiated THP-1 cells. Only the undifferentiated THP-1 cells expressed bioluminescence, but from our previous results seen in this thesis, this may indicate that the macrophage cells are better at DNA delivery. Unfortunately that has not yet been explored.

## **CONCLUSIONS AND FURTHER DIRECTIONS**

mmEVs are capable of delivering functional cargo to recipient cardiac organoids. Interestingly, there may be an inverse relationship between expression of the EV donor cells and expression of the EV recipient cells. Further work in this area may start by attempting to differentiate THP-1 cells to the M2 phenotype, before transfecting them and harvesting EVs to treat cardiac organoids to see if there is functional cargo transfer. If there were cargo transfer, M2 macrophages would be used as the EV donor cells in future experiments, if not, THP-1 monocyte-like cells would continue to be used. Next, cardiac organoids would be exposed to low oxygen conditions and stress to see if there was an increase in recipient cell expression. An increase in recipient cell expression would indicate a possible increase in uptake of mmEVs during inflammation by the cardiac organoids.

## **MATERIALS AND METHODS**

### **Cell Culture**

Human monocyte-like THP-1 cells (ATCC) were kept at 37°C in 5% CO<sub>2</sub>. They were maintained in suspension in RPMI1640 media supplemented with 10% fetal bovine serum

(FBS). Passaging of these suspension cells was done by spinning the cells at 130g for 7 minutes, before resuspension in fresh media. Cells were then automatically counted using Tryptophan-Blue for staining Live/Dead cells, and the amount of media was adjusted to maintain a concentration of  $5 \times 10^5$ - $1 \times 10^6$  cells/ml. Cardiac organoids were gifted by the Aguirre lab and maintained in RPMI1640 media supplemented with 10% FBS, and maintained at 37°C with 5% CO<sub>2</sub>. Human embryonic kidney, HEK293 (ATCC), cells were kept in the same conditions. HEK293 cells were passaged using 5% Trypsin-EDTA, and counted using Tryptophan-Blue for staining Live/Dead cells. The live cell count was used for seeding.

### **Macrophage Differentiation**

THP-1 cells were treated with 100 ng/ml PMA for 48 hours to differentiate them to macrophages. Macrophage differentiation was measured by successful adherence of the previously suspension cells.

### **Transfections**

THP-1 cells were transfected using TransIT Jurkat and Cag/Luc2-Tdt, in a ratio of 1:3 DNA ( $\mu\text{g}$ ) to transfection reagent ( $\mu\text{l}$ ) following manufacturer's instructions for transfecting suspension cells. 8E5 cells/well were seeded in a six well dish immediately prior to transfection. A master mix of TransIT Jurkat, DNA, and OptiMEM was created and incubated for 30 minutes at RT before being added drop wise to each well. The dish was gently swirled to mix the media, DNA-TransIT complexes, and cells before being incubated for 24h.

THP-1 cells were transfected with several different reagents, including: TransIT Jurkat, TransIT 2020, TransIT X2, using a ratio of 1:3 DNA ( $\mu\text{g}$ ) to transfection reagent ( $\mu\text{l}$ ), following manufacturer's instructions THP-1 cells were seeded immediately before in a six well dish with 6E5 cells/well. Two wells were transfected with each type of reagent.

In order to optimize THP-1 cell transfection, 4E5 THP-1 cells/well were seeded in 10 wells of a 12 well dish. Cag/Luc2-Tdt DNA was mixed with TransIT-Jurkat transfection reagent in OptiMEM in ratios of 1:2, 1:3, 1:4, and 1:5 DNA ( $\mu\text{g}$ ) to transfection reagent ( $\mu\text{l}$ ). Two wells each received the different mixes of each ratio of DNA to transfection reagent 24 hours after seeding. 4.5E5 THP-1 cells/well were seeded in a different 12 well dish, with two wells each receiving DNA mixed with TransIT-Jurkat transfection reagent in OptiMEM in ratios of 1:2, 1:3, 1:4, and 1:5 DNA ( $\mu\text{g}$ ) to transfection reagent ( $\mu\text{l}$ ) immediately after seeding. Transfection efficiency was tested using bioluminescence imaging 24 hours later.

THP-1 cells were seeded in nine wells of a 12 well. Three of those wells were differentiated to macrophages over the course of 48 hours, while the remaining six were allowed to expand. All cells were transfected using TransIT Jurkat with Cag/Luc2-Tdt in a ratio of 1:3 DNA ( $\mu\text{g}$ ) to transfection reagent ( $\mu\text{l}$ ). Expression of the DNA was measured using bioluminescence 24h later.

### **Extracellular Vesicle Isolation**

THP-1 cells were washed twice in PBS by spinning at 300g for 5min for each wash, before being resuspended in RPMI1640 supplemented with 10% EV-depleted FBS. The cells were incubated in the EV-depleted media for 24 hours, before the mix was removed for differential high-speed centrifugation. Cells were pelleted at 600g for 10min, and the supernatant was removed. The apoptotic bodies were pelleted from that supernatant at 2,000g for 20min, and the supernatant removed again for EV isolation. EVs were pelleted at 20,000g for 1h, and resuspended in remaining media after the supernatant was removed.

## Extracellular Vesicle Treatments

For the initial testing of EV delivery, HEK293 cells were used as a positive control for EV uptake and subsequent reporter gene expression. HEK293 cells were seeded in four wells of a 96 well dish at 2E4 cells/well. Cardiac organoids in a 96 well dish were gifted by the Aigurre lab, four seeded on Matrigel in a 96 well plate, and three organoids in suspension in media. EVs from six wells of TransIT Jurkat-transfected THP-1 cells were isolated and resuspended in 6 equal amounts of EVs in media. Two of these EVs in media were added to 2 wells of HEK293 cells, two mixes added to two wells of cardiac organoids on Matrigel, and two mixes added to two wells of cardiac organoids in suspension. All cells were incubated for 48 hours before testing for EV transfer using bioluminescence imaging.

For testing different reagents, HEK 293 cells were seeded at 2E4 cells/well in a 96 well dish 24 hours before transfer. EVs were isolated from THP-1 cells transfected using TransIT Jurkat, TransIT X2, or TransIT 2020. 20 µl of EVs were added per well of HEK 293 cells, for a total of six wells per transfection reagent type. The equivalent of 1/3 of EVs from one well of a six well dish were therefore added per one well of a 96 well dish. The EVs were incubated with the recipient cells for 48 hours before delivery was confirmed using bioluminescence imaging. EVs were collected from two wells of THP-1 cells transfected with Cag/Luc2-Tdt using TransIT Jurkat. Equal volume amounts of RPMI1640 media had TransIT Jurkat and Cag/Luc2-Tdt complexes added and underwent differential high-speed centrifugation to determine if the detected EV delivery was due to leftover transfection reagent. Same volume amounts of THP-1 EVs or media with transfection complexes were added to three wells each of HEK293 cells, seeded at 2E4 cells/well the day prior. Successful transfer was determined by bioluminescence imaging 48h later.

EVs were collected from individual wells of THP-1 cells transfected using TransIT Jurkat that had different levels of bioluminescence output. Equal weight amounts of Cag/Luc2-Tdt DNA was added to two wells of THP-1 cells, and EVs were isolated from these cells. Equal volume amounts of EVs from each well were added to three wells of HEK293 cells seeded at  $2 \times 10^4$  cells/well 24 hours prior. EV delivery was measured using bioluminescence 48 hours later.

### **Bioluminescence Imaging**

D-luciferin (10mg/ml) was added to the cells and mixed with them for 5 minutes before imaging. BLI was measured using the IVIS system from Perkin Elmer using the autoexposure settings, altered to a maximum time of 600s, with binning set to medium, f/stop equal to 1, and an open emission filter.

### **Statistical Significance**

Statistical significance between groups was determined using a standard T-test using Graph Pad. Luminescence was determined by the Living Image software made by Perkin Elmer, measuring total radiance (p/sec/cm<sup>2</sup>/sr) of each well.

## REFERENCES

1. Awada, H. K., Hwang, M. P. & Wang, Y. Towards comprehensive cardiac repair and regeneration after myocardial infarction: Aspects to consider and proteins to deliver. *Biomaterials* Preprint at <https://doi.org/10.1016/j.biomaterials.2015.12.025> (2016).
2. Singelyn, J. M. *et al.* Naturally derived myocardial matrix as an injectable scaffold for cardiac tissue engineering. *Biomaterials* (2009) doi:10.1016/j.biomaterials.2009.06.045.
3. Nahrendorf, M., Pittet, M. J. & Swirski, F. K. Monocytes: Protagonists of infarct inflammation and repair after myocardial infarction. *Circulation* Preprint at <https://doi.org/10.1161/CIRCULATIONAHA.109.916346> (2010).
4. Ramamoorth, M. & Narvekar, A. Non viral vectors in gene therapy - An overview. *Journal of Clinical and Diagnostic Research* Preprint at <https://doi.org/10.7860/JCDR/2015/10443.5394> (2015).
5. Glover, D. J., Lipps, H. J. & Jans, D. A. Towards safe, non-viral therapeutic gene expression in humans. *Nature Reviews Genetics* Preprint at <https://doi.org/10.1038/nrg1577> (2005).
6. Su, C.-H., Wu, Y.-J., Wang, H.-H. & Yeh, H.-I. Nonviral gene therapy targeting cardiovascular system. *American Journal of Physiology-Heart and Circulatory Physiology* (2012) doi:10.1152/ajpheart.00126.2012.
7. Lee, Y., el Andaloussi, S. & Wood, M. J. A. Exosomes and microvesicles: Extracellular vesicles for genetic information transfer and gene therapy. *Hum Mol Genet* (2012) doi:10.1093/hmg/dds317.
8. Alibhai, F. J., Tobin, S. W., Yeganeh, A., Weisel, R. D. & Li, R.-K. Emerging roles of extracellular vesicles in cardiac repair and rejuvenation. *American Journal of Physiology-Heart and Circulatory Physiology* (2018) doi:10.1152/ajpheart.00100.2018.
9. Jansen, F., Li, Q., Pfeifer, A. & Werner, N. Endothelial- and Immune Cell-Derived Extracellular Vesicles in the Regulation of Cardiovascular Health and Disease. *JACC: Basic to Translational Science* Preprint at <https://doi.org/10.1016/j.jacbts.2017.08.004> (2017).
10. Molinaro, R. *et al.* Biomimetic proteolipid vesicles for targeting inflamed tissues. *Nat Mater* (2016) doi:10.1038/NMAT4644.
11. Bunggulawa, E. J. *et al.* Recent advancements in the use of exosomes as drug delivery systems. *Journal of Nanobiotechnology* vol. 16 Preprint at <https://doi.org/10.1186/s12951-018-0403-9> (2018).

12. Yuan, D. *et al.* Macrophage exosomes as natural nanocarriers for protein delivery to inflamed brain. *Biomaterials* **142**, 1–12 (2017).
13. Kim, M. S. *et al.* Engineering macrophage-derived exosomes for targeted paclitaxel delivery to pulmonary metastases: *in vitro* and *in vivo* evaluations. *Nanomedicine* **14**, 195–204 (2018).
14. Haney, M. J. *et al.* Macrophage-Derived Extracellular Vesicles as Drug Delivery Systems for Triple Negative Breast Cancer (TNBC) Therapy. *Journal of Neuroimmune Pharmacology* **15**, 487–500 (2020).
15. Viola, M., de Jager, S. C. A. & Sluijter, J. P. G. Molecular Sciences Targeting Inflammation after Myocardial Infarction: A Therapeutic Opportunity for Extracellular Vesicles? (2021) doi:10.3390/ijms22157831.
16. Yang, L. *et al.* Stem cell-derived extracellular vesicles for myocardial infarction: a meta-analysis of controlled animal studies. *Aging* **11**, 1129–1150 (2019).
17. Wang, Y. *et al.* Macrophage-derived extracellular vesicles: diverse mediators of pathology and therapeutics in multiple diseases. *Cell Death & Disease* **2020 11:10** **11**, 1–18 (2020).
18. Wang, C. *et al.* Macrophage-Derived mir-155-Containing Exosomes Suppress Fibroblast Proliferation and Promote Fibroblast Inflammation during Cardiac Injury. *Molecular Therapy* **25**, 192–204 (2017).
19. Zhang, Z. *et al.* Exosomes as a messenger to regulate the crosstalk between macrophages and cardiomyocytes under hypoxia conditions. *J Cell Mol Med* **26**, 1486–1500 (2022).

CHAPTER FIVE:  
CONCLUSIONS AND FUTURE DIRECTIONS

When iron nanoparticles with the help of heparin and protamine sulfate<sup>1</sup> were taken up by tumor cells, those tumor cells could produce EVs associated with iron. It was unable to determine if iron was contained within the EVs, though from TEM images it seems more likely that they associate with the EV membranes, and are not contained within. Loading nanoparticles into EVs by loading the EV donor cells and collecting EVs from those cells has been done before<sup>2,3</sup>, and those nanoparticles are believed to be contained within the EVs<sup>3</sup>. It is possible that the use of heparin and protamine sulfate to improve uptake of the SPIOs alters the route of internalization of the nanoparticle, changing how the SPIOs are excreted by the cells. It is possible that EVs from the producer cells are merely associated with SPIOs leftover from the cell-labeling process, but it is unlikely due to the cells being washed four times before the addition of the EV-depleted media, and the differences seen between free iron and EV-associated iron during cancer. Iron associated with EVs isolated from tumor cells was preferentially retained in primary tumors in comparison to free iron, as determined by MPI. Further sectioning of the tumor showed that iron was present in tumor cells and associated with macrophages, determined by immunochemistry staining for tumor and macrophage markers, compared to the free iron which could not be identified at all and is typically taken up by macrophages<sup>4</sup>.

Another point that proves that there was association between the SPIOs and the EVs was that it had an effect on the distribution of the SPIOs. If the SPIOs were not associated with EVs, we would see similar distribution and accumulation when only SPIOs were injected. We see that in the case of healthy mice, but not in mice suffering from tumor burden. There was a significant difference in accumulation between the SPIOs and the FeEVs seen in primary breast tumors, and SPIOs alone did not accumulate in the brain when it was burdened with metastasis, unlike the FeEVs. This indicates a difference between the free iron and the iron associated with EVs.

It is interesting as well that the iron loading had an effect on protein expression of the EVs. It is unknown if this is due to any property of the iron oxide nanoparticle used or the use of heparin and protamine sulfate to help load the nanoparticles into the cells. It is interesting that the loading of the SPIOs appears to result in EVs that have higher amounts of proteins linked to EV uptake. Future studies may want to compare the delivery of a drug when it is loaded into EVs with the assistance of heparin and protamine sulfate vs when it is loaded into EVs using other methods to determine if the loading method results in EVs more prone to being taken up by cells. If so, this could be an interesting way to improve EV delivery in other diseases.

It should be noted that this enhanced retention and accumulation was only tested using cancer cell-derived EVs. To see if this retention and accumulation is due to the use of specifically cancer cell-derived EVs, and not all EVs, another type of parent cell such as a red blood cell or a healthy breast tissue cell line should be loaded with SPIOs and FeEVs from those lines collected. They should then have their distribution and retention compared to the FeEVs derived from breast cancer cells. In addition, to determine if this effect is due to any kind of “self-homing”<sup>5-7</sup>, SPIOs should be loaded into cancer cells from a different type of cancer, such as melanoma, and seeing if these cancer cell-derived FeEVs could also be retained in breast tumors and accumulate in brain metastases. This would allow it to be determined if the effect is due to the use of the same type of cancer EV, or just a general targeting of all cancer cell EVs to areas of cancer<sup>5-7</sup>.

In a future study, FeEVs from breast cancer cells should be loaded with a therapeutic agent to observe a change in brain metastasis size. This should be compared to iron nanoparticles conjugated to the therapeutic agent if SPIOs are still being used, or to the drug loaded into a liposome. The drug-loaded liposome would allow for a comparison of a lipid-associated drug,

which enhances delivery, to the lipid-membrane derived EVs. When choosing the therapeutic agent, off-target effects should be carefully considered. As most of the EVs end up in the liver, we do not want to cause damage to the organ. One potential therapeutic is a pro-drug therapy<sup>8</sup>, which would require both the drug and the enzyme to be present in order for cell death to occur and has been delivered using EVs<sup>9</sup>. Another possible idea would be using the HYPER therapy to target specific areas of the body where the iron oxide nanoparticles are present, such as a tumor, avoiding the liver completely. This therapy works by causing the SPIOs to switch the direction of magnetization very quickly, generating kinetic energy that is transformed into thermal energy, heating the cells around the SPIOs, causing cell death<sup>10</sup>.

mmEVs were also capable of delivery to cardiac organoids as well as human embryonic kidney cells as a positive control. The data presented in this thesis was very preliminary, using cardiac organoids and monocyte-derived EVs. Future work would benefit from starting by studying M2-derived EVs, as M1-derived EVs have been shown to promote inflammation<sup>11</sup>. Delivery of M2-derived EVs to cardiac organoids should be compared to monocyte-derived EVs by comparing light output. Next, cardiac organoids should be placed under MI-like conditions, which can be done by a combination of low oxygen and noradrenaline<sup>12</sup>, causing inflammation. Delivery of the superior mmEV would then be compared to cardiac organoids under MI-like conditions and healthy cardiac organoids in order to determine if there is an increase in accumulation in damaged heart tissue of mmEVs. The cardiac organoid should then be sectioned and stained for the different cells in the heart to determine what type of cell in the heart the mmEVs deliver cargo to. This would then inform the type of therapeutic that could be delivered using mmEVs.

## REFERENCES

1. Gutova, M. *et al.* Magnetic Resonance Imaging Tracking of Ferumoxytol-Labeled Human Neural Stem Cells: Studies Leading to Clinical Use. *Stem Cells Transl. Med.* **2**, 766 (2013).
2. Herrmann, I. K., Wood, M. J. A. & Fuhrmann, G. Extracellular vesicles as a next-generation drug delivery platform. *Nat. Nanotechnol.* **2021** *167* **16**, 748–759 (2021).
3. Marzola, P. *et al.* Magnetic resonance imaging of ultrasmall superparamagnetic iron oxide-labeled exosomes from stem cells: a new method to obtain labeled exosomes. *Int. J. Nanomedicine* (2016) doi:10.2147/ijn.s104152.
4. Makela, A. V. *et al.* Magnetic Particle Imaging of Macrophages Associated with Cancer: Filling the Voids Left by Iron-Based Magnetic Resonance Imaging. *Mol. Imaging Biol.* **22**, (2020).
5. Xie, X. *et al.* Tumor-derived exosomes can specifically prevent cancer metastatic organotropism. *J. Control. Release* **331**, 404–415 (2021).
6. Qiao, L. *et al.* Tumor cell-derived exosomes home to their cells of origin and can be used as Trojan horses to deliver cancer drugs. *Theranostics* **10**, 3474 (2020).
7. Nguyen, V. Du, Kim, H. Y., Choi, H., Park, J.-O. & Choi, E. Tumor-derived extracellular vesicles for the active targeting and effective treatment of colorectal tumors in vivo. *Drug Deliv.* **2022**, 2621–2631 (2022).
8. Sekar, T. V., Foygel, K., Willmann, J. K. & Paulmurugan, R. Dual-therapeutic reporter genes fusion for enhanced cancer gene therapy and imaging. *Gene Ther.* **20**, (2013).
9. Kanada, M. *et al.* Microvesicle-mediated delivery of minicircle DNA results in effective gene-directed enzyme prodrug cancer therapy. *Mol. Cancer Ther.* **18**, 2331–2342 (2019).
10. Tay, Z. W. *et al.* Magnetic Particle Imaging-Guided Heating in Vivo Using Gradient Fields for Arbitrary Localization of Magnetic Hyperthermia Therapy. *ACS Nano* **12**, (2018).
11. Liu, S. *et al.* M1-like macrophage-derived exosomes suppress angiogenesis and exacerbate cardiac dysfunction in a myocardial infarction microenvironment. *Basic Res. Cardiol.* **115**, (2020).
12. Richards, D. J. *et al.* Human cardiac organoids for the modelling of myocardial infarction and drug cardiotoxicity. *Nat. Biomed. Eng.* **4**, 446–462 (2020).